BEILSTEIN JOURNAL OF NANOTECHNOLOGY

Laser material processing in liquids for nanoparticle synthesis

Edited by Gladys Mínguez-Vega, Benjamin Mockenhaupt and Vincenzo Amendola

Generated on 23 November 2026, 23:21

Imprint

Beilstein Journal of Nanotechnology
www.bjnano.org
ISSN 2190-4286
Email: journals-support@beilstein-institut.de

The *Beilstein Journal of Nanotechnology* is published by the Beilstein-Institut zur Förderung der Chemischen Wissenschaften.

Beilstein-Institut zur Förderung der Chemischen Wissenschaften
Trakehner Straße 7–9
60487 Frankfurt am Main
Germany
www.beilstein-institut.de

The copyright to this document as a whole, which is published in the *Beilstein Journal of Nanotechnology*, is held by the Beilstein-Institut zur Förderung der Chemischen Wissenschaften. The copyright to the individual articles in this document is held by the respective authors, subject to a Creative Commons Attribution license.

BEILSTEIN JOURNAL OF NANOTECHNOLOGY

Combining laser ablation and sol–gel techniques for the synthesis of nanostructured organic–inorganic matrices

Emmanuel Haro-Poniatowski*[1,2], Cesar Augusto Guarín[1], Luis Guillermo Mendoza-Luna[1], Luis Escobar-Alarcón[3], José Luis Hernández-Pozos[1], L. Irais Vera-Robles[4], Patricia Castillo[5], Fátima Cabello[2], Johann Toudert[2], Fernando Chacón-Sánchez[2], Marina García-Pardo[2], Rosalia Serna[2], José Gonzalo[2] and Javier Solís[2]

Full Research Paper

Open Access

Address:
[1]Departamento de Física, Universidad Autónoma Metropolitana Iztapalapa, Apdo. Postal 55-534, México City, México, [2]Laser Processing Group, Instituto de Óptica, IO, CSIC, Serrano, 121 28006 Madrid, Spain, [3]Departamento de Física, Instituto Nacional de Investigaciones Nucleares, Carretera México-Toluca S/N, la Marquesa, Ocoyoacac, Estado de México. C.P.52750, México, [4]Departamento de Química, Universidad Autónoma Metropolitana Iztapalapa, Apdo. Postal 55-534, México City, México and [5]Laboratorio Microscopía Electrónica, Universidad Autónoma Metropolitana Iztapalapa, Apdo. Postal 55-534, México City, México

Email:
Emmanuel Haro-Poniatowski* - haro@xanum.uam.mx

* Corresponding author

Keywords:
laser ablation; nanocomposite glasses; sol–gel

Beilstein J. Nanotechnol. **2026,** *17,* 1478–1487.
https://doi.org/10.3762/bjnano.17.101

Received: 18 June 2026
Accepted: 06 October 2026
Published: 23 October 2026

This article is part of the thematic issue "Laser material processing in liquids for nanoparticle synthesis".

Guest Editor: G. Mínguez-Vega



© 2026 Haro-Poniatowski et al.; licensee Beilstein-Institut.
License and terms: see end of document.

Abstract

In this work we report a new and simple method that combines pulsed laser ablation in liquids (PLAL) and sol–gel techniques to obtain nanocomposite glasses and gelatins. Using this combination, we obtained two kinds of materials, bulk glasses on the one hand and gelatin films on the other hand. In the case of glasses, gold nanoparticles (Au-NPs) are generated by PLAL using an Au target submerged in a transparent liquid solution made previously with tetraethyl orthosilicate (TEOS) adding diluted hydrochloric acid as catalyzer. For gelatins, the same procedure is employed; however, in this case only commercial gelatin and tap water are used. We have found that a successful synthesis strongly depends on time and temperature since the viscosity of the gels increases with time. For the drying process the gels are sealed and stored at room temperature for several days. We identify the principal parameters that have to be considered in order to achieve a successful synthesis. The samples are characterized by UV–vis spectroscopy, HRTEM, ellipsometry and AFM microscopy. UV–vis spectra show a surface plasmon resonance band with its maximum at 540 nm indicating the presence of Au-NPs. HRTEM reveals crystalline Au-NPs with an average size of 20 nm. AFM measurements indicate that the glasses have a very smooth surface. In the case of gelatins, self-sustained, transparent, and pink flexible

films are obtained. Despite having determined the principal parameters involved in the obtention of these materials, we emphasize that a lot of work remains to be done in order to optimize this novel method of synthesis.

Introduction

Nanocomposite glasses have been around us since ancient times. Nowadays we know that the change in color upon transmission and reflection of light of the exceptional fourth-century Lycurgus cup, fabricated by the Romans, is due to the fact that it is made of a glass with Au and Ag nanoparticles (NPs) embedded in it [1], forming a nanocomposite. A nanocomposite is a kind of material in which one phase with nanoscale dimensions is embedded in a ceramic, glass, or polymer matrix. Great effort has been made recently to incorporate NPs into a wide variety of matrices that can be liquid or solids, crystalline or amorphous. This incorporation results in changes in the physical and chemical properties of the matrices, which are in some cases better than the properties of their individual components. Some examples are the improvement of the tribological properties of metals, oils, and polymers [2-4]. Nanoparticles of CdTe of different sizes have been dispersed in liquid, changing their color progressively from yellow to blue according to their corresponding size [5]. Other applications include quantum computing, with significant efforts pursued in fabricating nanodots embedded in different matrices and structures [6]. Additionally, multiple applications in the field of plasmonics require the synthesis of nanostructures in various substrates or matrices [7]. Very recently, the idea of embedding nanoparticles into a glassy matrix has been extended to include gelatin as a matrix to fabricate eco-friendly optical components such as flexible filters [8].

For a few years, we have been involved in the synthesis and development of nanostructured glasses. Our interest has been focused on nanoparticles of metals with low melting point immersed in solid matrices with high melting point. These systems are important because of their potential applications in optothermal devices such as thermo-optical switches responding to changes in temperature [9,10]. However, only a few examples can be found in the literature regarding these nanocomposites. To our knowledge, only Se, Bi, and Pb nanocrystals, and more recently CuCl and CuBr have been synthesized successfully in bulk amorphous matrices [11,12].

Finally, it is important to mention that the process of making such glasses is difficult and time- and energy-consuming due to the high temperatures needed in their fabrication. Consequently, synthesizing such systems “on demand”, for example, the fabrication of a glass with embedded elemental metallic NPs, is not an easy and straightforward process. Several routes have been, and are currently, under investigation. Pulsed laser deposition (PLD) has proved to be a suitable method to fabricate such nanocomposites [13-15].

An alternative possibility for the fabrication of the desired colloidal systems is the pulsed laser ablation in liquids (PLAL) technique [16]. Nanostructures of different sizes and morphologies including metals, alloys, and oxides have been produced by this technique [17,18]. An important advantage of PLAL is its versatility, enabling its combination with other fabrication processes in an easy way. In such direction, we have synthesized carbon nanosheets using PLAL under an ultrasound field [19]. However, the reports of PLAL-made nanocomposites are scarce. As mentioned before, nanoparticles have been dispersed by PLAL in polymers and in resins. For example, nail enamels of different colors have been produced by dispersing Au, Ag, and Pt nanoparticles by PLAL in a nail varnish [20].

For the synthesis of nanocomposite glasses, an alternative and convenient solution is the sol–gel technique. This method has the advantage of being fast and simple; furthermore, the materials are fabricated at room temperature, and eventual thermal treatments are of the order of only a few hundred degrees Celsius. The main drawback is that it is not easy to obtain large monoliths. Furthermore, the drying process is long and difficult to optimize. Using this technique, nanostructured glasses have been obtained by mixing organo-metallic products and colloids with nanoparticles. However, the variety of organo-metallic products has some limitations such as availability and price. Furthermore, an important advantage of PLAL is its independence from chemical precursors, avoiding the use of toxic substances or other by-products that can be present in the obtained material. To the best of our knowledge, there are few works that combine PLAL with a chemical route for synthesis of nanocomposites. The coating of gold nanoparticles with silica shells via PLAL in a single-step by ablating a gold target directly inside a mixture of tetraethyl orthosilicate (TEOS) and a catalyst has been reported [21]. Gd_2O_3@SiO_2 nanoparticles, formed by a gadolinium oxide core and a silica shell, have been synthesized in a single step via PLAL of a submerged Gd_2O_3 target in TEOS. As Gd_2O_3 nanoparticles are formed, they are immediately coated with SiO_2, directly yielding a core–shell structure for the use as MRI contrast agents [22].

In the present work, we propose to use the combination of the sol–gel and laser ablation techniques to synthesize nanostructured glasses and gelatins [23]. The main requirement is to use a

solution that is transparent at the wavelength used for ablation. The variety of glassy materials and gelatins that can be fabricated is very broad, while possible limitations could be the availability of the solid target, or the nature of the solvent. In the first approach of this combination of techniques, we have obtained Au nanoparticles embedded in a silica matrix and in a commercial gelatin. The presence of the NPs has been confirmed by UV–vis spectroscopy and TEM microscopy. The synthesis of the nanocomposite glasses reported in the present work is fast and simple compared to other methods of fabrication and has several potential applications since the materials can be prepared in bulk and thin film forms. However, a lot of work is still needed to optimize several parameters that determine the obtention of the final product. In the case of gelatins, we present some preliminary results in Supporting Information File 1, Section S1. The fabrication process is simpler than that of sol–gel glasses, and the results are very similar to those reported in [8] except for the method of the nanoparticles incorporation in the gelatin, which is PLAL in our case.

Results and Discussion

First, the optimum experimental conditions must be determined. The main parameters involved in the synthesis of nanocomposite glasses combining PLAL and sol–gel techniques are the following: (a) transparency of the sol, (b) temperature, (c) viscosity (viscosity decreases with temperature), (d) ablation time (viscosity increases with time), (e) amount of liquid above the target, (f) energy density, (g) laser wavelength, and (h) post-preparation thermal treatments. Furthermore, the optimization of these parameters in some cases can involve the change of the original formula used for the preparation of the sol as discussed later. Most of these parameters have been identified in previous works [20,23]. As said before, a very sensible one is viscosity, since it is directly related to the proper dispersion of nanoparticles; this aspect needs to be thoroughly investigated in future experiments.

Sol–gel glasses

The ablation process starts typically within one hour after the preparation of the sol when its temperature is around 40 °C; this gives enough time to perform the ablation (10 min) and to obtain a high dispersion of the Au nanoparticles. The effect of increasing viscosity with time is easily observable by the eye; however, a suitable experimental procedure is needed for obtaining quantitative information. This investigation is out of scope of the present work. The amount of liquid is also crucial for the laser ablation process, a thin layer of liquid results in significant splashing. In the present experiments, we have used a liquid layer around 1 cm above the surface of the target. As soon as the ablation process takes place, the production of gold nanoparticles can be detected visually. In Figure 1, for coloration comparison, the obtained gel is presented (Figure 1a) together with a colloid of gold nanoparticles (Au-NPs) obtained by PLAL in distilled water (Figure 1b) under the same experimental conditions.

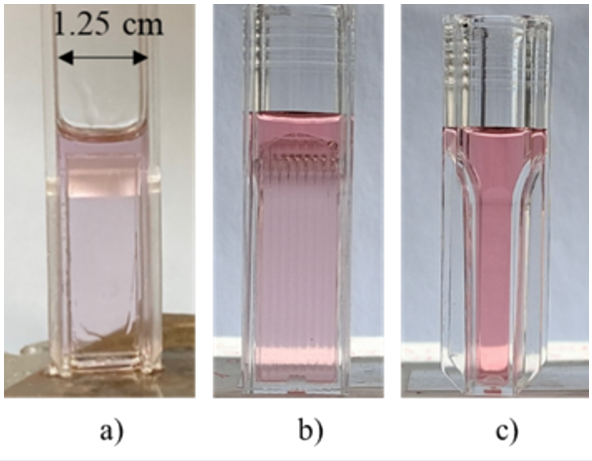

Figure 1: (a) As-prepared Au-NPs in the sol–gel solution, (b) Au-NPs in distilled water, and (c) lateral view of (b).

The gels were immediately characterized by UV–vis spectroscopy. The same setup configuration and measurement method were used for all the UV–vis spectroscopy measurements reported in this paper. Before ablation, a transparent reference sample was withdrawn from the sol. The UV–vis extinction spectra of the reference gel, the as-prepared gel with Au-NPs, and the gel with Au-NPs after ten days of drying are presented in Figure 2. The blue spectrum corresponds to the reference sample; as expected, no extinction features are observed in the visible range. The spectrum depicted in red shows a band around 540 nm that reveals the presence of Au-NPs in the gel and is attributed to the surface plasmon resonance of Au. The 540 nm resonance wavelength corresponds to NPs with a non-retarded dipolar resonance. If we assume, as a first approximation, that the NPs are monodisperse with spherical shape and that the refractive index of the surrounding medium is 1.44, Mie calculations (Supporting Information File 1, Section S2) suggest that the 540 nm peak position corresponds to NP diameters between 40 and 50 nm. Note also that the measured plasmon band spans the range from 520 to 800 nm and displays an asymmetric shape with a broader extension toward longer wavelengths. This contrasts with Mie simulations for a given NPs size and suggests that the NPs have a broad polydisperse size and/or shape distribution, with bigger and/or non-spherical NPs resonating on the long wavelength side of the spectrum [24]. Finally, from effective medium simulations (Maxwell–Garnett model) of the measured extinction spectrum, we estimate the volume fraction of Au-NPs to be very small, in the 10^{-4}% to 10^{-3}% range.

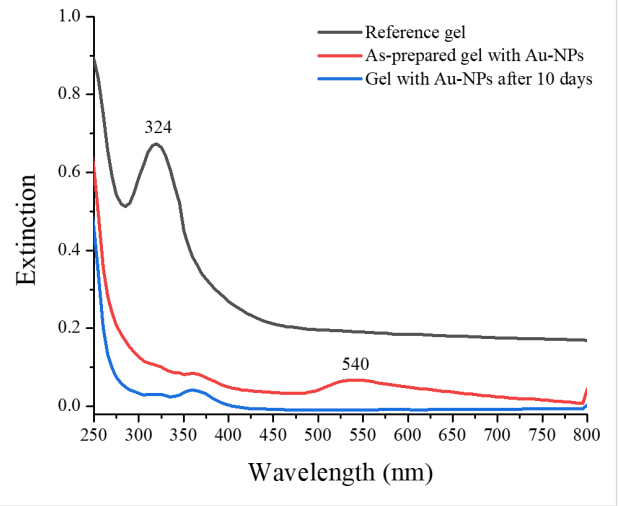

Figure 2: Extinction spectra of the reference gel without Au (black curve), the sol–gel obtained after the ablation of the Au target (red curve), and the same sample with Au-NPs after 10 days (blue curve).

The black spectrum in Figure 2 was recorded 10 days after preparation. The striking feature in this spectrum is that the band corresponding to the well-defined Au plasmon resonance has disappeared and an intense absorption band peaking at 324 nm appeared. Here we provide a preliminary discussion about why this plasmon band has disappeared. While no well-defined plasmon can be seen in the spectrum, there is a broad background, which might result from the presence of bigger NPs, with sizes of hundreds of nanometers, that do not show well-defined plasmon resonances as supported by the Mie simulations shown in Supporting Information File 1, Section S2. In other words, the NPs might have formed bigger structures within the matrix, either by coalescence or Ostwald ripening. Another, yet less likely, possibility is that a significant amount of Au has migrated toward the surface where it formed big NPs, as has been reported in other studies for Ag in glasses and thin films [25,26]. One might also think that the Au-NPs have chemically reacted with the matrix (e.g., Au-OC_2H_5 complexes, the acid inducing oxidation of Au to Au^+) or lost their plasmonic character due to intense chemical interface damping [16,27,28]. However, such effects usually have a strong impact only in the case of few-nanometer NPs, much smaller than in the present case. Note also that the appearance of the band at 324 nm is somewhat simultaneous to the disappearance of the Au plasmon band. This appearance is likely due to changes in the matrix as Au-NPs cannot display plasmon resonances in the UV. Further characterization, beyond the scope of this paper, is needed to definitely address the origin of the observed trends.

Drying and shrinking processes

The drying procedure appears to be crucial for the final result and is still under investigation. There are many publications regarding this aspect of the synthesis of sol–gel glasses [29,30]. Once the sol has been poured into the UV cuvette, the drying process starts. We have measured the weight loss as a function of time, as is shown in Figure 3.

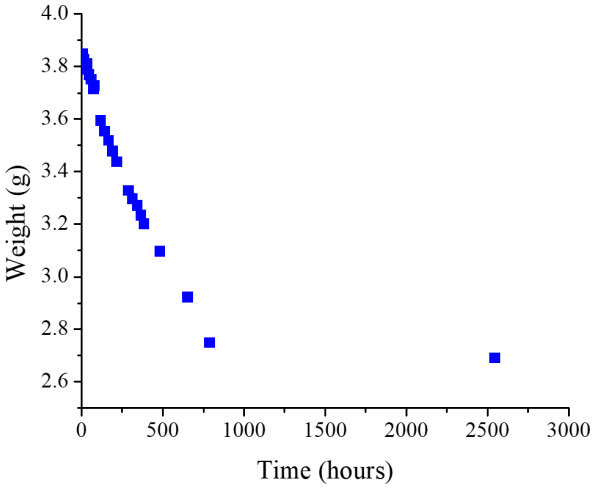

Figure 3: Weight of a sol–gel sample in a cuvette for UV–vis spectroscopy as a function of time.

In the first hour, the evaporation occurs quite fast and if the vessel is not partially sealed, the probability of fracture once the material solidifies is very high. After approximately three months of drying, the sample has shrunk and lost about 30% of its original weight. We have tried to optimize the drying process by changing the vessels, which determine the morphology and size of the glasses, and the sealing procedure. The vessels are covered with a plastic film with some holes to allow evaporation. Best results have been obtained using UV–vis spectroscopy cuvettes designed for 1.5 mL sealed with parafilm with some small holes in it. Just after preparation, the sol–gel solution occupies most of the sample volume of the cuvette (photograph not shown here). In Figure 4 we show the drying–shrinking process. Figure 4a and Figure 4b show the sample one month and two months after preparation, respectively. The final product after three months and after some slight polishing of the top is shown in Figure 4c. It is a quite hard transparent block of glass, $6 \times 2 \times 10$ mm^3 in size. At this stage, the obtained sample is very robust and can be easily manipulated but it is certainly not completely dry. We have examined samples that have dried for up to two years; although the optical properties of the sample exhibit only small changes, we cannot guarantee that they are completely dry.

Regarding the final block shown in Figure 4c, an AFM image reveals a very flat surface as shown later. The only surface that must be polished is the upper one, which maintains the block

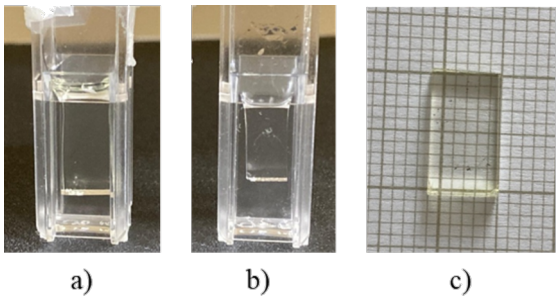

Figure 4: Shrinking process after (a) one month, (b) two months, and (c) three months of drying (images not in scale).

vertically in the cuvette. In the case of gelatins, the drying and shrinking processes are described in Supporting Information File 1, Section S1.

Thermal treatments

In many cases, and depending on the preparation variables used for the synthesis of the nanocomposites, once they have almost completely dried in the form of blocks or thin flat pieces, they can be thermally treated to retrieve the original pink color and the characteristic Au plasmon resonance near 530 nm. Thermal treatments at heating rates ranging from 1 °C/min to 10 °C/min were used. Best results are obtained for slow heating rates and depend on the shape and thickness of the samples. The results and UV–vis spectra are shown in Figure 5. Figure 5a shows a photograph of a piece of glass before (left) and after (right) a thermal treatment at 377 °C for 5 h at a heating rate of 3 °C/min. Figure 5b shows the extinction spectra of a nanocomposite glass with Au-NPs before and after two thermal treatments (TTs), at 377 °C and 500 °C for 5 h each, at a heating rate of 3 °C/min. The Au plasmon at 530 nm is clearly visible over a spectrally broad background; the spectrum of a reference glass (without Au-NPs) after thermal treatment at 500 °C is included for comparison. This suggests that, while large, few-hundred nanometer Au-NPs dominate the broadband optical response of the annealed glass, the annealing has also led to the formation of small, few-nanometer Au-NPs, perhaps from nucleation growth involving atoms that remained isolated in the matrix prior to annealing. The reappearance of the plasmon band also indicates that the Au-NPs that have chemically reacted during ablation [16,28] and revert their oxidation state upon thermal annealing.

Furthermore, we have observed that, after a very long drying process, the original plasmon resonance peak remains. In Figure 6 we show photographs of a reference sample (Figure 6a) and a nanocomposite with gold nanoparticles (Figure 6b) that has dried for six months. The sample on the left side is illuminated in reflection whereas the sample on the right side is illuminated in transmission. For the sample containing Au-NPs, the change in color is evident. Figure 6c and Figure 6d show a sample after two years of drying in transmission and reflection illumination respectively resembling the well-known dichroic effect observed in the Lycurgus cup. In Supporting

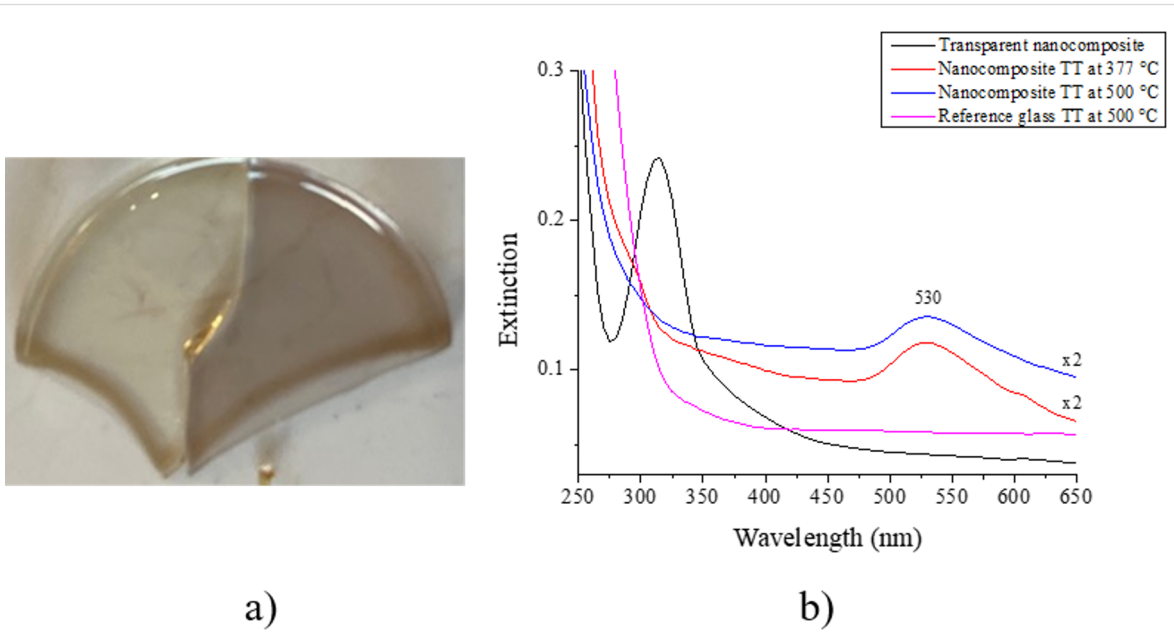

Figure 5: (a) Photograph of a piece of glass before (left) and after (right) thermal treatment at 377 °C, (b) extinction spectra corresponding to the transparent nanocomposite and after two thermal treatments (TTs) at 377 and 500 °C; a reference glass TT at 500 °C is included. Note that the spectra of the thermally treated samples (377 and 500 °C) are scaled (×2) to facilitate comparison.

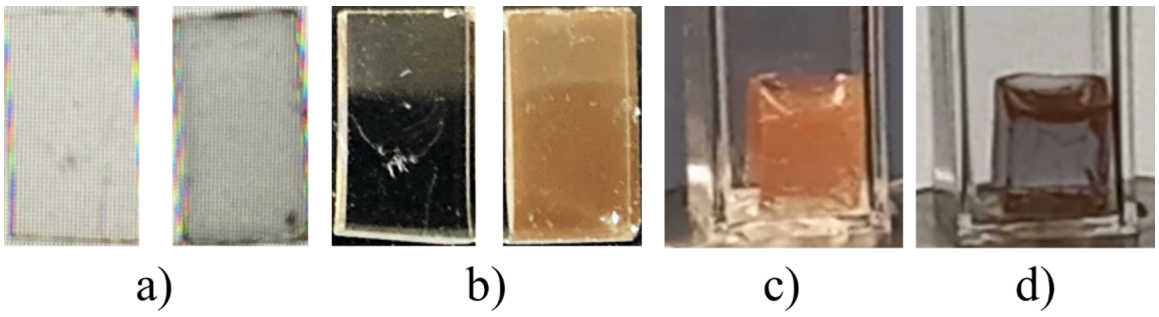

Figure 6: Photographs in transmission and reflection illumination of (a) a reference and (b) a sample with Au-NPs that have dried for six months. A nanocomposite with Au-NPs after two years of drying illuminated in transmission (c) and reflection (d).

Information File 2, we show a video to illustrate this color change in real time for the sample that has dried for two years. As mentioned before, a thermal treatment helps to accelerate the nanocomposite color recovery which is very slow if the glass is left to dry for a long time.

HRTEM characterization

To confirm the presence of Au-NPs in the obtained nanocomposite glasses, we have obtained HRTEM images. Figure 7a shows a high-resolution image in which nanoparticles with an interplanar distance of 0.233 nm, corresponding to the (111) planes of gold, are observed. The EDS spectrum shown in Figure 7b confirms that these are Au nanoparticles. A sample was analyzed by high-angle annular dark-field (HAADF) technique and from some images (Figure 7c shows one of them), sizes ranging from 10 to 43 nm in diameter were measured with an average of 20 nm, determined by analyzing 22 Au-NPs.

AFM characterization

To characterize the surface topography of the synthesized glasses, AFM measurements were performed via non-contact mode measurements. In Figure 8, we can see the smoothness of the surface, with most height values in the ±4 nm range and a mean square roughness of 1.92 nm. This confirms that the glasses have a smooth surface that will not play any role in the optical characterization, as well as opening a pathway for applications as a functional substrate.

Optical characterization

The optical characterization of the glass without Au-NPs was performed in a spectroscopic ellipsometer, covering the wavelength range from UV to NIR (300–1700 nm). The results for refractive index (n) and extinction coefficient (k) are presented in Figure 9. It shows a refractive index close to 1.45 in the UV–vis–NIR, while k remains below the limit of detection of

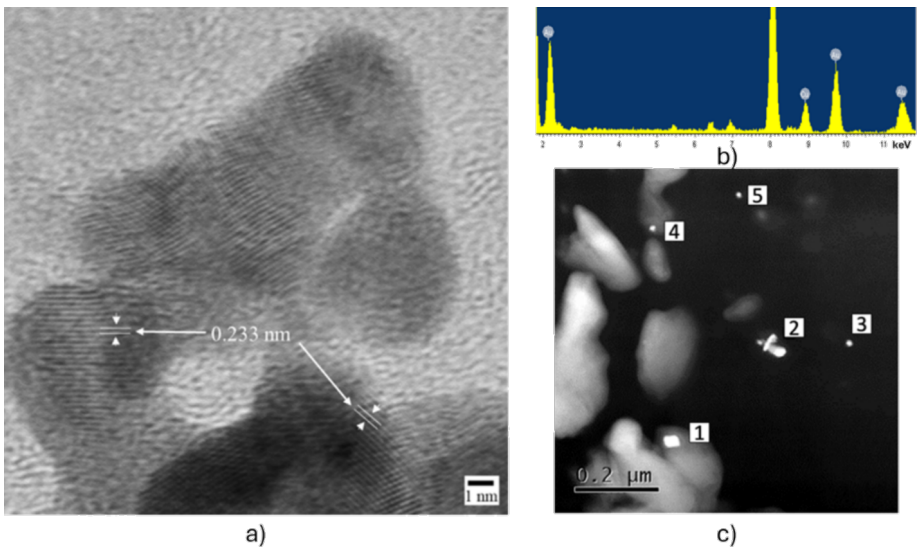

Figure 7: (a) HRTEM image of a nanocomposite sample after two years of drying, (b) EDS spectrum of one Au-NP, (c) HAADF-TEM image showing the presence of Au-NPs.

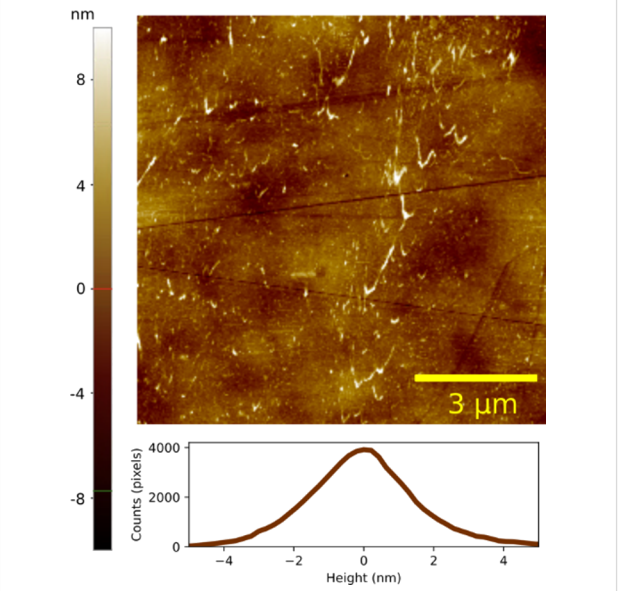

Figure 8: AFM image of a pure glass sample after six months of drying.

the ellipsometer (0.01). Measurements on glasses containing Au-NPs (not presented here) showed similar n and k values, because the volume fraction of NPs in the nanocomposite glass is too small to measurably modify its effective optical constants compared with the glass without NPs.

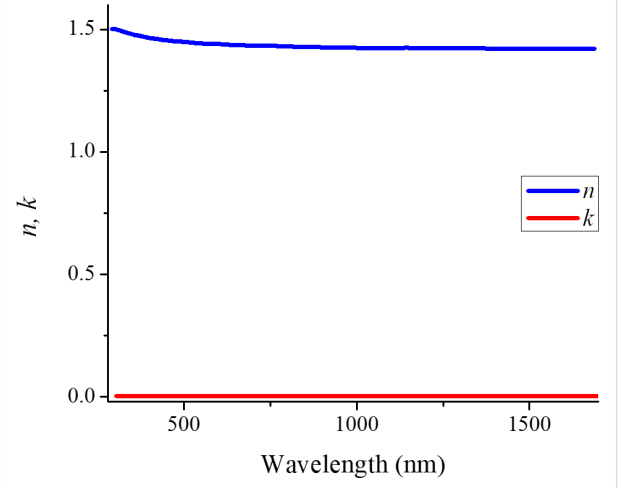

Figure 9: Ellipsometry results for the n and k values in the range from 300 to 1700 nm of a glass without Au-NPs.

Conclusion

In this investigation, we demonstrate the synthesis of nanocomposite glasses and gelatins by combining sol–gel and pulsed laser ablation in liquids techniques. Using this combination, we have been able to embed Au nanoparticles in a silicate matrix as well as in commercial gelatin. The properties of the obtained nanocomposites strongly depend on the laser ablation parameters and on the drying procedure. This versatile experimental approach can be implemented using a broad range of targets and precursors to obtain a wide range of nanocomposite materials with tailored optical properties for potential applications in photonics.

Experimental

The experimental procedure is shown schematically in Figure 10. The reagents used were of analytical grade. The pure (reference) glasses were prepared adding dilute hydrochloric acid as catalyzer to the tetraethyl orthosilicate (TEOS) with a molar ratio of 1:4 (final concentration of 1%). The catalyzer was prepared by adding 0.18 mL of hydrochloric acid to 1.5 mL of deionized water. This was added gradually to 4.74 mL of TEOS under constant stirring until a homogeneous solution was obtained. The sol–gel solution was prepared approximately 1 h before the ablation process. After the ablation, the samples were transferred into 1.5 mL plastic cuvettes for UV spectroscopy and covered partially with parafilm with some holes to let the solvent evaporate.

The solution jellifies after 20 to 30 h and forms a gel that fills the vessel. At this point, the material begins to shrink, which leads to a significant weight loss of up to 30%. This shrinkage occurs over a period of approximately two months. After this process, the sample is a solid block 6 × 2 × 10 mm^3 in size.

For the case of gelatins, the procedure is almost identical; however, the preparation of the solution is simpler and faster since it involves only gelatin and hot tap water. The ablation process is the same, the gelation time is 1 h, and drying occurs typically in three days.

Ablation in sol–gel

The nanocomposite glass was prepared laser-ablating a high purity (99.99%) commercial Au target with a diameter of 2.5 cm and thickness of 0.6 cm, submerged in the sol–gel precursor solution. For this purpose, the target was placed inside a glass cylindrical container with an inner diameter slightly larger than the target diameter to fit it at the bottom of the vessel. Afterwards, 5 mL of the sol were added forming a layer with a thickness close to 1 cm over the target surface. The laser beam was directed by means of mirrors and focused onto the target surface through a lens with 12 cm focal length. Laser ablation was carried out using the fundamental emission of a Nd:YAG laser at a wavelength of 1064 nm and 8 ns of pulse duration working at a repetition rate of 10 Hz. Experiments were performed at a laser energy of 100 mJ in a 2 mm diameter laser spot. The ablation time was typically 10 min; this value was de-

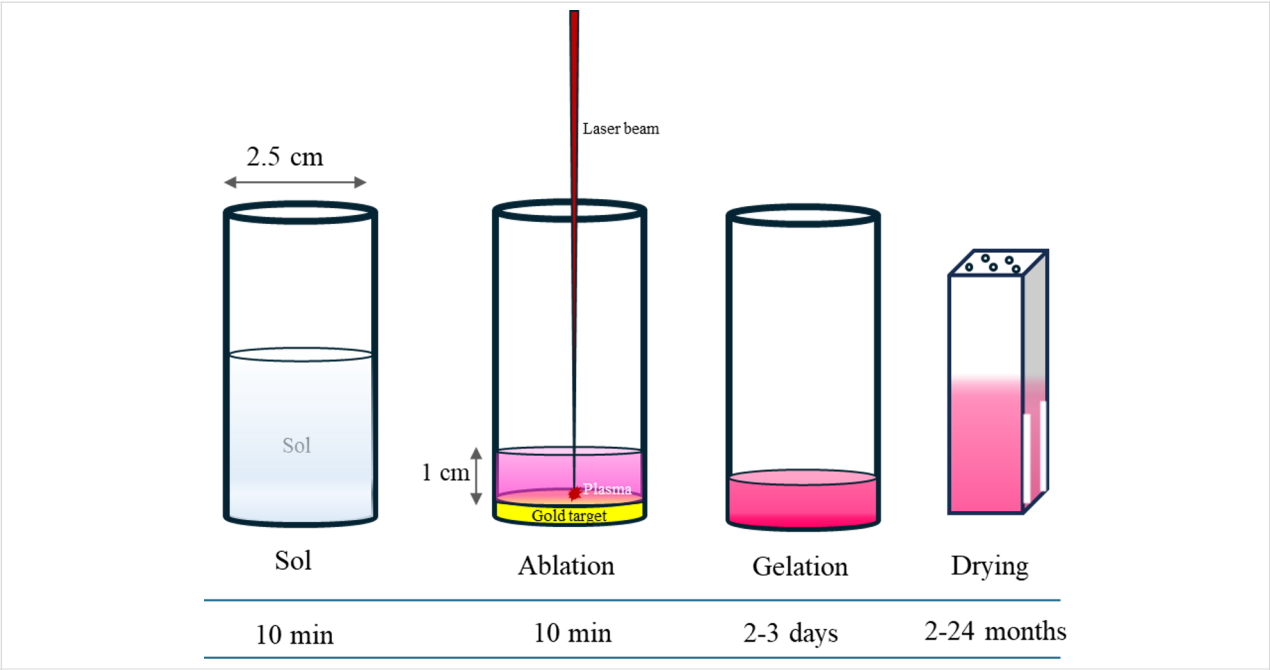

Figure 10: Schematic representation of the synthesis of the nanostructured sol–gel glasses.

termined empirically when observing that the sol turned from transparent to a pink color. The longer the ablation time, the higher the density of nanoparticles; however, the ablation efficiency decreases with time because the suspended Au nanoparticles exert a screening effect on the incident radiation. In the case of gelatins, 1.6 g of commercial pure gelatin were mixed with 62.5 mL of hot (70 °C) tap water under constant stirring for 20 min. Once the temperature decreased to 40 °C, the mixture was poured into the vessel with the Au target for the laser ablation process. The same configuration is used for TEOS and gelatins; however, the preparation parameters are different since the ablation process is more efficient in the gelatin solution than in the TEOS solution. Therefore, for the same energy density, the ablation time was reduced significantly, typically by 50%. In both cases, the presence of gold nanoparticles can be observed readily since the solution exhibits a pink color as shown in Figure 1 and Supporting Information File 1, Figure S1.

The optical properties of the nanocomposites and colloids were characterized by UV–vis spectroscopy with a Varian Cary 2000 double-beam spectrophotometer in transmission configuration at normal incidence. The presence of Au-NPs in the obtained nanocomposites was determined by TEM (JEOL JEM 2100F); for this purpose, the sample was prepared by mechanically grinding in an agate mortar. The powder was placed in a vial with alcohol and ultrasonicated for 30 min to disperse and homogenize it. Afterwards a drop of the obtained suspension was deposited on a formvar-coated Cu grid, allowing the solvent to evaporate completely at room temperature. Specular reflectance was measured with a Woollam VASE ellipsometer. AFM profiles were obtained with a Park XE7 microscope with OML-AC160TS cantilevers in non-contact mode.

Supporting Information

Supporting Information File 1

Gelatin results and Mie simulations.
[https://www.beilstein-journals.org/bjnano/content/supplementary/2190-4286-17-101-S1.pdf]

Supporting Information File 2

Change of color upon illumination.
Video that illustrates the change of color upon illumination in reflection and transmission in real time for the case of the glass sample that has been drying for two years. Video is also available on: https://youtu.be/WKpvlA15s68.
[https://www.beilstein-journals.org/bjnano/content/supplementary/2190-4286-17-101-S2.mp4]

Acknowledgements

We acknowledge the help of J. G. Morales-Méndez, T. Aguilar-Sánchez, A. Limas-Escobar, and A. Hernández-Gordillo in the early stages of this investigation. We thank the Laboratorio Microscopía Electrónica, Universidad Autónoma Metropolitana Iztapalapa for the TEM and HRTEM studies. Special thanks to Dr. Giulio Gorni of the Instituto de Cerámica y Vidrio

of Madrid for advices in the sol–gel preparation of glasses. EHP wishes to thank CK. M. Tibbetts and S. Barcikowski for enlightening discussions.

Funding

We are grateful to the Universidad Autónoma Metropolitana and SECIHTI through grant INFR-2015-255579 ''Infraestructura para Laboratorio de Interacción Radiación Materia y Espectroscopía de Procesos Ultrarrápidos" for their funding. C. A. G. and L. G. M. L. are grateful to SECIHTI for funding through grant 683 in the framework of the ''Investigadores por México" scheme. E. H. P. thanks the Secretaría de Ciencia, Humanidades, Tecnología e Innovación (SECIHTI) of México for financial support. The ININ support through the project CB-004 is acknowledged.

Conflict of Interest

The authors declare that they have no conflicts of interest.

Author Contributions

Emmanuel Haro-Poniatowski: conceptualization; formal analysis; investigation; methodology; supervision; validation; writing – original draft; writing – review & editing. Cesar Augusto Guarín: investigation; validation. Luis Guillermo Mendoza-Luna: investigation; validation; writing – review & editing. Luis Escobar-Alarcón: investigation; validation; writing – original draft; writing – review & editing. José Luis Hernández-Pozos: investigation. L. Irais Vera-Robles: investigation; methodology; writing – original draft. Patricia Castillo: investigation. Fátima Cabello: investigation. Johann Toudert: investigation; writing – original draft; writing – review & editing. Fernando Chacón-Sánchez: investigation. Marina García-Pardo: investigation. Rosalia Serna: conceptualization; investigation. José Gonzalo: investigation. Javier Solís: conceptualization; investigation.

ORCID® iDs

Emmanuel Haro-Poniatowski - https://orcid.org/0000-0001-7172-3335
Luis Guillermo Mendoza-Luna - https://orcid.org/0000-0002-9068-4738
Marina García-Pardo - https://orcid.org/0000-0002-5183-9960
Rosalia Serna - https://orcid.org/0000-0002-7101-3947
José Gonzalo - https://orcid.org/0000-0001-5523-2640
Javier Solís - https://orcid.org/0000-0002-4075-5016

Data Availability Statement

Data generated and analyzed during this study is available from the corresponding author upon reasonable request.

Preprint

A non-peer-reviewed version of this article has been previously published as a preprint: https://arxiv.org/abs/2601.10889

References

1. Freestone, I.; Meeks, N.; Sax, M.; Higgitt, C. *Gold Bull.* **2007,** *40,* 270–277. doi:10.1007/bf03215599
2. Thampi, A. D.; Prasanth, M. A.; Anandu, A. P.; Sneha, E.; Sasidharan, B.; Rani, S. *Mater. Today: Proc.* **2021,** *47,* 4919–4924. doi:10.1016/j.matpr.2021.03.664
3. Singhal, V.; Shelly, D.; Saxena, A.; Gupta, R.; Verma, V. K.; Jain, A. *Lubricants* **2025,** *13,* 93. doi:10.3390/lubricants13020093
4. Olea-Mejía, O.; Brostow, W.; Escobar-Alarcón, L.; Vigueras-Santiago, E. *J. Nanosci. Nanotechnol.* **2012,** *12,* 2750–2755. doi:10.1166/jnn.2012.5737
5. da Costa, P. F. G. M.; Merízio, L. G.; Wolff, N.; Terraschke, H.; de Camargo, A. S. S. *Sci. Rep.* **2024,** *14,* 7884. doi:10.1038/s41598-024-57810-8
6. Xue, J.; Wang, X.; Jeong, J. H.; Yan, X. *Chem. Eng. J.* **2020,** *383,* 123082. doi:10.1016/j.cej.2019.123082
7. Liu, J.; He, H.; Xiao, D.; Yin, S.; Ji, W.; Jiang, S.; Luo, D.; Wang, B.; Liu, Y. *Materials* **2018,** *11,* 1833. doi:10.3390/ma11101833
8. Becerril-Castro, I. B.; Negrín-Montecelo, Y.; Moreno, J.; Correa-Duarte, M. A.; Giannini, V.; Alvarez-Puebla, R. A. *Commun. Chem.* **2024,** *7,* 115. doi:10.1038/s42004-024-01202-6
9. Jiménez de Castro, M.; Cabello, F.; Toudert, J.; Serna, R.; Haro-Poniatowski, E. *Appl. Phys. Lett.* **2014,** *105,* 113102. doi:10.1063/1.4895808
10. Alvarez-Alegria, M.; Siegel, J.; Garcia-Pardo, M.; Cabello, F.; Toudert, J.; Haro-Poniatowski, E.; Serna, R. *Adv. Opt. Mater.* **2022,** *10,* 2101405. doi:10.1002/adom.202101405
11. Haro-Poniatowski, E.; Jiménez de Castro, M.; Fernández Navarro, J. M.; Morhange, J. F.; Ricolleau, C. *Nanotechnology* **2007,** *18,* 315703. doi:10.1088/0957-4484/18/31/315703
12. Cabello, F.; Jiménez de Castro, M.; Mariscal-Jiménez, A.; Cuenda, D.; Serna, R.; Haro-Poniatowski, E. *Ceram. Int.* **2025,** *51,* 55697–55703. doi:10.1016/j.ceramint.2025.09.289
13. Serna, R.; Afonso, C. N.; Ricolleau, C.; Wang, Y.; Zheng, Y.; Gandais, M.; Vickridge, I. *Appl. Phys. A: Mater. Sci. Process.* **2000,** *71,* 583–586. doi:10.1007/s003390000619
14. Olvera-Rodríguez, I.; Hernández, R.; Medel, A.; Guzmán, C.; Escobar-Alarcón, L.; Brillas, E.; Sirés, I.; Esquivel, K. *Sep. Purif. Technol.* **2019,** *224,* 189–198. doi:10.1016/j.seppur.2019.05.020
15. Martínez-Chávez, L. A.; Esquivel, K.; Solis-Casados, D. A.; Velázquez-Castillo, R.; Haro-Poniatowski, E.; Escobar-Alarcón, L. *Appl. Phys. A: Mater. Sci. Process.* **2021,** *127,* 808. doi:10.1007/s00339-021-04957-0
16. Zhang, D.; Gökce, B.; Barcikowski, S. *Chem. Rev.* **2017,** *117,* 3990–4103. doi:10.1021/acs.chemrev.6b00468
17. Svetlichnyi, V. A.; Shabalina, A. V.; Lapin, I. N.; Goncharova, D. A. Metal Oxide Nanoparticle Preparation by Pulsed Laser Ablation of Metallic Targets in Liquid. In *Applications of Laser Ablation - Thin Film Deposition, Nanomaterial Synthesis and Surface Modification;* Yang, D., Ed.; InTech, 2016. doi:10.5772/65430
18. Ye, F.; Musselman, K. P. *APL Mater.* **2024,** *12,* 050602. doi:10.1063/5.0199104
19. Escobar-Alarcón, L.; Espinosa-Pesqueira, M. E.; Solis-Casados, D. A.; Gonzalo, J.; Solis, J.; Martinez-Orts, M.; Haro-Poniatowski, E. *Appl. Phys. A: Mater. Sci. Process.* **2018,** *124,* 141. doi:10.1007/s00339-018-1559-8

20. Lau, M.; Waag, F.; Barcikowski, S. *Ind. Eng. Chem. Res.* **2017,** *56,* 3291–3296. doi:10.1021/acs.iecr.7b00039
21. Salminen, T.; Honkanen, M.; Niemi, T. *Phys. Chem. Chem. Phys.* **2013,** *15,* 3047–3051. doi:10.1039/c2cp42999c
22. Luo, N.-Q.; Huang, Z.-Y.; Li, L.; Shao, Y.-Z.; Chen, D.-H. *Chin. Phys. Lett.* **2013,** *30,* 038101. doi:10.1088/0256-307x/30/3/038101
23. Haro-Poniatowski, E. Proceso para la fabricación de matrices nanoestructuradas embebidas con nanopartículas. Instituto Mexicano de la Propiedad Industrial. MX 415245 B, July 17, 2024.
24. Toudert, J.; Simonot, L.; Camelio, S.; Babonneau, D. *Phys. Rev. B* **2012,** *86,* 045415. doi:10.1103/physrevb.86.045415
25. Camelio, S.; Babonneau, D.; Girardeau, T.; Toudert, J.; Lignou, F.; Denanot, M.-F.; Maître, N.; Barranco, A.; Guérin, P. *Appl. Opt.* **2003,** *42,* 674–681. doi:10.1364/ao.42.000674
26. Fernández Navarro, J. M.; Toudert, J.; Rodríguez-Lazcano, Y.; Maté, B.; Jiménez de Castro, M. *Appl. Phys. B: Lasers Opt.* **2013,** *113,* 205–213. doi:10.1007/s00340-013-5458-6
27. Hövel, H.; Fritz, S.; Hilger, A.; Kreibig, U.; Vollmer, M. *Phys. Rev. B* **1993,** *48,* 18178–18188. doi:10.1103/physrevb.48.18178
28. Moore Tibbetts, K.; Tangeysh, B.; Odhner, J. H.; Levis, R. J. *J. Phys. Chem. A* **2016,** *120,* 3562–3569. doi:10.1021/acs.jpca.6b03163
29. Kajihara, K. *J. Asian Ceram. Soc.* **2013,** *1,* 121–133. doi:10.1016/j.jascer.2013.04.002
30. Kajihara, K.; Kanamori, K.; Shimojima, A. *J. Ceram. Soc. Jpn.* **2022,** *130,* 575–583. doi:10.2109/jcersj2.22078

License and Terms

This is an open access article licensed under the terms of the Beilstein-Institut Open Access License Agreement (https://www.beilstein-journals.org/bjnano/terms), which is identical to the Creative Commons Attribution 4.0 International License (https://creativecommons.org/licenses/by/4.0). The reuse of material under this license requires that the author(s), source and license are credited. Third-party material in this article could be subject to other licenses (typically indicated in the credit line), and in this case, users are required to obtain permission from the license holder to reuse the material.

The definitive version of this article is the electronic one which can be found at:
https://doi.org/10.3762/bjnano.17.101

BEILSTEIN JOURNAL OF NANOTECHNOLOGY

Kinetically controlled boron carbide composite sub-micrometer particle formation pathways during continuous-flow laser melting in liquids with high-power lasers

Nico G. Koch[1], Christoph Rehbock[1], Naoto Koshizaki[2] and Stephan Barcikowski[*1]

Full Research Paper

Open Access

Address:
[1]Technical Chemistry I and Center for Nanointegration Duisburg-Essen (CENIDE), University of Duisburg-Essen, Universitätsstraße 7, 45141 Essen, Germany and [2]Graduate School of Engineering, Hokkaido University, Sapporo, Japan

Email:
Stephan Barcikowski* - stephan.barcikowski@uni-due.de

* Corresponding author

Keywords:
boron carbide nanoparticles; continuous nanomaterial production; flow-through reactor; hard ceramics; pulsed laser melting in liquids; sub-micrometer spheres (SMSs)

Beilstein J. Nanotechnol. **2026,** *17,* 1582–1595.
https://doi.org/10.3762/bjnano.17.108

Received: 10 July 2026
Accepted: 12 October 2026
Published: 10 November 2026

This article is part of the thematic issue "Laser material processing in liquids for nanoparticle synthesis".

Guest Editor: G. Mínguez-Vega

© 2026 Koch et al.; licensee Beilstein-Institut.
License and terms: see end of document.

Abstract

Monodisperse, spherical sub-micrometer particles with clean, smooth surfaces are key materials used as composite reinforcements, abrasives, and tribological additives, but remain synthetically challenging to produce. Pulsed laser melting in liquids (LML) is an environmentally friendly, emerging route for producing such particles. However, demonstrations have so far been limited to batch reactors, which are difficult to scale up to industrial production. Here, we extend laser melting in liquids to a continuous flat jet flow-through reactor in which boron carbide composite nanoparticles (B_4CC) dispersed in ethanol are fed perpendicular to a nanosecond pulsed high-power ultraviolet laser beam; this is complemented by additional experiments employing pristine boron carbide. We elucidate how flow conditions and the application of modern high-repetition-rate lasers alter particle formation pathways. Characterization of B_4CC, irradiated at fluences of 45–135 mJ·cm^{-2}, by transmission electron microscopy and dynamic light scattering, evidences the formation of a bimodal size distribution of spherical particles with mean diameters of ≈50 and ≈100 nm, verifying the parallel occurrence of isochoric reshaping and an aggregation–melting–fusion mechanism. While the smaller particle size fraction formed in accordance with thermal equilibrium calculations, the second size mode, derived from a multistep aggregation–melt–fusion pathway, was significantly smaller than predicted. Systematic variation of the number of laser pulses per unit volume (PPV) from 1 to 16 by tuning the interpulse delay (τ_{IP}) from 1.4 to 0.1 ms revealed an initial increase of the mean diameter of the second mode with PPV, reaching maximum size at 4 PPV. Interestingly, at higher PPV, further particle growth is arrested, probably due to an interplay between low particle mass concentration and shorter τ_{IP} limiting the number of aggregation–melt–fusion steps, indicating kinetically controlled particle formation pathways. If the laser fluence is increased to

180 mJ·cm^{-2}, laser fragmentation in liquid prevails, and small mass fractions of ultrasmall nanoparticles (approx. 2 nm) are formed, which constitutes the upper limit of the LML process window. Overall, at the example of the ultrahard material boron carbide, difficult to process by other methods into perfect spheres, kinetically controlled LML in a flat jet flow-through reactor gives access to nanostructures in a size range previously unattainable by laser processing, establishing the basis for upscaling production in liquid flow with matched laser pulse numbers.

Introduction

Hard ceramic sub-micrometer spheres (SMSs) represent a class of materials with exceptional mechanical and chemical stability, rendering them indispensable for emerging technologies [1,2]. Their relevance spans a wide range of applications, including composite reinforcements [3-5], abrasives [6-8], drilling materials [9,10], and solid lubricant systems [11-13]. Hardness, crystallinity, and particle size distribution are the major physicochemical properties that determine the performance of ceramic SMSs in these applications; these properties are primarily dictated by the synthesis route [14,15]. Conventional synthesis methods, however, face substantial limitations in meeting the stringent purity, crystallinity, and particle size requirements to tune the SMSs to their corresponding application. Among ceramics, boron carbide (B_4C) is particularly noteworthy due to its outstanding hardness, ranking among the highest on the Mohs scale (about 9.5) [16]. Despite its favorable characteristics, boron carbide synthesis and processing pose considerable challenges. While several synthesis routes have been explored for boron carbide nanoparticles (NPs) and SMSs, each presents inherent limitations regarding crystallinity, dispersibility, or size control. Solvothermal and wet-chemical approaches typically yield amorphous or poorly crystalline products that exhibit pronounced aggregation [17,18], whereas chemical vapor deposition [19-21] can produce highly crystalline B_4C but suffers from formation of polydisperse particles and limited scalability. As a result, the fabrication of well-dispersed, crystalline, and smooth-surfaced B_4C spheres with monomodal size distributions remains challenging. This difficulty is further amplified during particle comminution, as the pronounced hardness and intrinsic brittleness of B_4C severely hinder mechanical size reduction and homogenization. Aligned with the chemical industry's ongoing transition toward greener and more sustainable manufacturing paradigms [22,23], pulsed laser melting in liquid (LML) has emerged as an attractive approach for NP processing [24]. The technique relies solely on electrical energy (to create the laser beam), which can be sourced renewably. But also the role of the liquid (which in the case of ethanol may not be fully recyclable) needs to be considered. For more details on LML-specific sustainability aspects, we refer to the recent assessment of the four variants of laser synthesis and processing of colloids regarding the twelve green chemistry criteria [25]. Ethanol was selected as the liquid medium because aqueous processing may promote oxidation [26] and hydrolysis of boron-containing species under the high-temperature conditions generated during laser processing; in contrast, ethanol provides a less oxidizing environment but may additionally generate transient carbonaceous species through solvent decomposition [27]. To date, boron carbide SMSs produced by LML of feedstock NPs have been exclusively generated based on boron NPs, which are transformed into boron carbide SMSs due to the incorporation of carbonaceous radicals from solvent decomposition [24]. This kind of reactive LML relies on a complex design where physical particle melting and chemical reactions have to be controlled in parallel. It necessitates multipulse processing and irradiation times up to 60 min in batch reactors. A simpler and potentially more robust LML synthesis route where B_4C SMSs are formed directly from B_4C NPs has rarely been investigated, mainly because synthesizing B_4C NP starting materials is more challenging, and commercial availability is limited [28]. Direct processing of pre-formed B_4C NPs offers the advantage of bypassing the kinetically demanding incorporation of carbon into molten boron, which is particularly relevant for short-residence-time, continuous high-throughput processing. In this way, the use of B_4C feedstock can facilitate the formation of stoichiometric and phase-pure B_4C spheres without requiring an additional carbonization step during laser processing, provided that the starting material already meets the required phase-purity specifications. Previous investigations demonstrated that four pulses are sufficient to induce SMS formation under batch conditions using boron [29]. However, this pulse number proves inadequate for a quantitative conversion of elemental boron to boron carbide. Higher-repetition-rate lasers would facilitate higher-pulse-number applications in both batch and flow-through reactors. However, to date, almost all LML-based approaches have been conducted in batch or guided-flow configurations coupled with Nd:YAG lasers operating at low repetition rates (typically around 10 Hz) [24,28,30,31]. These systems inherently limit throughput and scalability and are hardly suitable for the scale-up of boron carbide SMS synthesis by LML [29]. Even existing guided-flow reactors have deep liquid paths and turbulent back-mixing, leading to severe optical shielding, non-uniform fluence profiles, and undefined irradiation histories per particle. The integration of a high-repetition-rate laser into a continuous-flow flat jet LML platform

thus fundamentally advances previous LML approaches. Although laser systems with high pulse energy allow for a significant increase in the irradiated volume at equivalent fluence, this enlargement causes pronounced shielding effects in the irradiated volume. These effects occur when particles or created bubbles absorb or scatter the laser beam, leading to steep fluence gradients within the irradiated volume, strongly influencing the LML process and SMS quality. Here, regions experiencing higher fluence yield different particle sizes or morphologies compared to areas exposed to lower fluence. These nonuniform energy distributions compromise control over particle size and homogeneity, which is critical for scalability. To overcome these obstacles, scale-up approaches necessitate switching from large-volume batches to smaller irradiated volumes realized in continuous liquid-flow reactors, where throughput is controlled by the volume flow rate [32].

The current state of the art in scaled up laser synthesis and processing of colloids is based on the utilization of high-power lasers (up to 400 W) operated at kilohertz-to-megahertz repetition rates, frequently combined with advanced continuous liquid-jet setups applicable for laser fragmentation in liquids (LFL) [33-35] and pulsed laser defect engineering in liquids [36,37], where throughputs of several grams per hour have been realized [34,37,38]. Such advanced laser-processing setups have not been used in the context of LML. There, they could dramatically increase the number of laser pulses available for continuous processing, while maintaining a stable interaction zone that minimizes self-focusing and defocusing effects. However, a critical challenge at such high repetition rates arises from heat buildup [39]. If the pulse sequences are too fast, the particle will not fully cool down before the next pulse hits it. This may cause a further increase in the particle's temperature by heat accumulation, which promotes fragmentation [40]. These thermally driven nonlinearities, furthermore, fundamentally impair uniform and controlled formation of SMSs as they introduce fluctuations in aggregation kinetics [41,42] and transport of reactive intermediates [43]. Such considerations, however, reveal an intrinsic mismatch between simplified theoretical models and experimental observations. The model proposed by Koshizaki et al. predicts cooling times for molten SMSs of the order of milliseconds, rationalizing heat accumulation onset at repetition rates exceeding 400 Hz [40]. In contrast, recent studies report cooling rates for SMS-regime particles approaching 10^9 K·s^{-1} [44-46], implying that an SMS or molten aggregate at 4000 K returns to ambient temperature within about 4 μs. This estimate, however, reflects only the maximum cooling rate at the onset of heat transfer, when the temperature difference between particle and liquid is largest. As the particle cools, the temperature gradient and thus the instantaneous cooling rate decrease continuously. Consequently, the total cooling time to room temperature can be expected to be roughly one order of magnitude larger, corresponding to an effective average cooling rate of about 10^8 K·s^{-1}. Nonetheless, LML in batch setups demonstrates the formation of substantially smaller NP fractions already at 0.4 kHz, corresponding to cooling times of about 2.5 ms and indicating fragmentation under ostensibly thermally benign conditions [40]. This unresolved discrepancy, spanning nearly three orders of magnitude between theory (particle cooling time) and experiment (time between two pulses), likely originates from batch configuration characteristics that introduce unmodeled thermal and hydrodynamic effects. Such effects can be disentangled by implementing a flat jet flow-through reactor into LML research, where fluence deviations are minimal and the number of pulses per volume (PPV) can be precisely tuned [36]. Thereby, LML processes may be meticulously mechanistically explored and further adapted to function in high-throughput, high-power, and high-repetition-rate laser setups.

In the current study, we examine the extent to which steady-state high-power laser processing in flowing ethanol can be used for the scalable synthesis of boron carbide SMSs. This experimental design may be further utilized to study particle formation pathways under kinetic control, contrasting thermodynamic equilibrium conditions during batch processing, well described and established in the literature. Hence, in contrast to the state-of-the-art LML, we utilize the following methodological innovations: (i) boron carbide composite (B_4CC) as feedstock material instead of boron, aiming at faster processing with a lower number of laser pulses, (ii) a thin flat jet flow-through reactor that minimizes fluence gradients along the laser beam path, which enables uniform flow conditions and a precise setting of the PPV for the whole processed volume, and (iii) a high-repetition-rate laser (10 kHz) with a hundred times lower pulse intervals, potentially shorter than the particle cooling time between pulses.

Transmission and scanning electron microscopy (TEM and SEM) are employed to evaluate morphological changes, while dynamic light scattering (DLS) provides quantitative insight into size distributions. Together, these analyses elucidate the relationship between laser parameters, SMS formation mechanisms, and the resulting material properties in the underexplored kinetically controlled particle formation regime during LML. Ultimately, this study seeks to bridge the conceptual divide between fundamental laser–matter interaction physics and the practical requirements of scalable SMS production. By demonstrating the feasibility of a high-frequency UV-nanosesond-LML process within a flat jet geometry, the work establishes a pathway for future mechanistic studies and process optimization. A demonstrative scale-up emphasizes the

application relevance of this methodology and its potential contribution to sustainable nanomaterials manufacturing if fully optimized. The general concept and the design of the study are illustrated in Figure 1.

Experimental

Pulsed laser melting in liquid

The B_4C particles (mean particle diameter of 40–80 nm according to the manufacturer) were purchased from Nanografi [47] and dispersed in absolute ethanol (99.8%, VWR) using a Hielscher UP200ST [48] sonotrode operated at 100 W for 10 min. For purification, the suspension was subsequently filtered through a syringe filter (76479-060, VWR) to remove residual large feedstock particles with a cutoff above 100 nm. For each experiment, 100 mL feedstock suspension was prepared, with a B_4C mass concentration of 250 mg·L^{-1}. Since the LML process was operated as a closed-loop recirculation process without intentional mass removal, the overall particle concentration remained constant throughout laser processing. Solvent evaporation was negligible under the employed conditions, and any minor evaporated solvent was condensed within the closed flow system. Laser processing was conducted using a UV nanosecond laser system (Trumpf TruMicro 8340, 400 Watt at 10 kHz, 18 ns, 343 nm) integrated into a flat jet setup developed within the research group (Supporting Information File 1, Figure S1). The average laser power was monitored using the integrated measurement tool of the Trumpf laser system. The laser beam was focused to a spot size of 0.12 cm^2 (2 mm by 8 mm) using a Thorlabs cylindrical lens with a focal length of 500 mm. The resulting fluence values calculated from this profile may be subject to systematic error due to the spot size measurement. Based on the specifications of the beam profiling camera (Ophir SP932U), the estimated systematic measurement uncertainty of the beam diameter is 2%. However, as all measurements were performed within an identical experimental setup, this potential offset remains constant and does not affect the comparative validity or relative trends reported in this study. The liquid jet was generated by a 90° nozzle (NF90303BSP, BETE Spray Technology), producing a laminar liquid layer with a thickness of 35 µm as determined by UV–vis extinction spectroscopy (Flame, Ocean Optic, Supporting Information File 1, Figure S2). This configuration eliminates both laser refraction at the air–liquid interface and liquid backmixing phenomena, thus ensuring reproducible laser–matter interactions under defined optical and hydrodynamic conditions. Quantitative evaluation of the medium's absorption behavior was performed using the Beer–Lambert's law, enabling the correlation of optical absorbance with solute concentration for precise process control. To selectively capture the laser-excited volume fraction, a custom-built mechanical separation unit of 3 mm redirects unirradiated fractions into a closed-loop recirculation pathway, thereby efficiently using the feedstock

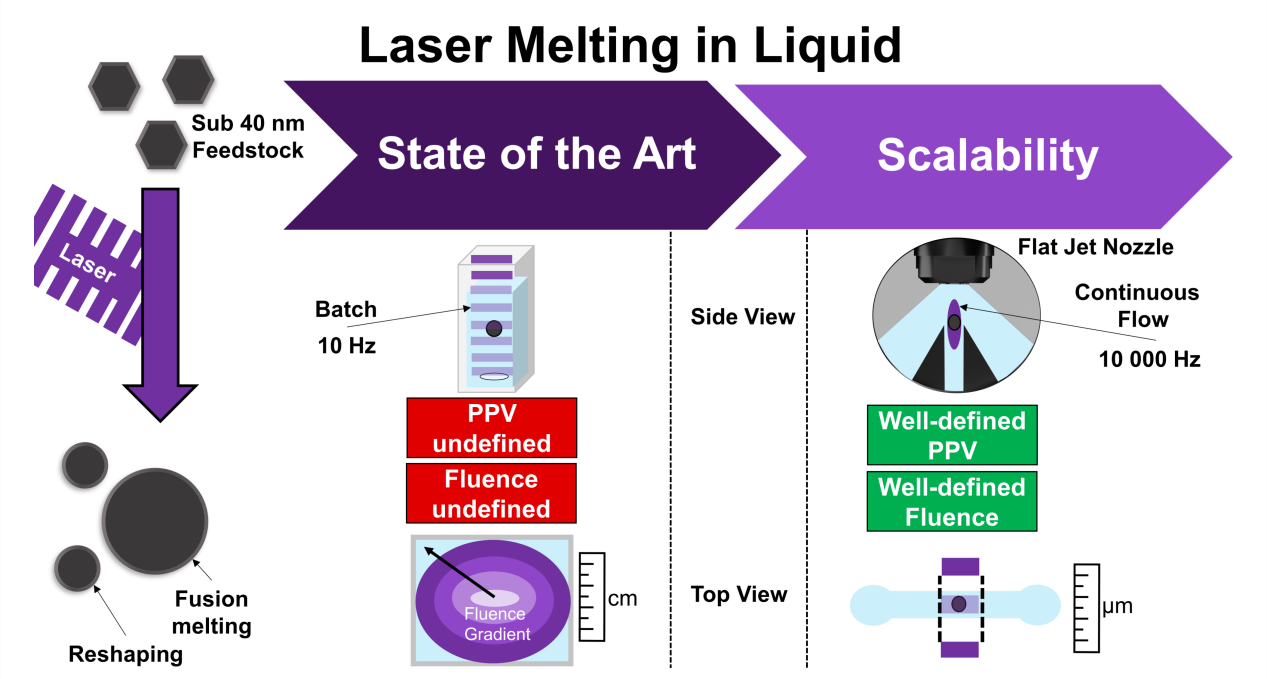

Figure 1: General concept of the LML transition to high-power flow-through setups coupled with a flat jet approach. Left: The two particle formation pathways of isochoric reshaping and aggregation–melting–fusion, both simultaneously occurring during LML. Middle: General shortcomings of established batch setups for LML are characterized by undefined irradiation conditions (fluence and PPV). Right: Schematic setup of the flat jet flow-through setup used in this work to overcome the limitations of batch processing.

material (Supporting Information File 1, Figure S1). The separation knives need to have a safety distance (0.5 mm) from the laser beam edge, so that only 66% of the volume collected downstream was processed by LML (2 mm laser and 3 mm separation width). The experiments at varying fluence were performed at a constant repetition rate of 10 kHz and a laser power between 200 and 400 W and 16 PPV. The volumetric flow rate of the treated suspension was maintained at 20 mL·min^{-1} using an Ismatec REGLO-Z pump. The calculated Reynolds number of 147 (see Supporting Information File 1 for further information) and low pump pulsation indicate operation within a non-turbulent regime, ensuring reproducible layer thickness and minimal flow fluctuations. For PPV studies, an integrated divider module was employed to adjust the laser output repetition rate (0.7–10 kHz) and thereby the PPV within a range from 1 to 16. This results in interpulse delays from 0.1 to 1.4 ms (see Supporting Information File 1, Section S4, Table S1).

X-ray photoelectron spectroscopy

To prepare the sample for X-ray photoelectron spectroscopy (XPS) analysis, the powdered material was pressed directly onto an indium film substrate. XPS measurements were conducted using a JEOL JPS-9200 spectrometer equipped with a monochromate Al Kα X-ray source. An electron neutralizer was utilized during data acquisition to compensate for surface charging effects. Spectral deconvolution and quantitative analysis were performed using standard fitting procedures. A Shirley-type background subtraction was applied to isolate the core-level signals. Peak fitting was carried out using a mixed Gaussian–Lorentzian line shape, where the Gaussian-to-Lorentzian mixing ratio was treated as an adjustable parameter during the fitting process.

Electron microscopy

To prepare the electron microscopy samples, the NP suspensions were concentrated using a centrifuge (Hettich Micro 220) with a nominal cutoff of 50 nm. The collected particles were subsequently washed three times with high-purity ethanol under identical centrifugation conditions to remove residual impurities originating from thermal ethanol decomposition. For transmission electron microscopy (TEM) analysis, 5 µL of the purified suspension was deposited onto a carbon-coated copper TEM grid, whereas for scanning electron microscopy (SEM), the suspension was dripped onto a polished silicon wafer. In both cases, the solvent was allowed to evaporate under ambient conditions. TEM imaging was carried out using a JEOL JEM 1400 Plus operated at 200 kV, while SEM characterization was conducted with a Thermo Scientific Magna Ray WDS Spectrometer. Image analysis and particle size evaluation were performed using the Fiji software package, measuring at least n = 250 particles.

Dynamic light scattering

Dynamic light scattering (DLS) measurements were conducted using a Zetasizer ZS90 (Malvern Instruments). The optical transmission of each sample was adjusted to approximately 70% using anhydrous ethanol as the solvent. A volume of 5 mL of the resulting suspension was transferred to a quartz cuvette, and measurements were performed in backscattering mode at 173°. The sample temperature was maintained at 25 °C throughout the experiment. To ensure statistical reliability, each sample was measured in triplicate, with three measurement cycles per replicate.

X-ray diffraction

X-ray diffraction (XRD) analysis was performed using a Bruker D2 Phaser benchtop diffractometer equipped with Cu Kα radiation (λ = 1.54056 Å). Approximately 100 mg of powdered samples were loaded onto a spinner reflection stage for enhanced angular reproducibility. The feedstock B_4CC powder was analyzed directly as received from the commercial manufacturer without further treatment. For the laser-treated samples, the processed nanoparticle dispersion was collected after LML processing, concentrated by centrifugation, and dried at 60 °C to obtain the powder required for XRD analysis. Data were acquired over a 2θ range of 5–90° at a step size of 0.01214° and a step time of 3.6 s per step.

Thermogravimetric analysis

Thermogravimetric analysis (TGA) was performed using a Shimadzu TGA-50 thermal analyzer. The solid sample was weighed directly into an alumina crucible with an initial sample mass between 3 and 5 mg. Measurements were conducted under a nitrogen/oxygen atmosphere with a continuous purge flow rate of 20 mL·min^{-1}. The temperature program consisted of dynamic heating from room temperature (approx. 25 °C) to a maximum temperature of 1000 °C at a constant heating rate of 25 °C·min^{-1}. Sample mass loss and the corresponding derivative thermogravimetric signal were recorded continuously throughout the temperature range.

Results and Discussion

Feedstock nanoparticle characterization

To investigate the transferability of the LML process to continuous flow in a flat jet, a thorough characterization of the feedstock NPs is essential. To this end, we analyzed the feedstock particles by XRD, XPS, and TGA, verifying that we work with a boron carbide composite (B_4CC) containing 21 wt % of boron carbide, as well as fractions of graphitic carbon and boron oxide. However, as carbon does not form stable SMSs at atmospheric pressure, it evaporates at 3642 °C [49], we can assume that SMSs formed from B_4CC are mainly composed of B_4C, although fractions of B or B_2O_3 in the particles cannot be

excluded. As the SMSs generated by LML from pure B_4C show similar particle diameters and shapes (Supporting Information File 1, Figure S3), we can assume that the herein used B_4CC is suitable for mechanistic studies of LML (Supporting Information File 1, Section S2). Although the two feedstock materials have markedly different crystal structures, XRD analysis shows that their response is similar after LML. Notably, all diffraction features attributable to boron oxide disappear after processing, suggesting complete removal rather than reduction below the detection limit. This transformation occurs regardless of the initial crystallographic state, demonstrating that oxide formation is not only suppressed, but also effectively eliminated under the applied LML conditions, probably attributed to reductive environments frequently reported during LML in organic solvents [27]. To explain why we used B_4CC feedstock rather than the B_4C reference, we need to examine the particle size distribution of both (Supporting Information File 1, Figure S3). As we wanted to obtain scientific results based specifically on the aggregation–fusion–melting process, the broader particle size distribution of the B_4C resulted in overlap between aggregation, melting, fusion, and isochoric reshaping. Therefore, although it is a composite, we used the B_4CC due to its narrower size distribution and overall smaller mean particle diameters in the feedstock powder.

Fluence study

TEM analysis of the B_4CC feedstock particles predominantly shows a hexagonal morphology according to the manufacturer's specifications [47], as validated in Figure 2A. It is noteworthy, however, that particles smaller than 40 nm do not consistently possess a perfect hexagonal shape; some display rounded edges, though they remain distinctly non-spherical. The initial particle diameter distribution follows a characteristic log-normal profile, confirmed by TEM (Supporting Information File 1, Figure S5). The mean value from TEM is about 30 nm with a standard deviation of ±12 nm. These findings align with the manufacturer's specifications, which indicate particle diameters in the range of 40 to 80 nm. The observed shift towards smaller particles below 40 nm is primarily attributed to the feedstock suspension purification steps described in the Experimental section. This initial characterization establishes a reliable baseline, enabling unambiguous attribution of any subsequent structural or morphological changes to laser–material interactions during the LML process. Owing to the inherent mechanisms of laser–particle interactions described by the heating–melting–evaporation (HME) model established by Koshizaki et al. for LML [50,51], the LML treatment is expected to yield a bimodal particle size distribution. According to this model, a given fluence has two particle size values in the bathtub-shaped fluence–diameter diagram (reaching the melting onset temperature). The feedstock particle size is already in the range of the first intersection (at the smaller size), but the formation of significantly larger molten spheres of the second melting-onset size would require the particles to fuse. This means that the smaller population arises from surface reshaping of pre-existing particles (including smaller agglomerates), while the larger sizes may only originate from aggregation–melting–fusion, as illustrated in Figure 2A. The corresponding bimodal size distribution pattern is corroborated by the DLS data in Figure 2B, where two distinct peaks can be assigned to the respective SMS sizes depicted in Figure 2A. TEM analysis also reveals a bimodal size distribution with a higher particle density (n = 2500) compared to Figure S5 (Supporting Information File 1).

The laser fluence window is a key parameter that controls the initiation and progression of LML, and it particularly dictates the maximum SMS diameter meltable under thermodynamic control [51]. Fundamental studies by Koshizaki et al. have repeatedly demonstrated that carefully defining this window is essential for achieving controlled transformations during LML. Over the past two decades, increasingly advanced theoretical models have been developed to predict the lower and upper boundaries of the effective LML fluence range [50,51]. In the present study, we further advance the quantitative model introduced by Sakaki et al. [51] to describe the fluence-dependent LML threshold under the specific optical and thermal boundary conditions of our system. This model was extended to include the upper fluence limit associated with the LFL regime [45]. We experimentally determined the fluence at which LFL begins and, using the HME model, marked the corresponding particle temperature as the onset of LFL. All simulated temperatures above this threshold are shown in the profiles as a white "bathtub area" (further information and model code are provided in Section S4 of Supporting Information File 1). In both the black LML area and the white LFL area, only the temperatures required to trigger or initiate LML or LFL are reached. Consequently, it cannot be guaranteed that LML and LFL will fully develop; instead, the two mechanisms may partially overlap. Recent studies by Zhigilei et al. [52] have shown that, under laser irradiation, the solvent may reach supercritical conditions at the surface. The transition substantially modifies heat transfer at the nanoparticle–liquid interface and is therefore expected to shift the effective fluence during laser melting in liquids toward higher values. However, the present model should be interpreted with caution and not as a quantitatively predictive framework. Experimental analysis revealed that the purchased B_4CC feedstock does not exhibit ideal purity, as detailed in Supporting Information File 1 (Section S2), but could also contain fractions of C and B_2O_3. Despite this, the simulations were deliberately performed assuming pure B_4C. This approach enables the use of well-established literature parameters and avoids the introduction of multiple poorly constrained assumptions regard-

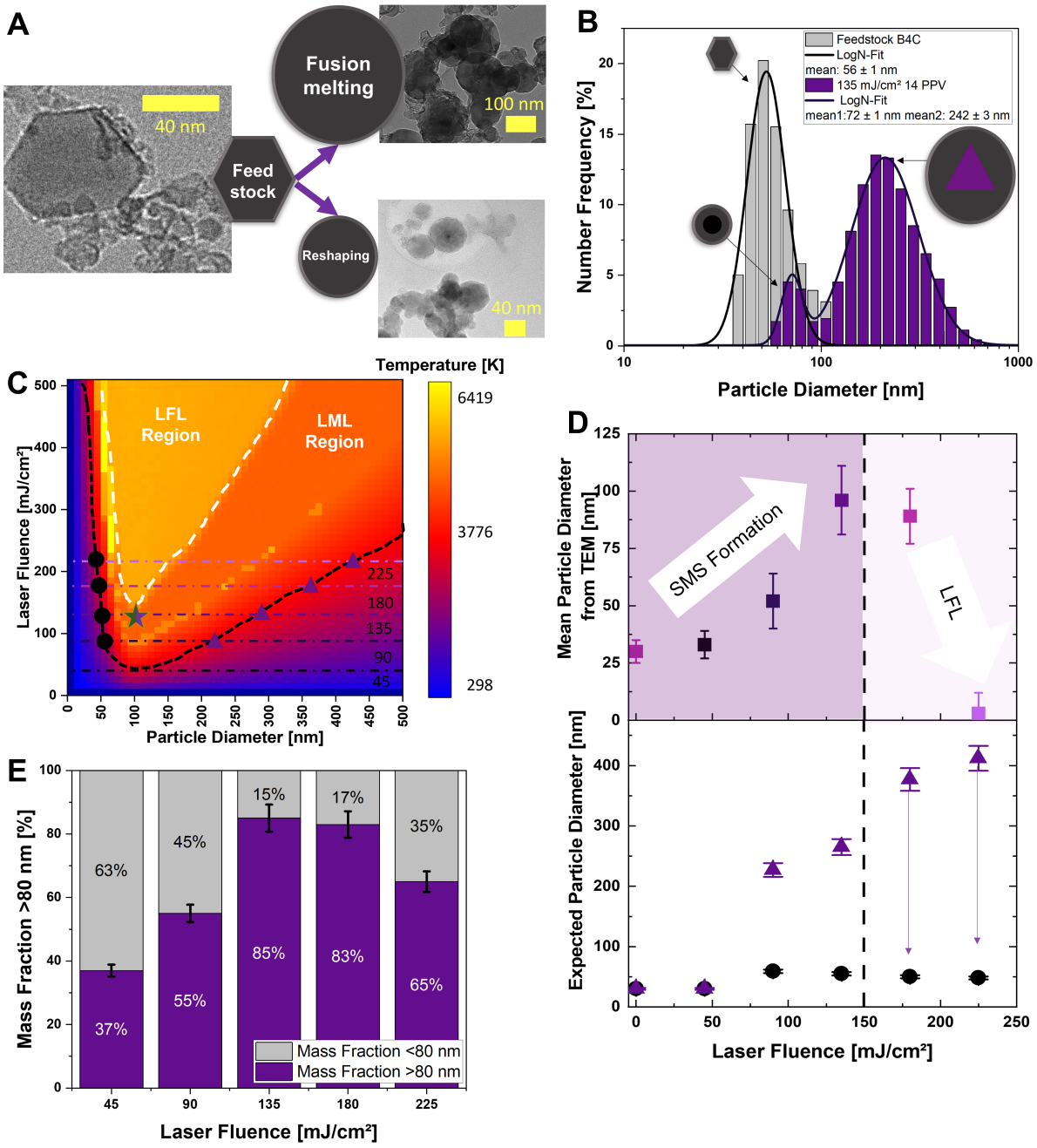

Figure 2: (A) Schematic representation of the LML concept, illustrating the transformation of irregular feedstock NPs into fusion-formed spherical SMSs and isochorically reshaped NPs, complemented by representative TEM micrographs of both feedstock particles and resulting SMSs. The corresponding number-weighted hydrodynamic size distributions determined by DLS (B) exemplify the evolution from the initial NPs to a bimodal distribution after LML at 135 mJ·cm^{-2} and 16 PPV with a graphic illustration of educt isochoric remelting (circle) and fusion melting (triangle). (C) Prediction of the LFL and LML regimes using the extended HME model, with a marked fluence series of 45, 90, 135, 180, and 225 mJ·cm^{-2}, with the modeled reshaping products indicated by black circles and the expected SMS diameters after fusion-melting indicated by purple triangle markers. The dashed black line marks the start of the LML region, whereas the dashed white line marks the start of the LFL region. The star denotes the observed mean particle size for both B_4CC and the B_4C reference (see Supporting Information File 1, Section S3). (D) Quantitative evaluation of TEM-derived (from Supporting Information File 1, Figure S6) equivalent diameters over the entire fluence series, in comparison to the modeled expected size. Arrows indicate the onset of fragmentation of larger particles. (E) Mass fraction of SMSs larger than 80 nm as a function of the laser fluence (with standard deviation from three independent measurements).

ing impurity-dependent thermophysical properties. Furthermore, impurities in the B_4CC starting material are predominantly attributed to free carbon. Under the applied thermal conditions in ethanol, carbon cannot undergo melting and thus does not form spherical particles, but instead remains as a solid non-melting phase. This behavior is further substantiated by XPS and XRD analyses (Supporting Information File 1, Section 2), which demonstrate a progressive decrease in oxide species alongside the persistent presence of unreacted graphitic carbon. Consequently, while the simulations capture the principal mechanisms governing the process, deviations from the experimental system are expected. The model should therefore be regarded as an approximation of the underlying physics rather than a precise predictive tool.

The laser-material-interactions described herein exclusively focuses on photothermal mechanisms, excluding stress confinement effects for two key reasons. First, the stress confinement conditions [53], relevant to ultrashort-pulsed laser fragmentation in liquids (e.g., picosecond-LFL) [54] are not applicable to the regime investigated here and are therefore omitted from further consideration. Second, given that (i) the optical penetration depth of the 343 nm laser in 30 nm boron carbide particles is approximately 32 nm, estimated from the relation $\delta = \lambda/(4\pi k)$, where k is the extinction coefficient at 343 nm [55], and (ii) the thermal penetration depth δ_{th} during the 18 ns pulse is approximately 0.5–1.0 µm ($\delta_{th} = (4\alpha\tau)^{0.5}$) [56], the feedstock particles experience homogeneous heating throughout their volume. Both values are originally defined for the penetration depth in bulk solids; nonetheless, the thermal penetration depth is substantially higher than the laser-excited particle diameter. For laser melting in liquids, the thermal penetration depth is the decisive parameter, and it exceeds the characteristic size of the feedstock NP diameter, including their agglomerates. Consequently, the entire agglomerate volume is thermally affected during a pulse, ensuring complete melting.

The bimodal size distribution characteristic of LML processes in the flat jet configuration was evaluated for a fluence series (45–225 mJ·cm^{-2}), with results analyzed primarily by DLS and TEM (see Supporting Information File 1, Section S4 and Figure S5). The size bimodality is confirmed by the DLS data in Figure 2B and the TEM images in Supporting Information File 1, Figure S6. A marked discrepancy between TEM and DLS outcomes is apparent, arising from the strong sixth-power dependence of DLS intensity on particle diameter, which may cause multiscattering phenomena and thereby overinterpret signals from larger particles. Moreover, DLS measures hydrodynamic sizes and thus registers particle aggregates as singular large entities, whereas TEM resolves primary NPs distinctly [57]. Consequently, DLS cannot distinguish individual spheres from aggregates, precluding clear differentiation of samples where larger aggregates and spheres coexist. These methodological differences account for the absence of distinct double peaks in the TEM analysis of Supporting Information File 1, Figure S6B–E, in contrast to the pronounced bimodality in the DLS spectrum of Figure 2B. Even though absolute particle diameters deviate between TEM and DLS, the collective evidence robustly validates the model's predictive power for bimodal size distributions recorded by both methods.

The model for LML predicts a progressive increase in particle size beyond the laser melting limit, with final diameters of 225 to 375 nm occurring simultaneously with an initial isochoric reshaping process with mean diameters near 50 nm in our case (Figure 2C). These predictions assume thermal equilibrium conditions prevalent in batch reactors, where repeated laser pulses drive cumulative growth, aggregation, and particle fusion, with the fluence dictating the maximum achievable size through complete melting. This assumes the availability of particles in the vicinity of the host particle to grow and a sufficiently fast particle motion (or a sufficient collision rate). In continuous-flow flat jet reactors, however, particle motion deviates markedly from these conditions owing to kinetic limitations, such as lower agglomeration rates. This yields a persistent size fraction with mean diameters below 100 nm (Figure 2D, top), in direct contrast to purely thermodynamic expectations (Figure 2D, bottom). Interestingly, particle growth and the final diameters remain fluence-dependent. Both mean particle diameter and mass fraction of particles exceeding 80 nm (Figure 2E) increase as the fluence rises from 45 to 135 mJ·cm^{-2}, resulting in 85 ± 5% of larger particles at 135 mJ·cm^{-2}. For mass yield determination, we selected TEM images, as DLS cannot differentiate spheres from aggregates of equivalent or larger sizes. Particles in pressurized flow systems undergo rapid convective transport out of the LML zone. Hence, agglomeration kinetics are limited by the residence time of the individual particles in the irradiated volume of the unidirectional convective flow of the liquid jet ($\tau = h/v$), which is approximately 1.5 µs, assuming a laser spot height of h = 8 mm and a linear flow velocity of v = 4.8 m·s^{-1}. Hence, fluence in LML is not only a thermodynamic ruler of maximum particle size but also accelerates particle formation kinetics by intensified heating and enhanced mass transport. Photophoretic forces, stemming from asymmetric laser-induced heating, propel particles from hotspots, reducing collision frequencies essential for fusion and aggregation; positive photophoresis predominates, countering thermophoretic clustering [58,59]. Convection-driven dilution further suppresses particle clustering and high local concentration, enforcing non-equilibrium dynamics that curtail excessive growth. Furthermore, studies by Tsuji et al. [60] have shown that incubation effects in laser ablation pro-

cesses can cause nanoparticle agglomeration. This occurs on timescales of seconds to minutes after the incubation period, especially when stabilizing ligands are present, which is substantially longer than the timescales realized under continuous flat jet conditions.

Pulse per volume study

Another hypothesis as to why the B_4CC SMSs have substantially smaller particle diameters than anticipated by the model may be due to the interpulse delay (τ_{IP}) and the number of PPV, which are both substantially smaller than those in literature-established batch setups [24]. Hence, we systematically varied the PPV from 1 to 16 and, alongside reducing τ_{IP} from 1.4 to 0.1 ms at a fluence of 135 mJ·cm^{-2}, monitored differences in the particle size distributions. The fluence of 135 mJ·cm^{-2} was chosen as it yields the largest particle diameter, while it is still clearly below the fragmentation threshold. The results are shown in Figure 3.

The particle size distribution data from DLS of the PPV studies (Figure 3A) are qualitatively consistent with the TEM observations in Figure 3D and Supporting Information File 1, Figure S9, except for the previously discussed shift in absolute particle diameters. The peak around 50 nm particle size, probably derived from isochoric reshaping, is independent of PPV and τ_{IP}. Based on these findings, we can hypothesize that, in this regime, reshaping occurs as a single-pulse event decoupled from particle agglomeration or fusion. Regarding the peaks of the larger particle size fractions, attributed to the pathway of aggregation–melting–fusion, particle size increases with PPV up to a maximum at 4 PPV. This is consistent with previously described mechanisms involving NP heating, melting, and coalescence during laser irradiation by Ishikawa and coworkers [29]. Interestingly, contrary to expectations from the LML's HME model, beyond 4 PPV, the size increase stagnates, a phenomenon that might be attributed to several hypotheses, which are the mechanistic discoveries of the continuous flat jet LML: (i) Heat: Absorption coefficients of NPs are particle size-dependent and increase with particle diameter. Hence, profound heat accumulation could preferably occur in particles, initiating LFL when a specific particle size threshold is exceeded. However, this is unsupported by our experimental findings as no small fragments were detected by DLS or TEM at the used laser fluence and PPV (see Figure 2E). (ii) Bubbles: With increasing PPV, τ_{IP} decreases. Hence, we may have reached a threshold value of τ_{IP} where cavitation bubbles generated during melting impair the attachment of educt particles to molten aggregates and limit further particle growth. Consequently, the number of aggregation–melting–fusion steps would be capped. Note that there are indications of gas and bubble formation during LML [61,62], but little is yet known about the size and lifetime of these bubbles [24]. (iii) Sluggish aggregation: There is a minimal PPV threshold for growth initiation, affirmed by the observed stagnant size for more than 4 PPV. It is known that the aggregation rate of colloidal NPs scales with the square of the number concentration [63]. Hence, it is conceivable that additional pulses cannot contribute to further growth when the particle number concentration is too low and, thereby, the aggregation kinetics are too slow. This disables the initiation of subsequent aggregation–melting–fusion steps, resulting in a defined final particle diameter.

While direct kinetic rate constants were not experimentally measured, the observed size plateau beyond 4 PPV (0.4 ms interpulse delay) and the resulting mean particle diameters below the theoretically predicted size maximum strongly indicate a kinetic limitation (kinetic control) rather than a thermodynamic growth limit. To substantiate the sluggish aggregation hypothesis, we calculated the Brownian motion of particles during the pulse repetition interval, which governs the likelihood of particles encountering fusion partners. This was approximated by the Stokes–Einstein equation ($D = k_B T/(6\pi\eta r)$ at 20 °C, using the viscosity of ethanol and a particle size of 50 nm [64,65] (Figure 3C). A Poisson distribution model shows a sharp decline in aggregation probability beyond 4 PPV with the probability falling to under 5%, which effectively caps particle fusion. These results should only be used to gain an understanding of the behavior and should not be interpreted as absolute numbers. This may explain the plateau in particle size despite increasing pulse numbers (size histograms are displayed in Section S5 of Supporting Information File 1). Thus, both PPV, which imposes a minimum of four pulses before the saturation of particle size occurs due to a concentration limit, and τ_{IP}, restricting diffusive repositioning between successive pulses, could evenly contribute to particle growth capping. This dual dependency of the final particle diameter on τ_{IP} and the suspension properties, like interparticle distance scaling with concentration, offers further degrees of freedom for upscaling continuous-flow LML. Furthermore, the following interdependencies need to be considered during LML. First, LML mass throughput scales with the concentration, accelerating aggregation and increasing the fusion probability required to form the larger SMSs, indicating a size–concentration correlation. Second, laser systems with even higher repetition rates would be difficult to implement as they must be matched by higher flow speeds to reach higher (i.e., above 4) PPV values, in turn providing lower τ_{IP}.

In future studies, this parameter matching could be mechanistically elucidated by altering τ_{IP} at a constant PPV by changing the residence time in the LML zone (e.g., by doubling flow speed and repetition rate). Also, testing different feedstock par-

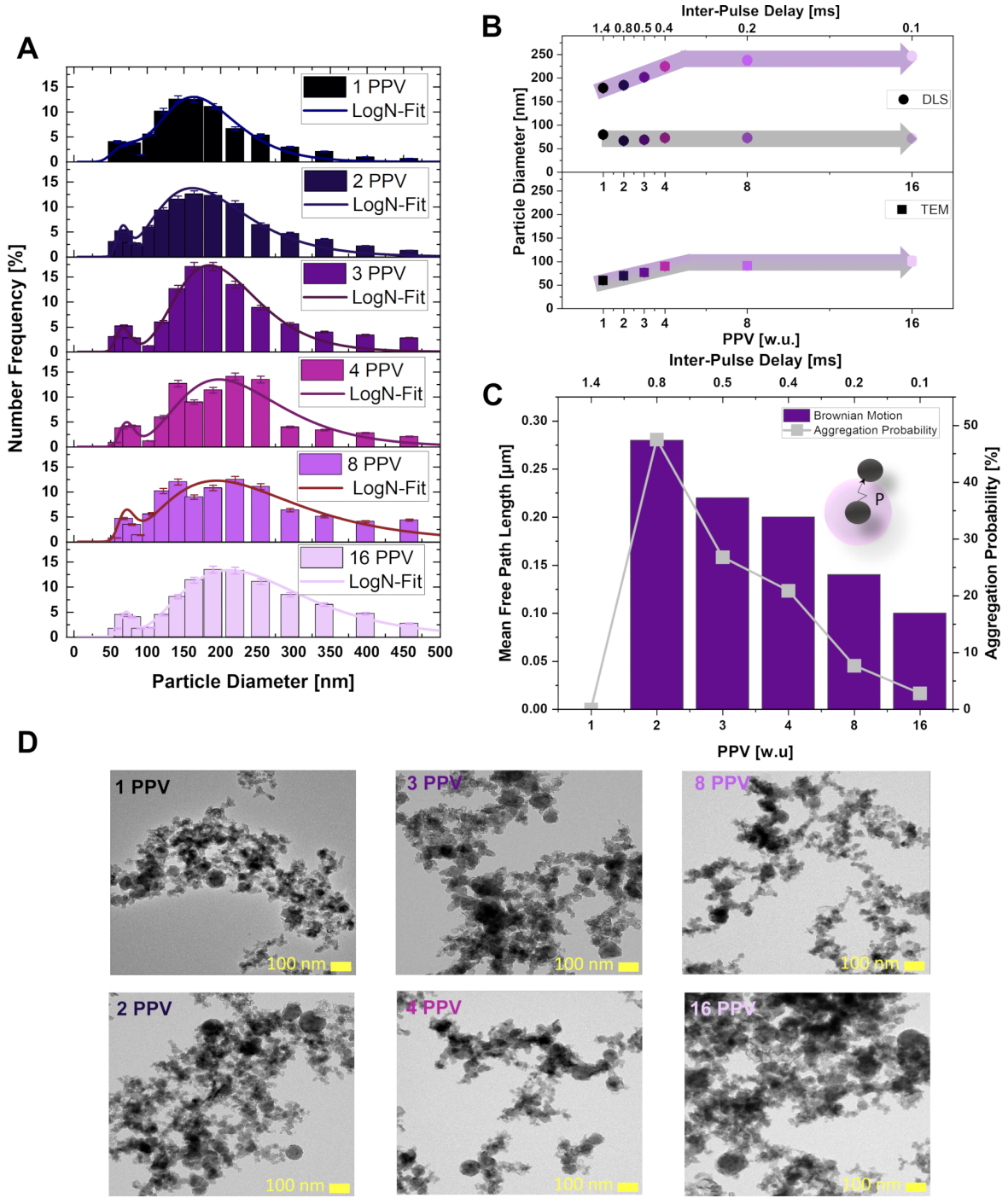

Figure 3: (A) DLS size distributions for NPs exposed to PPV of 1–16 at 135 mJ·cm^{-2}, with each distribution fitted using a log-normal function to resolve distinct size populations evolving with pulse number. (B) Quantitative evaluation of the bimodal particle size evolution as a function of PPV and interpulse delay that regulates particle fusion dynamics. (C) Calculation of the Brownian motion-driven diffusion lengths of the precursor particles during the interpulse delay linked to PPV, combined with the corresponding Poisson probability of particle collisions enabling fusion events. (D) Representative TEM images across the PPV series.

ticle concentrations would be straightforward, at least up to a threshold where the fluence drop along the beam path through the jet thickness is insignificant. Another playground for tuning the aggregation rate includes altering the liquid properties, the viscosity, and the Debye length. The Debye length scales with the square root of the medium's permittivity, and a shorter Debye length would destabilize the suspension, accelerate agglomeration, and potentially improve SMS formation.

But the aggregation-limiting factor can also be considered useful from an application perspective. A major advantage of flat jet SMS synthesis, experimentally evidenced in this study, is that the product particle size is constant above a certain PPV value, rendering the flow-through LML process robust against flow rate fluctuations. Furthermore, while the thermodynamic optimum is always achieved in the batch process at extended processing time, it can be specifically influenced kinetically in the continuous flow process, making the process even more versatile for isolating intermediates [66]. After having identified the intended "arrest" size, only the number of pulses required to synthesize a specific particle type needs to be "invested", without wasting energy by unnecessarily applying laser pulses. Furthermore, it should be noted that B_4C SMS formation is also possible with highly chemically contaminated particles, omitting the need for expensive, highly pure feedstock particles, although the impact of the impurities on the mechanical properties of the SMSs needs to be evaluated in future studies.

As a competing mechanism to LML, LFL occurs at a higher fluence in Figure 2E; this is indicated by a distinct cutoff in the expected particle growth at a laser fluence exceeding 150 mJ·cm^{-2}. For particles around 100 nm, as observed in Figure 2C, this fluence provides sufficient energy to exceed the threshold fluence for LFL. Consequently, the process yields reshaped spheres of approximately 50 nm, representing one facet of the thermodynamic optimum, while particles exceeding ≈100 nm may undergo fragmentation via mechanisms such as phase explosion upon subsequent pulses, producing ultrasmall B_4CC NPs (≈2 nm; Supporting Information File 1, Figure S7 and Section S3) [46,67,68]. These ultrasmall particles correspond to recent findings by Ziefuß et al. [38] using identical wavelength and pulse duration (but higher fluences). This contrasts with reports by Koshizaki et al. on nanosecond-pulsed laser-induced LML of boron [24] and boron carbide [26,69,70]. The apparent discrepancies between the two experimental observations can be rationalized by fluence gradients inherent to the respective setups. These gradients arise from spatial intensity distributions within individual laser pulses, the optical penetration depth of the laser in colloidal suspensions, and from partial shielding by larger particles. While Figure 2C assumes a uniform fluence distribution, both spatial and temporal inhomogeneities of the laser field are unavoidable. In flat liquid jet configurations, optical path and irradiated volume are well defined, resulting in a narrow fluence window and a sharply resolved transition between LML and LFL. By contrast, batch reactors exhibit a pronounced fluence drop across the optical path due to absorption and scattering, which superimposes both processes and obscures this transition. Moreover, previous studies primarily analyzed the sediment fraction, which predominantly contains larger and more compact particles, while smaller NPs were not systematically evaluated.

Conclusion

The controlled synthesis of hard-ceramic nanoparticles (NPs) and sub-micrometer spheres (SMSs) remains a key challenge in materials science as it requires precise control over particle size, crystallinity, and sphericity to tailor functional performance. Achieving this balance demands a mechanistic understanding of how aggregation, melting, and fusion kinetics jointly determine size selectivity and yield. Laser melting in liquids (LML) provides a direct and chemically clean route to reorganize NPs through spatially and temporally confined energy input. In accordance with the principles of green chemistry, LML enables solvent-based, reagent-free synthesis, offering a sustainable platform for the controlled fabrication of SMSs. However, scalability limitations inherent to conventional batch-mode LML hinder its translation to industrial production. Bridging this gap requires the development of a continuous LML technique that preserves precise control over the interaction between laser and matter. This study implements the LML concept in a flat jet reactor, enabling a systematic and decoupled evaluation of the effects of laser parameters on SMSs formation. Boron carbide was chosen as the model material not only because of its high application relevance, but also due to its high melting point (difficult to process by other methods) and chemical inertness (robust in LML), making it an ideal benchmark for extending LML towards continuous operation.

Transmission electron microscopy and dynamic light scattering analyses reveal a bimodal product distribution. These two size fractions comprise a fluence-independent population centered at ≈50 nm, attributed to particle reshaping, and an aggregation–fusion-driven fraction spanning 100–225 nm. However, in the flat jet configuration, this growth remains kinetically constrained as the thermodynamically predicted particle sizes of 225–375 nm do not form. Hence, flow-through LML may continuously produce size intermediates that have been inaccessible in prolonged batch reactor LML processing. Furthermore, XRD and XPS characterizations in combination demonstrate the effective elimination of oxide impurities, thus validating the LML synthesis method.

The flat jet experiments further underscore the necessity of incorporating fragmentation fluence thresholds into theoretical models. At fluences exceeding 150 mJ·cm^{-2}, fragmentation of larger spheres in the flat jet system generates ultrasmall NPs, underlining the advantage of flat jet LML in precise fluence control within the excited volume (no beam refraction, minimized beam attenuation along the thin liquid layer). To elucidate the formation dynamics and the apparent deviation from

thermodynamic growth, variations in pulse per volume (PPV, up to 16) indicate that fusion-mediated size increase requires at least four pulses. This constraint probably arises from limited Brownian diffusion and low collision rates (≈5%). This goes along with the use of a high-repetition-rate laser system (required for decent throughput), where the short pulse intervals restrict the number of interparticle collision events and thus growth based on an aggregation–melting–fusion mechanism. These effects yield a persistent 50 nm population and a fluence-dependent secondary modal size fraction exceeding 80 nm with a mass yield of ≈85% at 135 mJ·cm^{-2}. This decouples the LML process from thermodynamic equilibrium conditions and further allows for control of particle size distributions by interpulse delay time and particle mass concentration, yielding particles of ≈100 nm, notoriously difficult to synthesize with laser-based synthesis routes.

Productivity Estimation

A comparative analysis of the productivity of established synthesis methods for SMSs by LML allows us to classify and rank the scaling potential of the flat jet approach as specified in Figure 4. The calculations supporting these values are provided in Supporting Information File 1, Section S6. An automated, exchangeable batch reactor serves as the baseline for comparison and achieves a productivity of 5.15 mg·h^{-1} [32]. The optimized guided flow reactor achieves 195 mg·h^{-1} [29], underscoring the significant potential of flow-based reactors during scalable synthesis. However, the reactor's design constraints inherently limit this performance, suggesting that the system has likely reached its maximum productivity. The current flat jet reactor yields 100 mg·h^{-1}. However, by fully exploiting advanced laser parameters, particularly the power (here 400 W) and repetition rate (10 kHz) of high-power nanosecond laser systems, productivity approaching 900 mg·h^{-1} can be rapidly attained, while future beam shaping strategies may further enhance process control and selectivity [71]. Extrapolating from studies on heating, a fourfold increase in feedstock particle concentration is feasible, enabling substantially enhanced outputs. This significant productivity enhancement establishes the industrial relevance of the flat jet flow reactor, particularly for SMS synthesis. This method enables scalable production with precisely tunable particle characteristics and opens new pathways for materials preparation in research-intensive and application-driven fields. Employing the "unused" laser energy that exits the flat jet would maximize the usage of the available laser power. This could be done, for example, by stacking LML jets or increasing the jet thickness along the trade-off between energy usage (energy-specific LML mass throughput) and fluence deviation-caused SMS size precision loss (decreasing product quality). The flat jet technique's capacity for rapid throughput and flexible process control positions it as a transformative advancement for both fundamental research and upscaled material production.

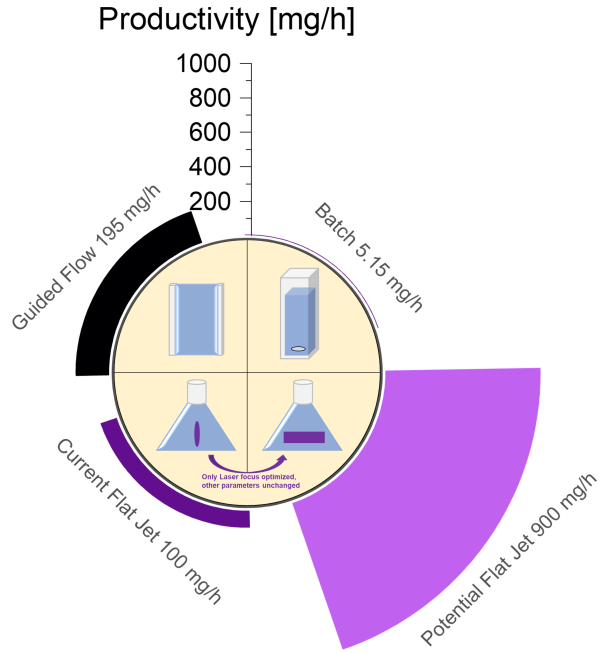

Figure 4: Productivity metrics of common pulsed laser melting in liquid synthesis routes for sub-micrometer spheres, showing production rates scaling with synthesis innovations.

Supporting Information

Supporting Information File 1

Additional experimental data.
[https://www.beilstein-journals.org/bjnano/content/supplementary/2190-4286-17-108-S1.pdf]

Acknowledgements

We would like to thank Julian Fink, Tobias Bessel, Florian de Kock, Kirsten Schwark, and Jurij Jakobi for their support. The development of the flat jet system and the characterization of the particles would not have been possible without their dedicated contribution. Artificial intelligence was used as an aid in the linguistic revision of the manuscript. All experimental work and the underlying scientific content were carried out independently by the author and were not influenced by artificial intelligence. A part of this work was conducted at the Laboratory of XPS Analysis, Joint-use Facilities, Hokkaido University.

Funding

We gratefully acknowledge financial support from GF-GG under project no.: 491146928 (DFG-GEPRIS). We also grate-

fully acknowledge the DFG Deutsche Forschungsgemeinschaft for its financial support under project number 555656461. The XPS part was supported by “Advanced Research Infrastructure for Materials and Nanotechnology in Japan (ARIM)” of the Ministry of Education, Culture, Sports, Science and Technology (MEXT), proposal number JPMXP1226HK0007.

ORCID® iDs

Nico G. Koch - https://orcid.org/0009-0002-7247-8321
Christoph Rehbock - https://orcid.org/0000-0002-4708-5246
Naoto Koshizaki - https://orcid.org/0000-0003-4491-7200
Stephan Barcikowski - https://orcid.org/0000-0002-9739-7272

Data Availability Statement

Data generated and analyzed during this study is available from the corresponding author upon reasonable request.

Preprint

A non-peer-reviewed version of this article has been previously published as a preprint: https://doi.org/10.26434/chemrxiv-2025-w0g82

References

1. Lei, J.; Xiaofan, W. *J. Ceram. Process. Res.* **2024,** *25,* 904–909. doi:10.36410/jcpr.2024.25.5.904
2. Yan, Z.; Gao, Y.; Zhang, H. *Appl. Sci.* **2023,** *13,* 10957. doi:10.3390/app131910957
3. Bafakeeh, O. T.; Shewakh, W. M.; Abu-Oqail, A.; Abd-Elaziem, W.; Abdel Ghafaar, M.; Abu-Okail, M. *Polymers (Basel, Switz.)* **2021,** *13,* 4116. doi:10.3390/polym13234116
4. Singhal, V.; Shelly, D.; Saxena, A.; Gupta, R.; Verma, V. K.; Jain, A. *Lubricants* **2025,** *13,* 93. doi:10.3390/lubricants13020093
5. Çöpoğlu, N.; Çiçek, B. *Surf. Coat. Technol.* **2021,** *419,* 127275. doi:10.1016/j.surfcoat.2021.127275
6. Wang, W.; Chen, Y.; Chen, A.; Ma, X. *Mater. Chem. Phys.* **2020,** *240,* 122279. doi:10.1016/j.matchemphys.2019.122279
7. Shipway, P. H.; Hogg, J. J. *Wear* **2007,** *263,* 887–895. doi:10.1016/j.wear.2006.11.028
8. Tatami, J.; Kodama, E.; Watanabe, H.; Nakano, H.; Wakihara, T.; Komeya, K.; Meguro, T.; Azushima, A. *J. Ceram. Soc. Jpn.* **2008,** *116,* 749–754. doi:10.2109/jcersj2.116.749
9. Okada, M.; Yoshimoto, F.; Watanabe, H.; Nikawa, M. *J. Manuf. Processes* **2023,** *89,* 410–429. doi:10.1016/j.jmapro.2023.01.055
10. Yu, Z.; Zheng, Y.; Sun, J.; Zhao, J. *Int. J. Refract. Met. Hard Mater.* **2026,** *134,* 107436. doi:10.1016/j.ijrmhm.2025.107436
11. Du, C.; Yu, T.; Sui, X.; Zhang, Z.; Cai, R.; Zhang, L.; Feng, Y.; Feng, M.; Zhou, F.; Wang, D. *Adv. Mater. (Weinheim, Ger.)* **2025,** *37,* 2413781. doi:10.1002/adma.202413781
12. Xing, Y.; Deng, J.; Wang, X.; Meng, R. *Wear* **2015,** *342–343,* 1–12. doi:10.1016/j.wear.2015.08.002
13. Jendrzej, S.; Gondecki, L.; Debus, J.; Moldenhauer, H.; Tenberge, P.; Barcikowski, S.; Gökce, B. *Appl. Surf. Sci.* **2019,** *467–468,* 811–818. doi:10.1016/j.apsusc.2018.10.060
14. Kambale, K. R.; Mahajan, A.; Butee, S. P. *Met. Powder Rep.* **2019,** *74,* 130–136. doi:10.1016/j.mprp.2019.04.060
15. Palmero, P. *Nanomaterials* **2015,** *5,* 656–696. doi:10.3390/nano5020656
16. Domnich, V.; Reynaud, S.; Haber, R. A.; Chhowalla, M. *J. Am. Ceram. Soc.* **2011,** *94,* 3605–3628. doi:10.1111/j.1551-2916.2011.04865.x
17. Mohammad Sharifi, E.; Karimzadeh, F.; Enayati, M. H. *Adv. Powder Technol.* **2011,** *22,* 354–358. doi:10.1016/j.apt.2010.05.002
18. Kozień, D.; Żeliszewska, P.; Szermer-Olearnik, B.; Adamczyk, Z.; Wróblewska, A.; Szczygieł, A.; Węgierek-Ciura, K.; Mierzejewska, J.; Pajtasz-Piasecka, E.; Tokarski, T.; Cios, G.; Cudziło, S.; Pędzich, Z. *Materials* **2023,** *16,* 6534. doi:10.3390/ma16196534
19. Sezer, A. O.; Brand, J. I. *Mater. Sci. Eng., B* **2001,** *79,* 191–202. doi:10.1016/s0921-5107(00)00538-9
20. Jafari, A.; Mosavat, M.; Meidanchi, A.; Hossienkhani, H. *J. Chem. Res.* **2018,** *42,* 73–76. doi:10.3184/174751918x15178264975471
21. Xu, S.; Yu, Y.; Zhang, B.; Zhu, K.; Cheng, Y.; Zhang, T. *RSC Adv.* **2025,** *15,* 10717–10730. doi:10.1039/d5ra00734h
22. Chioatto, E.; Mancinelli, S.; Mazzanti, M.; Onofrio, F. *Curr. Opin. Green Sustainable Chem.* **2024,** *50,* 100976. doi:10.1016/j.cogsc.2024.100976
23. Venkatesan, K.; Sundarababu, J.; Anandan, S. S. *Green Chem. Lett. Rev.* **2024,** *17,* 2312848. doi:10.1080/17518253.2024.2312848
24. Ishikawa, Y.; Tsuji, T.; Sakaki, S.; Koshizaki, N. *Prog. Mater. Sci.* **2023,** *131,* 101004. doi:10.1016/j.pmatsci.2022.101004
25. Ziefuß, A. R.; Tibbetts, K. M.; Barcikowski, S., Eds. *Handbook of Green Laser Synthesis & Processing of Colloids,* 3rd ed.; University of Duisburg-Essen: Duisburg Essen, Germany, 2025. doi:10.17185/duepublico/84588
26. Ishikawa, Y.; Shimizu, Y.; Sasaki, T.; Koshizaki, N. *Appl. Phys. Lett.* **2007,** *91,* 161110. doi:10.1063/1.2799786
27. Suehara, K.; Takai, R.; Ishikawa, Y.; Koshizaki, N.; Omura, K.; Nagata, H.; Yamauchi, Y. *ChemPhysChem* **2021,** *22,* 675–683. doi:10.1002/cphc.202001000
28. Ishikawa, Y.; Sasaki, T.; Koshizaki, N. *J. Nanosci. Nanotechnol.* **2010,** *10,* 5467–5470. doi:10.1166/jnn.2010.1947
29. Ishikawa, Y.; Koshizaki, N. *Sci. Rep.* **2018,** *8,* 14208. doi:10.1038/s41598-018-32528-6
30. Nakamura, D.; Koshizaki, N.; Shishido, N.; Kamiya, S.; Ishikawa, Y. *Nanomaterials* **2021,** *11,* 2201. doi:10.3390/nano11092201
31. Koshizaki, N.; Ishikawa, Y. Formation Mechanism of Spherical Submicrometer Particles by Pulsed Laser Melting in Liquid. In *High-Energy Chemistry and Processing in Liquids;* Ishikawa, Y.; Nakamura, T.; Saeki, M.; Sato, T.; Sugiyama, T.; Wada, H.; Yatsuhashi, T., Eds.; Springer Nature: Singapore, 2022; pp 115–135. doi:10.1007/978-981-16-7798-4_7
32. Takai, R.; Koshizaki, N.; Ishikawa, Y.; Hakuta, Y. *Chem. Eng. Sci.* **2020,** *219,* 115580. doi:10.1016/j.ces.2020.115580
33. Friedenauer, T.; Buck, K.; Eberwein, M.; Bünte, A.-L.; Rehbock, C.; Barcikowski, S. *Part. Part. Syst. Charact.* **2023,** *40,* 2300034. doi:10.1002/ppsc.202300034
34. Tack, M.; Usama, M.; Kazamer, N.; Exner, K. S.; Brodmann, M.; Barcikowski, S.; Reichenberger, S. *ACS Appl. Energy Mater.* **2024,** *7,* 4057–4067. doi:10.1021/acsaem.4c00342
35. Friedenauer, T.; Spellauge, M.; Sommereyns, A.; Rehbock, C.; Huber, H. P.; Barcikowski, S. *J. Phys. Chem. C* **2025,** *129,* 6803–6816. doi:10.1021/acs.jpcc.4c08643
36. Zerebecki, S.; Reichenberger, S.; Barcikowski, S. *J. Phys. Chem. A* **2020,** *124,* 11125–11132. doi:10.1021/acs.jpca.0c08787

37. Koch, N. G.; Poschmann, M.; Heumann, S.; Puthussery, A. J.; Čolić, V.; Barcikowski, S.; Reichenberger, S. *ChemCatChem* **2025,** *17,* e00622. doi:10.1002/cctc.202500622
38. Ziefuß, A. R.; Stratmann, N.; Reifenrath, C.; Kanu, G.; Berndt, N.; Disch, S.; Barcikowski, S. *Opt. Lett.* **2026,** *51,* 437–440. doi:10.1364/ol.582519
39. Saeki, M.; Taguchi, T.; Nakashima, N.; Ohba, H. *J. Photochem. Photobiol., A* **2015,** *299,* 189–193. doi:10.1016/j.jphotochem.2014.11.022
40. Sakaki, S.; Ikenoue, H.; Tsuji, T.; Ishikawa, Y.; Koshizaki, N. *Appl. Surf. Sci.* **2018,** *435,* 529–534. doi:10.1016/j.apsusc.2017.10.235
41. Swihart, M. T.; Carr, R. W. *Int. J. Chem. Kinet.* **1996,** *28,* 817–828. doi:10.1002/(sici)1097-4601(1996)28:11<817::aid-kin4>3.0.co;2-q
42. Khairani, I. Y.; Mínguez-Vega, G.; Doñate-Buendía, C.; Gökce, B. *Phys. Chem. Chem. Phys.* **2023,** *25,* 19380–19408. doi:10.1039/d3cp01214j
43. Ishikawa, Y.; Katou, Y.; Koshizaki, N.; Feng, Q. *Chem. Lett.* **2013,** *42,* 530–531. doi:10.1246/cl.130044
44. Huang, H.; Zhigilei, L. V. *Sci. China: Phys., Mech. Astron.* **2022,** *65,* 274206. doi:10.1007/s11433-021-1881-8
45. Huang, H.; Zhigilei, L. V. *J. Phys. Chem. C* **2021,** *125,* 13413–13432. doi:10.1021/acs.jpcc.1c03146
46. Plech, A.; Tack, M.; Huang, H.; Arefev, M.; Ziefuß, A. R.; Levantino, M.; Karadas, H.; Chen, C.; Zhigilei, L. V.; Reichenberger, S. *ACS Nano* **2024,** *18,* 10527–10541. doi:10.1021/acsnano.3c12314
47. Boron Carbide (B4C) Nanopowder/Nanoparticles. https://shop.nanografi.com/nanoparticles/boron-carbide-b4c-nanopowder-nanoparticles-purity-99-5-size-40-60-nm-hexagonal/ (accessed Nov 17, 2025).
48. UP200St - Leistungsstarker Ultraschall-Labor-Homogenisator. https://www.hielscher.com/de/up200st-powerful-ultrasonic-lab-homogenizer.htm (accessed Oct 7, 2026).
49. Sheindlin, M.; Vervikishko, P.; Bgasheva, T.; Bulava, A.; Frolov, A.; Vasin, A. *Phys. Rev. B* **2025,** *111,* 214105. doi:10.1103/physrevb.111.214105
50. Pyatenko, A.; Wang, H.; Koshizaki, N.; Tsuji, T. *Laser Photonics Rev.* **2013,** *7,* 596–604. doi:10.1002/lpor.201300013
51. Sakaki, S.; Ikenoue, H.; Tsuji, T.; Ishikawa, Y.; Koshizaki, N. *ChemPhysChem* **2017,** *18,* 1101–1107. doi:10.1002/cphc.201601175
52. Arefev, M. I.; Valavanis, A. S.; Zhigilei, L. V. *J. Phys. Chem. C* **2026,** *130,* 1042–1066. doi:10.1021/acs.jpcc.5c06989
53. Paltauf, G.; Dyer, P. E. *Chem. Rev.* **2003,** *103,* 487–518. doi:10.1021/cr010436c
54. Spellauge, M.; Tack, M.; Streubel, R.; Miertz, M.; Exner, K. S.; Reichenberger, S.; Barcikowski, S.; Huber, H. P.; Ziefuß, A. R. *Small* **2023,** *19,* 2206485. doi:10.1002/smll.202206485
55. Larruquert, J. I.; Pérez-Marín, A. P.; García-Cortés, S.; Rodríguez-de Marcos, L.; Aznárez, J. A.; Méndez, J. A. *J. Opt. Soc. Am. A* **2012,** *29,* 117. doi:10.1364/josaa.29.000117
56. Arita, Y.; Nishi, Y.; Amaya, M.; Matsui, T. *Thermochim. Acta* **2000,** *352–353,* 39–42. doi:10.1016/s0040-6031(99)00434-7
57. Letzel, A.; Gökce, B.; Menzel, A.; Plech, A.; Barcikowski, S. *Appl. Surf. Sci.* **2018,** *435,* 743–751. doi:10.1016/j.apsusc.2017.11.130
58. Li, S.; Marshall, J. S.; Liu, G.; Yao, Q. *Prog. Energy Combust. Sci.* **2011,** *37,* 633–668. doi:10.1016/j.pecs.2011.02.001
59. Lin, C.-H.; Zhu, C. Chapter 3 - Relevance of Particle Transport in Surface Deposition and Cleaning. In *Developments in Surface Contamination and Cleaning,* 2nd ed.; Kohli, R.; Mittal, K. L., Eds.; William Andrew Publishing, 2008; Vol. 1, pp 91–118. doi:10.1016/b978-0-323-29960-2.00003-4
60. Tsuji, T.; Takade, I.; Tsuji, M.; Ishimawa, Y.; Koshizaki, N. *J. Laser Micro/Nanoeng.* **2015,** *10,* 329–333. doi:10.2961/jlmn.2015.03.0017
61. Tabayashi, Y.; Sakaki, S.; Koshizaki, N.; Yamauchi, Y.; Ishikawa, Y. *Langmuir* **2021,** *37,* 7167–7175. doi:10.1021/acs.langmuir.1c00736
62. Pustovalov, V. K. *Appl. Phys. A: Mater. Sci. Process.* **2020,** *126,* 196. doi:10.1007/s00339-020-3370-6
63. Bukosky, S. C.; Dev, S.; Allen, M. S.; Allen, J. W. *Beilstein J. Nanotechnol.* **2021,** *12,* 413–423. doi:10.3762/bjnano.12.33
64. Zhou, Y.; Huang, M.; Tian, F.; Shi, X.; Zhang, X. *J. Chem. Phys.* **2024,** *160,* 054109. doi:10.1063/5.0189490
65. Zhong, H.; Lin, Z. *Opt. Express* **2025,** *33,* 30073–30087. doi:10.1364/oe.567763
66. Lau, M.; Ziefuß, A.; Komossa, T.; Barcikowski, S. *Phys. Chem. Chem. Phys.* **2015,** *17,* 29311–29318. doi:10.1039/c5cp04296h
67. Pustovalov, V. K. *Nanotechnol. Precis. Eng.* **2024,** *8,* 025001. doi:10.1063/10.0034539
68. Havelka, O.; Cvek, M.; Urbánek, M.; Łukowiec, D.; Jašíková, D.; Kotek, M.; Černík, M.; Amendola, V.; Torres-Mendieta, R. *Nanomaterials* **2021,** *11,* 1538. doi:10.3390/nano11061538
69. Kondo, M.; Shishido, N.; Kamiya, S.; Kubo, A.; Umeno, Y.; Ishikawa, Y.; Koshizaki, N. *Part. Part. Syst. Charact.* **2018,** *35,* 1800061. doi:10.1002/ppsc.201800061
70. Ishikawa, Y.; Feng, Q.; Koshizaki, N. *Appl. Phys. A: Mater. Sci. Process.* **2010,** *99,* 797–803. doi:10.1007/s00339-010-5745-6
71. Molina-Prados, S.; Bulgakova, N. M.; Bulgakov, A. V.; Lancis, J.; Mínguez-Vega, G.; Doñate-Buendía, C. *Beilstein J. Nanotechnol.* **2026,** *17,* 309–342. doi:10.3762/bjnano.17.22

License and Terms

This is an open access article licensed under the terms of the Beilstein-Institut Open Access License Agreement (https://www.beilstein-journals.org/bjnano/terms), which is identical to the Creative Commons Attribution 4.0 International License (https://creativecommons.org/licenses/by/4.0). The reuse of material under this license requires that the author(s), source and license are credited. Third-party material in this article could be subject to other licenses (typically indicated in the credit line), and in this case, users are required to obtain permission from the license holder to reuse the material.

The definitive version of this article is the electronic one which can be found at: https://doi.org/10.3762/bjnano.17.108

BEILSTEIN JOURNAL OF NANOTECHNOLOGY

Exploring combinations of spatial laser beam shaping for advancing nanoparticle synthesis by ablation in liquids

Rémi Bérard*[1], Abdel Rahman Altakroury[2], Oleksandr Gatsa[1], Zongwen Fu[2], Bilal Gökce[2] and Alexander V. Bulgakov*[1]

Full Research Paper

Open Access

Address:
[1]FZU - Institute of Physics of the Czech Academy of Sciences, Na Slovance 1999/2, 18200 Prague 8, Czech Republic and [2]Chair of Materials Science and Additive Manufacturing, School of Mechanical Engineering and Safety Engineering, University of Wuppertal, 42119 Wuppertal, Germany

Email:
Rémi Bérard* - remi.berard@fzu.cz;
Alexander V. Bulgakov* - alexander.bulgakov@fzu.cz

* Corresponding author

Keywords:
beam splitting; donut-shaped beams; laser ablation in liquids; nanoparticle productivity; size control

Beilstein J. Nanotechnol. **2026,** *17,* 1605–1623.
https://doi.org/10.3762/bjnano.17.110

Received: 11 September 2026
Accepted: 22 October 2026
Published: 12 November 2026

This article is part of the thematic issue "Laser material processing in liquids for nanoparticle synthesis".

Guest Editor: G. Mínguez-Vega

© 2026 Bérard et al.; licensee Beilstein-Institut.
License and terms: see end of document.

Abstract

Pulsed laser ablation in liquids (PLAL) is a versatile and sustainable technique for the synthesis of ligand-free colloidal nanoparticles, but its wider application is limited by relatively low productivity and insufficient control over particle size distributions. Here, to advance the technique, we investigate the possibility of combining in one synthesis process the advantages of two recently developed cost-effective approaches, multibeam PLAL for productivity increase and donut-shaped laser beams for particle size modification. Nanoparticles of gold, an iron–nickel alloy, and a high-entropy alloy were produced in water using single-beam and multibeam configurations with four and eleven picosecond sub-beams. The effects of beam profile, beam-splitting factor, and laser fluence on particle yield and size distributions were systematically evaluated. Splitting donut-shaped beams is shown to offer a similar productivity increase as Gaussian pulses, and, at moderate fluences, multiple donut beams can be even more efficient. A single donut-shaped beam generally reduces the particle size, but, in a multibeam configuration, the reduction effect is hindered by secondary processes such as the interaction of cavitation bubbles, nanoparticle fragmentation, and redeposition. The results demonstrate the feasibility of combining donut-shaped beams with multibeam ablation in PLAL synthesis and identify key process parameters that have to be optimized to achieve both high productivity and improved particle size control.

Introduction

Pulsed laser ablation in liquids (PLAL) has emerged as a versatile and inherently green route for nanoparticle (NP) synthesis [1-4]. Owing to its one-step nature, the absence of added chemical reagents, its applicability to a broad range of solid materials, and the direct production of colloidal NPs suitable for subsequent processing, PLAL provides a convenient alternative to

conventional wet-chemistry routes for applications in medicine [5-7], catalysis [8,9], sensing [10,11], and additive manufacturing [12,13]. In the broader context of resource scarcity and environmental constraints [14,15], the low material consumption and surfactant-free character of PLAL are particularly attractive.

Despite these advantages, two major limitations still hinder the widespread industrial application of PLAL-produced NPs, namely, relatively low production rates and insufficient control over NP size distributions [16]. The first limitation is caused mainly by the cavitation bubble generated during PLAL, which shields the subsequent laser pulses thus reducing the ablation rate and hence the NP synthesis productivity [2,17,18]. Other shielding effects, including those caused by persistent microbubbles [19] and suspended nanoparticles [2,20], as well as redeposition processes [21], and nonlinear absorption [2,22] can also reduce ablation efficiency in liquids. The second challenge, namely, obtaining narrow, unimodal NP size distributions, is associated with several mechanisms involved in NP formation, growth, and fragmentation during PLAL. The interplay among these mechanisms often results in several NP populations and, consequently, broad or bimodal size distributions [2,23-26].

Considerable efforts have been made to overcome these two limitations of the PLAL technique. Various strategies have been employed to increase the ablation efficiency in liquid environments and thus enhance the NP yield, including optimization of irradiation conditions [27-30] and target geometry [31-33], the use of liquid-flow reactors [34,35] and spatiotemporal focusing [22]. A milestone in upscaling PLAL synthesis was achieved by Streubel et al. [17], who demonstrated the industrial-scale level of NP synthesis productivity by using a combination of a high-repetition-rate laser, liquid flow, and rapid, supersonic scanning of the laser beam over the target, thus bypassing the cavitation bubble. However, the fast polygon scanner employed in this approach is an expensive and technically complex component, which may limit its widespread practical use. More recently, a multibeam (MB) PLAL technique was developed [18,36,37] that allows the cavitation-bubble shielding effect to be mitigated both temporally and spatially through the use of inexpensive diffractive optical elements (DOEs). The MB-PLAL method has demonstrated NP synthesis productivity comparable to that achieved using polygon scanners, while providing a potentially more reliable and cost-effective approach.

Extensive research has been conducted to achieve control over size distributions of PLAL-produced NPs and reduce their width. Several strategies have been developed including tuning the PLAL processing parameters [2,38-40], quenching of NP growth by adding surfactants [41,42], ligands [43], and low-salinity ions [44], as well as varying liquid media [45] and using two-step laser synthesis involving ablation and fragmentation [46,47]. However, most of the developed NP size-tailoring techniques are not universal and are effective only for specific materials. Moreover, the addition of stabilizers compromises one of the principal advantages of PLAL, namely, its ability to produce surfactant- and ligand-free NPs, and may therefore limit the versatility and applicability of the resulting colloids. Furthermore, one optimized tailoring parameter often affects the others. For instance, narrowing the NP size distribution by reducing laser fluence leads to a drawback of lower productivity [2]. Recently, a new optical approach was developed to modify the size distributions of PLAL-produced NPs by using donut-shaped (DS) laser beams instead of conventional Gaussian beams [37,48]. Experiments with various material classes, including metals, alloys, and oxides, demonstrated that PLAL with DS beams can significantly reduce particle size, narrow the size distribution, and improve particle sphericity.

In this study, building on these recent developments, we investigated the simultaneous implementation of MB-PLAL and picosecond DS laser pulses to combine high productivity and enhanced NP size control within a single PLAL configuration. Colloidal NPs of three materials, gold (Au), an iron–nickel (FeNi) alloy, and a high-entropy alloy (HEA), were produced in water using this approach. The selected materials exhibit substantially different thermophysical properties, particularly different laser-ablation thresholds, while their NPs are also relevant to a wide range of applications. The resulting colloids were characterized in terms of NP synthesis productivity and particle size distribution. Their characteristics were compared with those of NPs produced from the same materials using single-beam PLAL with Gaussian laser pulses.

Experimental

Pulsed laser ablation in water

The PLAL setup is schematically shown in Figure 1. The target is positioned in a vertical flow-through aluminium chamber (internal dimensions are $85 \times 30 \times 10$ mm^3) using double-sided adhesive tape. The tested targets were polycrystalline $Fe_{0.5}Ni_{0.5}$ alloy ($1 \times 20 \times 70$ mm^3, 99.95%, Sindlhauser Materials GmbH, Germany), high-entropy Cantor alloy $Co_{0.2}Cr_{0.2}Fe_{0.2}Mn_{0.2}Ni_{0.2}$ ($1 \times 20 \times 70$ mm^3, 99.5%, Sindlhauser Materials GmbH), and Au ($1 \times 20 \times 70$ mm^3, 99.99%, EVOCHEM Advanced Materials GmbH, Germany). The flow rate of demineralized water (Synergy Water Purification System) was adjusted to 300 mL/min using a peristaltic pump that ensured complete filling of the chamber volume under laminar flow conditions (the Reynolds number is ≈140).

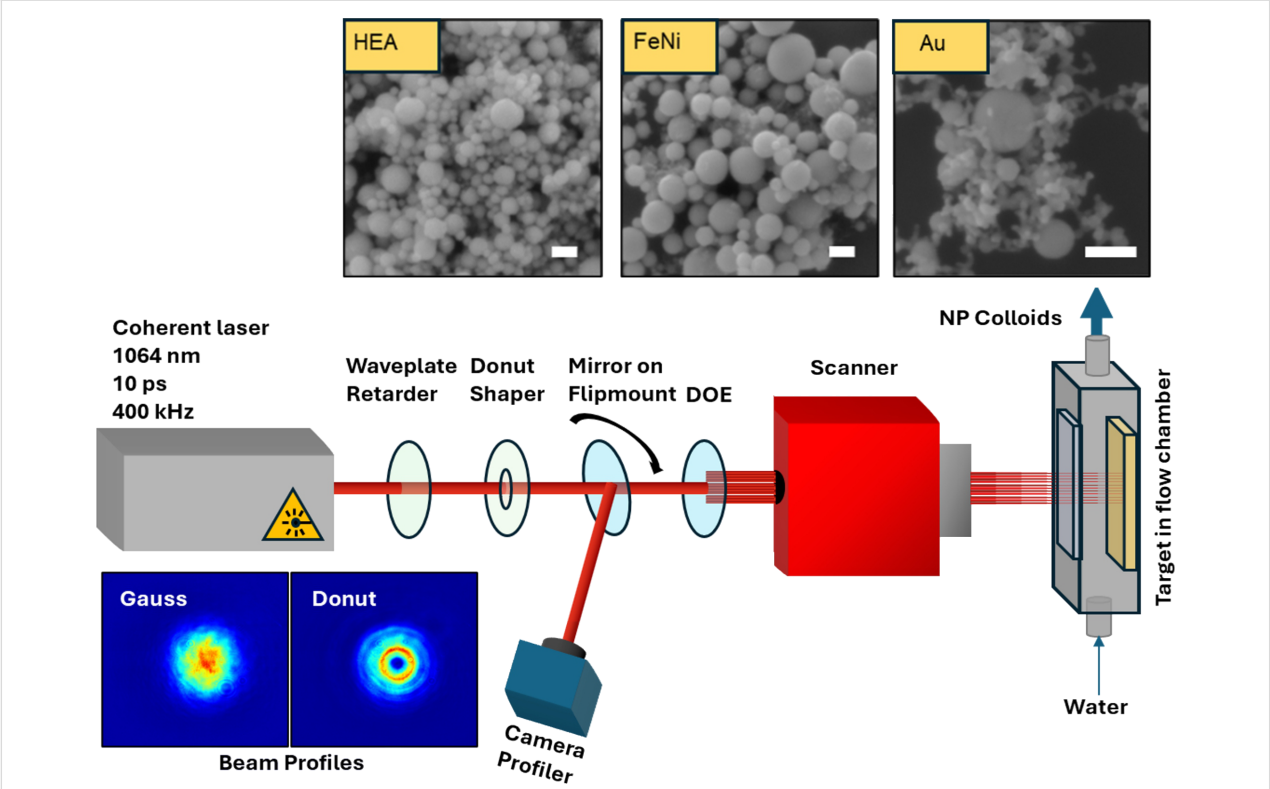

Figure 1: Schematic presentation of the PLAL setup. A donut shaper and a DOE (1×4 or 1×11) can be placed or removed from the beam path to provide different combinations of the beam shaping. The beam profiles (bottom left) are acquired prior to the experiments by flipping a mirror to redirect the beam toward a camera. The inset at the top shows typical SEM images of NPs of the three materials obtained with the donut shaper and the 1×11 DOE (scale bar is 100 nm).

The targets were irradiated at normal incidence through the chamber glass window by a Nd:YAG laser (HyperRapid NXT, Coherent Corp., pulse duration 10 ps, wavelength 1064 nm, maximum power 120 W) at a repetition rate of 400 kHz. The output beam had a diameter of 5 mm and a Gaussian intensity profile. A galvo scanner SUPERSCAN IV-15 (Raylase GmbH, Germany) equipped with an f-theta lens (focal distance 167 mm) was used to focus and scan the beam at the target surface with a scanning speed of 20 m/s. The scanning patterns depended on the irradiation conditions as specified in Table 1. The beam power in front of the flow chamber was varied in the range of 3–82 W using a laser attenuator and monitored by a power meter Puls2 (LaserPoint, Vimodrone, Italy). In all experiments, the target was located at the focal plane, unless specified otherwise, and irradiated for 5 min to obtain ≈1.5 L of colloid for every PLAL regime.

Three types of spatial shaping of the laser beam were investigated. First, a radially polarized DS beam was produced from the original Gaussian beam using a half-waveplate in combination with a S-waveplate convertor (Workshop of Photonics, Vilnius, Lithuania). The resulting beam shape was controlled using a beam profiler CMOS-1.001-Nano-UV (CINOGY Technologies, Duderstadt, Germany). As the polarization of DS pulses was found to barely affect the PLAL-produced NPs [47], azimuthal polarization was not investigated here. Second, the output beam was split into n sub-beams using static DOEs for multibeam PLAL. Two different DOEs were placed after the galvo scanner to obtain at the target either a horizontal line of four spots separated by 0.7 mm (1×4 DOE, 0.28° beam separation angle, HOLO/OR, Ness Ziona, Israel) or a vertical line of eleven spots separated by 4 mm (1×11 DOE, 1.2° beam separation angle, LIMO Lissotschenko Mikrooptik GmbH, Dortmund, Germany). The DOEs were installed after the lens of the scanner in order to accommodate the use of a large scanning pattern with the 1×11 DOE. Finally, the DOEs were combined with the DS convertor to investigate PLAL with multiple DS beams. The NPs produced with the shaped laser pulses were compared with those obtained in the standard PLAL regime with a single Gaussian beam at different laser fluences.

The combination of the different shaping elements leads to a large variety of experimental conditions with different sub-beam energies and fluences. The investigated ablation regimes are summarized in Table 1. The selected set of conditions enables comparison of different regimes at nearly identical

Table 1: Irradiation conditions. For multibeam configurations, pulse energy and fluence correspond to individual sub-beams.

	Power notation	Total power, W	Pulse energy, µJ	Fluence, J/cm^2		Scanning pattern
				Gauss	Donut	
single beam	P_0	81.2	203	12.6[a]	5.0[a]	spiral
	P_0/2.7	32.6	81.5	9.0	—	
	P_0/4	21.8	54.5	6.0	2.2	
	P_0/11 or P_0/4/2.7	8.9	22.3	2.5	0.90	
	P_0/11/2.7	3.4	8.5	0.9	—	
DOE 1×4	P_0	81.2	50.8	5.6	2.1	raster
	P_0/2.7	32.6	20.4	2.2	—	
DOE 1×11	P_0	81.2	18.5	2.0	0.75	spiral
	P_0/2.7	32.6	7.4	0.82	—	

[a]The target was shifted 2 mm out of focus to avoid damage of the chamber window.

energy and/or fluence in an individual sub-beam, that is, at comparable PLAL conditions, in the fluence range of 0.7–13 J/cm^2. The peak fluences for Gaussian beams were evaluated using an effective spot diameter of 48 µm (focal plane, $1/e^2$ criterion) measured for this setup previously [18]. For donut-shaped beams at the same pulse energy and focusing conditions as for Gaussian beams, the fluence is lower by a factor of ≈2.7 [48,49]. Therefore, to obtain identical fluences in individual sub-beams, the pulse energy of a single Gaussian beam was reduced by a factor of n = 4 or 11 when comparing with multibeam PLAL or by a factor of 2.7 when comparing with donut-shaped beams. Note that the beam splitting with a DOE does not change the shape of the original beam [18]. Note also, that, due to different splitting angles and beam-array dimensions of the used DOEs, different beam scanning patterns were used. For a single beam and 11 sub-beams, this was a hollow spiral with outer and inner diameters of 10 and 4 mm, respectively [50], while for the 1×4 DOE, this was a raster pattern over an area of 6 × 10 mm^2 [18]. The irradiated area per sub-beam was nearly identical for both DOEs, approximately 60 mm^2. With the 1×4 DOE, all four beams irradiated this area, whereas with the 1×11 DOE, it was exposed to one beam and, owing to the overlap of adjacent spiral patterns, it was additionally irradiated by two neighboring beams. Consequently, the number of laser pulses accumulated per spot was approximately two times lower for the 1×11 DOE. To ensure comparable pulse accumulation, the target was shifted to a fresh area after 1×4 DOE runs twice as frequently as for PLAL runs with the spiral scanning pattern.

Characterization

The productivity of NP synthesis was determined from the target mass loss during PLAL. The targets were dried in an oven, cooled down on a metallic plate, and weighed using an analytical balance (Gram, FS220, resolution 0.1 mg) before and after each PLAL experiment. For NP size characterization, approximately 100 mL of colloid was collected after 2 to 3 min of irradiation. The obtained sample was drop-cast and dried on a piece of a ⟨100⟩ silicon wafer, and the deposited NPs were analyzed using a scanning electron microscope (SEM, TESCAN MIRA3 LMH). For each sample, several images were acquired at different places of the droplet to investigate more than 1000 NPs per sample. Particle sizes were extracted from the SEM images using ImageJ. The resulting particle size datasets were subsequently processed using a dedicated script implemented in OriginPro. The script was used to calculate, directly from the experimental data, the median size $\langle D \rangle$, the median absolute deviation (MAD), and the robust coefficient of variation, RCV = MAD/$\langle D \rangle$ [51], and to perform lognormal fitting of the size distributions. A two-component lognormal model was used to approximate the bimodal distributions of Au NPs. Details of the statistical analysis and fitting procedure are provided in Supporting Information File 1.

Results and Discussion

Figures 2, 3, and 4 provide an overview of the productivity and size distributions for PLAL-produced NPs of HEA, FeNi, and gold, respectively. These two key characteristics of the PLAL process are discussed below in the context of various beam-shaping approaches.

Productivity

The obtained productivity values in different PLAL regimes are summarized in Table 2. The accuracy of the obtained values is estimated to be within 5% based on two to three independent measurements for several selected PLAL regimes and our

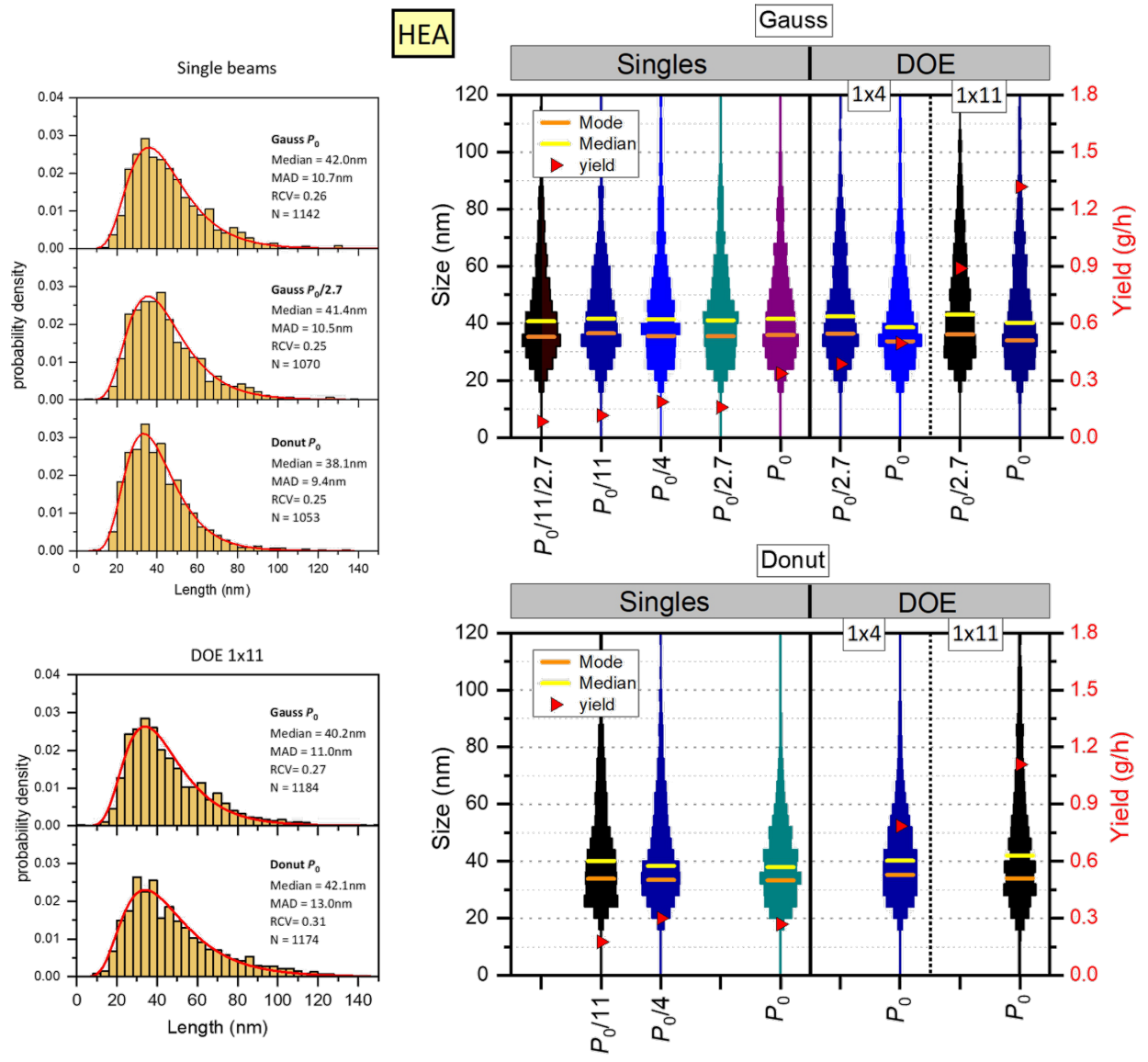

Figure 2: Summary of results for HEA NPs. Left: Examples of size distributions of NPs produced by single Gaussian and DS beams at different powers (top), and by eleven Gaussian and donut-shaped sub-beams at maximal power (bottom). The lines represent lognormal fits. The indicated median size, median absolute deviation (MAD), and robust coefficient of variation (RCV) are derived directly from the particle size data. The number of measured nanoparticles (*N*) is also indicated. Right: The violin plots showing the NP size distributions for all the samples obtained with Gaussian (top) and donut-shaped (bottom) beams as a function of the total laser power. The plots for an identical fluence have the same color. The mode (orange lines) and median (yellow lines) values are obtained from lognormal fits. The right axis shows the productivity (red triangles).

previous similar studies [18]. The uncertainty originates mainly from the fact that the PLAL process is not entirely reproduced under the same irradiation conditions, but not from the errors in the balance measurement (which are virtually negligible).

Fluence effect for a single Gaussian beam

Laser fluence is one of the most important parameters affecting the PLAL process and determining the NP synthesis productivity [2]. Above a threshold fluence for ablation, the ablation rate, and therefore the productivity, increase gradually until reaching a limitation due to effects such as cavitation-bubble shielding and optical breakdown. In the absence of these limitations (e.g., when the cavitation bubble is effectively bypassed), the ablation rate follows the fluence dependence in air, suggesting that there exists an optimal fluence F_{opt} with the maximal productivity per average input laser power [2,17]. According to a simple model [52], the optimal fluence of ultrashort laser pulses in air can be estimated as

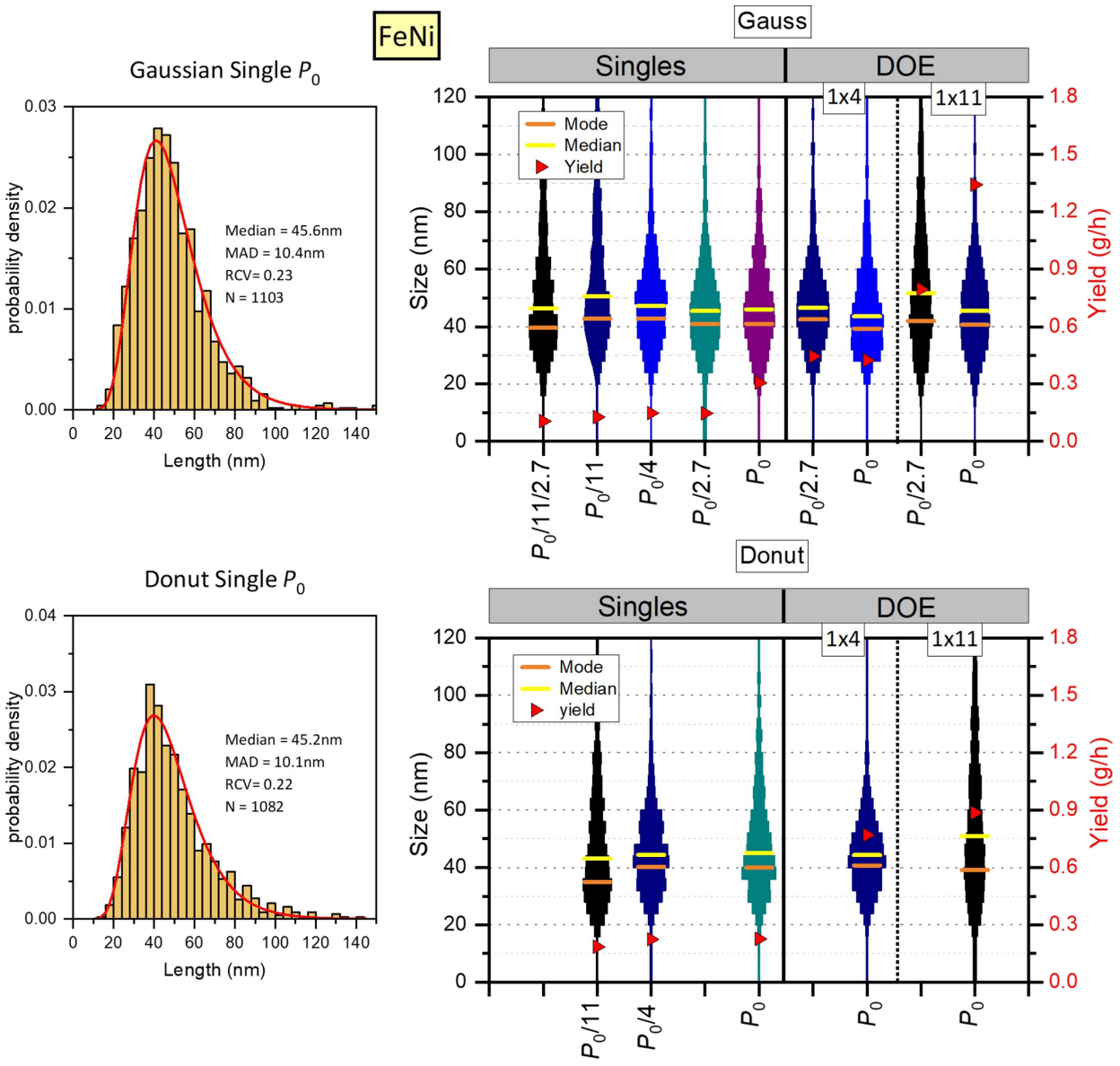

Figure 3: Summary of results for FeNi NPs. Left: Examples of size distributions of NPs produced by single Gaussian and DS beams at maximal power. The lines represent lognormal fits. The indicated median size, median absolute deviation (MAD), and robust coefficient of variation (RCV) are derived directly from the particle size data. The number of measured nanoparticles (*N*) is also indicated. Right: The violin plots showing the NP size distributions for all the samples obtained with Gaussian (top) and donut-shaped (bottom) beams as a function of the total laser power. The plots for an identical fluence have the same color. The mode (orange lines) and median (yellow lines) values are obtained from lognormal fits. The right axis shows the productivity (red triangles).

$$F_{\text{opt}} = e^2 F_{\text{th}}, \tag{1}$$

where e is the Euler constant and F_{th} is the ablation threshold.

The obtained single-beam productivity values follow the general fluence behavior for Gaussian beams with a gradually increasing dependence for gold and with signs of saturation at fluences above ≈6 J/cm^2 for HEA and FeNi (Figure 5a). The data obtained at the highest laser power, P_0, were excluded here because they were acquired using a larger irradiation spot and were therefore not directly comparable with the remaining data. Figure 5b shows the productivity data normalized to the average power (i.e., the specific NP yield) as a function of laser fluence. The expected maximum at an optimal fluence is observed only for gold while HEA and FeNi exhibit gradually decreasing fluence dependencies.

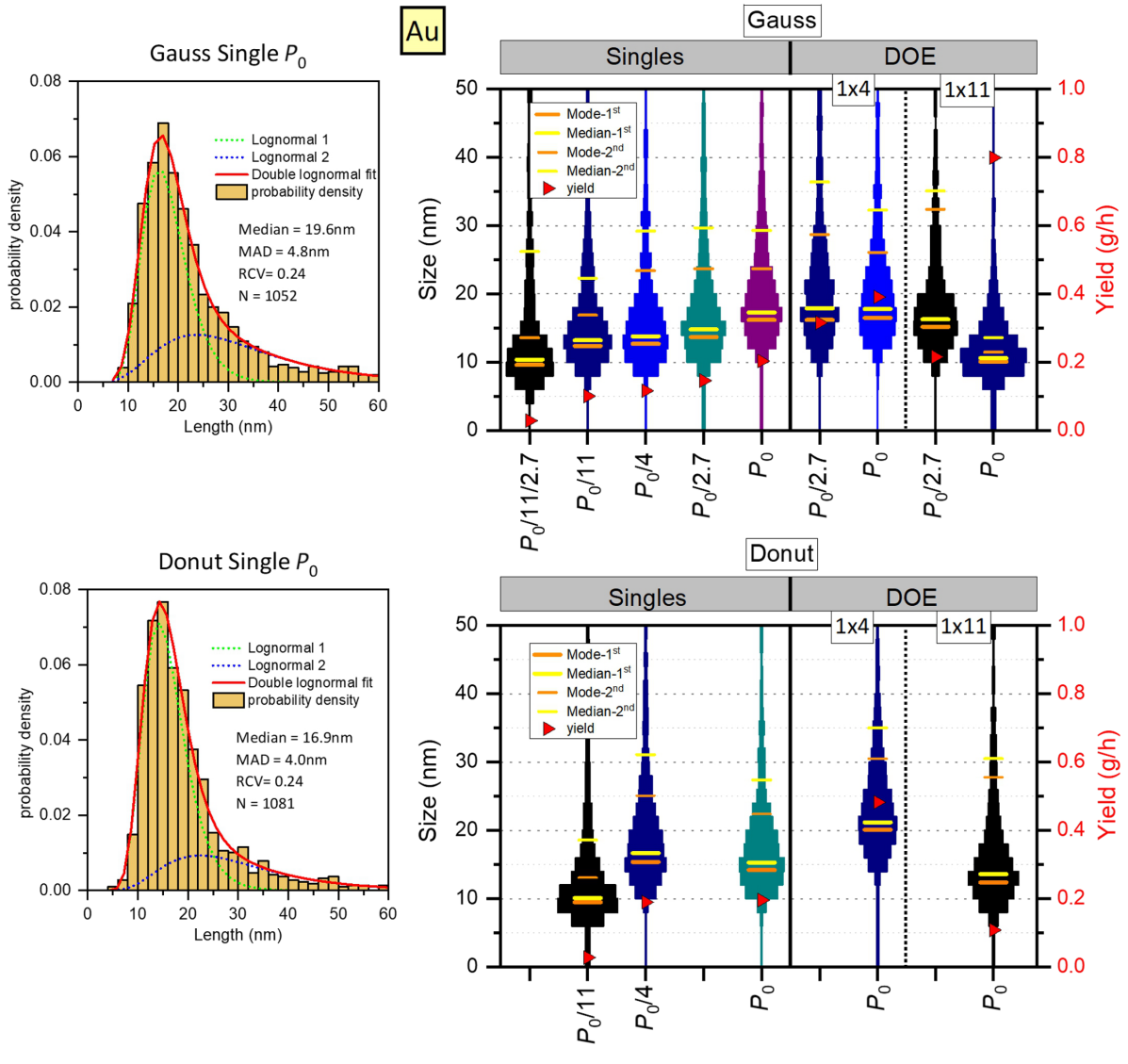

Figure 4: Summary of results for Au NPs. Left: Examples of size distributions of NPs produced by single Gaussian and DS beams at maximal power. The NP size distributions are approximated by two lognormal functions for small (green dotted lines) and large (blue dotted lines) NP populations. The indicated median size, median absolute deviation (MAD), and robust coefficient of variation (RCV) are derived directly from the particle size data. The number of measured nanoparticles (*N*) is also indicated. Right: The violin plots showing the NP size distributions for all the samples obtained with Gaussian (top) and donut-shaped (bottom) beams as a function of the total laser power. The plots for an identical fluence have the same color. The mode (orange lines) and median (yellow lines) values are obtained from lognormal fits and are given for both NP populations. The right axis shows the productivity (red triangles).

The expected optimal fluences for the ideal situation of completely bypassing the cavitation bubble can be estimated using Equation 1. The single-shot ablation thresholds in water for picosecond near-IR laser pulses were reported as 3.36 J/cm^2 for gold and 1.3 J/cm^2 for FeNi [21]. Under multishot irradiation, as in our case, the threshold fluence is lower due to incubation effects [53-55]. The decrease of the threshold with the number of pulses N was found to follow the equation:

$$F_{\mathrm{th}}(N) = F_{\mathrm{th}}(1) N^{S-1}, \qquad (2)$$

where $F_{\mathrm{th}}(1)$ is the single-shot threshold and S is an accumulation coefficient whose value for metals and picosecond pulses is typically 0.8 [54], although weaker dependencies were also reported [56]. The average pulse number per spot during our 5 min PLAL experiment can be estimated as $N \approx 3600$ assuming uniform irradiation over the scanning patterns. Then, taking $S = 0.8$, we obtain from Equation 2 the multishot ablation thresholds of 0.65 J/cm^2 for gold and 0.24 J/cm^2 for FeNi. For the HEA CoCrFeMnNi, the multishot threshold for ablation conditions similar to those in this study was reported as 0.36 J/cm^2 [50]. The expected optimal fluences, according to

Table 2: Productivity of NP synthesis (in mg/h) for different PLAL regimes. The values in parentheses indicate the percentage of the productivity of an individual sub-beam in MB-PLAL compared to the single-beam regime at the same laser fluence.

	Power notation	FeNi		HEA		Au	
		Gauss	Donut	Gauss	Donut	Gauss	Donut
Single beam	P_0	307	227	336	269	204	196
	P_0/2.7	146	—	159	—	146	—
	P_0/4	148	224	187	300	116	190
	P_0/11 or P_0/4/2.7	127	185	116	176	101	27.6
	P_0/11/2.7	106	—	84.0	—	28.8	—
DOE 1×4	P_0	425 (72%)	769 (86%)	496 (66%)	785 (65%)	391 (84%)	482 (63%)
	P_0/2.7	445 (88%)	—	386 (83%)	—	316 (78%)	—
DOE 1×11	P_0	1341 (96%)	886 (40%)	1318 (103%)	1109 (57%)	799 (72%)	108 (36%)
	P_0/2.7	796 (68%)	—	889 (96%)	—	216 (68%)	—

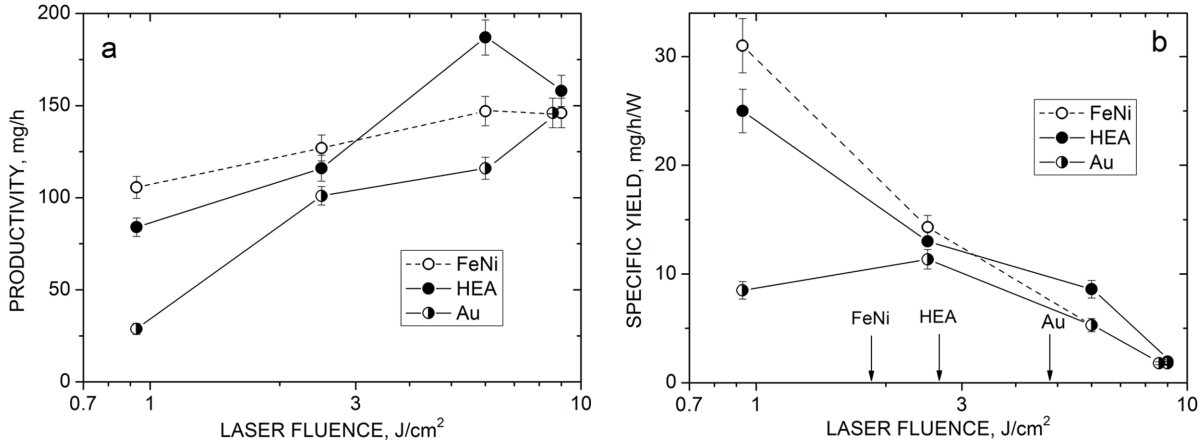

Figure 5: Mass productivity (a) and power-specific productivity (b) of FeNi, HEA, and gold NPs produced by a single Gaussian beam as a function of laser fluence. The arrows in (b) show expected optimal fluences evaluated from Equation 1 (see text for details).

Equation 1, are therefore 4.8, 2.66, and 1.85 J/cm^2 for Au, HEA, and FeNi, respectively (Figure 5b).

For all three materials, the experimentally observed PLAL conditions corresponding to the maximum specific NP yield are shifted toward lower fluences relative to the values estimated using the air-ablation model (Figure 5b). This indicates that the cavitation bubble is not completely bypassed under the considered conditions, which reduces the NP synthesis productivity in the single-beam regimes. Indeed, although the interpulse distance under our PLAL conditions (50 µm for the 400 kHz pulses scanned at 20 m/s) is almost the same as the spot diameter (48 µm) and thus the nominal spot overlap is negligible, the cavitation bubble grows during the interpulse time (2.5 µs) to larger lateral sizes, above 100 µm, under the considered conditions [18]. Therefore, the bubble shields and reflects the incoming next pulse, reducing the productivity (ablation rate) [2]. The shielding effect is particularly pronounced at high fluences, when the bubble grows faster [18,57]; thus, the optimal irradiation conditions are shifted towards lower fluences, and beyond the optimum, the specific NP yield drops rapidly with fluence (Figure 5b). These limitations for NP synthesis productivity can be overcome by using the multibeam PLAL approach [18,36,37].

Multibeam approach

Beam splitting with different splitting factors has recently been demonstrated as an efficient and low-cost method to increase the productivity of the PLAL NP synthesis for Gaussian beams [18,36,37]. The advantage of the approach relies not only on a

larger number of laser beams but, more important, on the possibility of bypassing the cavitation bubble [18]. Here we demonstrate the increase in productivity by MB-PLAL of the three studied materials. Figure 6 compares the NP yields for single-beam and MB regimes at identical laser powers of P_0/2.7 and P_0 (full power) in the case of Gaussian pulses. Note that, at a fixed total power, the laser fluence of an individual sub-beam in the MB-PLAL is lower than that in a single beam by the splitting factor n (Table 1). For all the materials, the MB-PLAL technique offers substantial increases in net productivity. At a P_0/2.7 power, the highest benefit from the splitting is for FeNi, a material with the lowest ablation threshold and a weak fluence dependence of the ablation yield (Figure 5a). Thus, a small reduction in the sub-beam productivity with fluence decreased from 9 to 2.2 J/cm^2 by the 1×4 DOE is more than compensated by the fourfold increase in the number of beams resulting in the productivity gain by a factor k = 3.0 while those for HEA and Au are 2.5 and 2.2, respectively (Figure 6a). For the 1×11 DOE, the productivity increases by a factor of ≈5.5 for both FeNi and HEA, while only 1.5 times for gold. The small increase in the latter case is likely because of the low fluence in a sub-beam, close to the gold ablation threshold. With the full power, the productivity gain with the 1×4 DOE for all the materials is reduced (k = 1.5, 1.4, and 1.9, for HEA, FeNi, and Au, respectively, Figure 6b), probably due to limitations imposed by the cavitation bubble, which is fairly large and long-lived at this fluence. With the 1×11 DOE, the sub-beam fluence is below 1 J/cm^2, the bubble-induced limitations are apparently minor, and the productivity increase factor remains high (≈4) for all three materials.

The selected regimes (Table 1) enable us to evaluate potential losses in the productivity of an individual sub-beam in the MB-PLAL relative to a single-beam PLAL at identical fluences. The numbers in parentheses in Table 2 represent the percentage of a split sub-beam productivity compared to the corresponding single-beam PLAL. With the 1×11 DOE, the efficiency of a sub-beam is close to 100% in most cases (except for gold, where sub-beam fluences in these MB regimes are well below optimal values). This is consistent with the large spot separation in this case (4 mm), when significant interaction of simultaneously produced bubbles is unlikely, so there are no productivity losses. The interspot distance is much shorter for the 1×4 DOE (0.7 mm), which may promote bubble interaction [58], thus reducing the sub-beam productivity to ≈85% at P_0/2.7 and ≈70% at P_0 (Table 2). The bubble interaction can also affect the sizes of the produced NPs [58]; thus, the spot separation is an additional important factor in the MB-PLAL regimes.

We should underline that the possibilities of the splitting technique to bypass the cavitation bubble and to increase the PLAL productivity are not fully exploited in this study. The pulse repetition rate is fixed here in all the regimes, and thus the bypassing effect under MB-PLAL conditions is based merely on a smaller size and shorter lifetime of the bubble induced by a lower-fluence sub-beam. However, the bubble can be temporally bypassed more efficiently by reducing the repetition rate and therewith keeping the sub-beam fluence at a fairly high optimal level at the same total laser power [18,37]. We therefore expect that a considerably higher synthesis efficiency than that obtained here (Figure 5) can be gained in the MB-PLAL by choosing a proper combination of the splitting factor, pulse repetition rate, spot size, and spot separation at a given laser power. Such an optimization is, however, beyond the scope of this work.

Donut-shaped beams

Introducing a donut shaper into the system modifies considerably the irradiation conditions and leads to new factors affecting the PLAL productivity. First, the peak fluence is 2.7 times

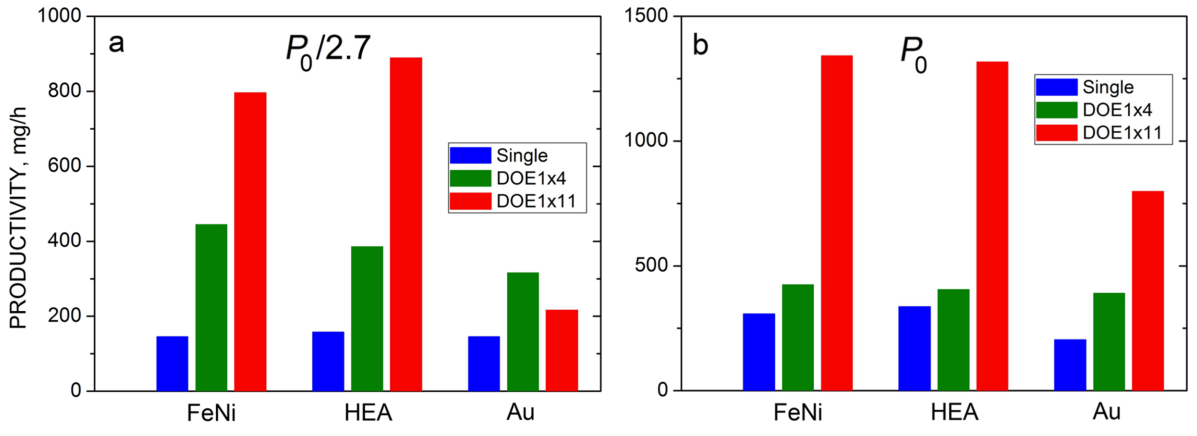

Figure 6: Productivity of FeNi, HEA, and Au NPs in single-beam PLAL and MB-PLAL with Gaussian pulses at P_0/2.7 (a) and P_0 (b) laser powers.

lower than that with a Gaussian beam at the same pulse energy [37]; this could reduce the ablation rate, in particular at low fluences, near the ablation threshold. Second, the irradiation spot area with a DS pulse is larger and more uniformly heated [48], which can be, in contrast, a favorable factor for the productivity, especially at moderate and high fluences, when the productivity is expected to have only a weak dependence on fluence, similar to Gaussian pulses (Figure 5a). Third, due to a larger spot, the lateral size of the cavitation bubble produced by a DS pulse is also larger, at least at initial stages, which can promote the bubble shielding effect and interaction of neighboring bubbles, thus reducing the productivity, especially at high fluences. Finally, the time evolution of the bubble is more complicated than that induced by a Gaussian pulse with asymmetric expansion and collapse that reduces the bubble lifetime and apparently affects both yield and size of the produced NPs [37,48].

The observed trends are consistent with the above considerations. Indeed, the productivity with a single DS pulse at a moderate fluence of 2.2 J/cm^2 (P_0/4) is 1.5–1.6 times higher than that with a Gaussian pulse at the same power for all three materials (Figure 7a). This is likely due to a larger and more uniformly irradiated DS laser spot. A similar gain in productivity with the DS pulse is observed at an even lower fluence (0.9 J/cm^2, P_0/11) for HEA and FeNi, while for Au, the productivity drops dramatically to ≈4 times lower than that of the Gaussian beam (Table 2). The latter is obviously because the sub-beam fluence at P_0/11 is too low for gold, near the ablation threshold. The markedly stronger productivity decrease observed for Au compared with FeNi and HEA is likely related to the proximity of the DS-beam fluence to the Au ablation threshold. The DS sub-beam fluence in the P_0/11 regime (0.75 J/cm^2) exceeds the estimated multishot threshold for Au (0.65 J/cm^2) only marginally, whereas it remains approximately two and three times above the corresponding thresholds for HEA and FeNi, respectively. Under such near-threshold conditions, the Au ablation yield becomes particularly sensitive to local fluence variations, shielding effects, and possible redeposition processes, resulting in a substantially stronger productivity degradation.

When the fluence of the Gaussian beam is reduced to the same value of 0.9 J/cm^2 at P_0/11/2.7, the productivity is also low and similar to that of the DS pulse at P_0/11 (Table 2). On the other hand, when the power increases from P_0/4 to P_0, the productivity of the DS pulses is not practically changed (and even drops for HEA) while that of the Gaussian pulses still increases (Table 2). This indicates that the bubble-induced shielding is indeed stronger for DS pulses at high fluences.

Note that at near-threshold fluences, DS pulses do not provide an advantage in productivity over Gaussian pulses due to a larger irradiated area, as observed at moderate fluences. This may be associated with a more efficient redeposition of the ablated material back to the target surface in the PLAL process with DS pulses. The redeposition was shown to be responsible for reducing the material removal efficiency in liquids, as compared with air, at low fluences, when the ablated layer does not propagate far from the target and eventually redeposits onto the surface [21]. With DS pulses, the redeposition effect is likely more pronounced since both the propagation distance and lifetime of the ablation plasma plume are shorter than for plasmas induced by Gaussian pulses, as was demonstrated in plasma imaging experiments [59]. The observed productivity decrease with near-threshold DS pulses can therefore be due to a combi-

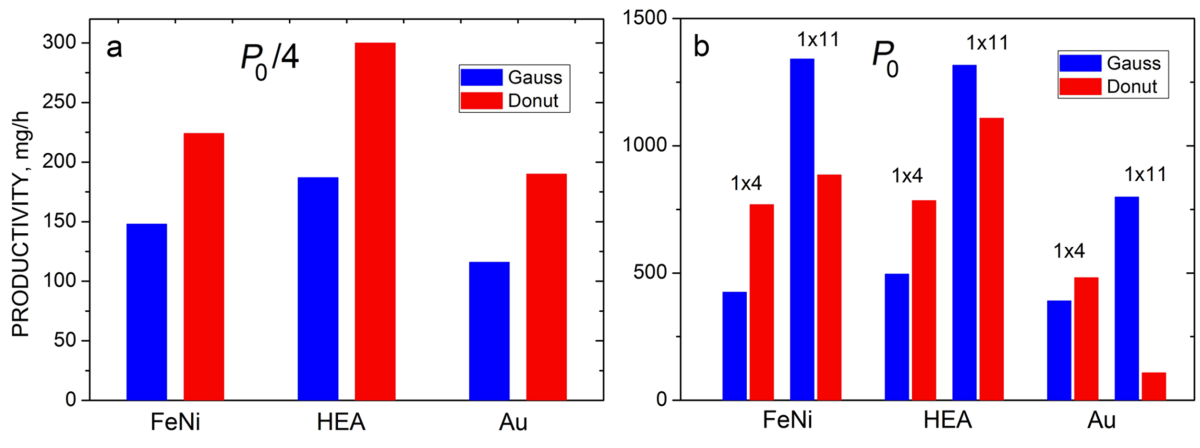

Figure 7: Comparison of the NP productivities of Gaussian and donut-shaped pulses in single-beam PLAL at a P_0/4 power (a) and in MB-PLAL with the 1×4 and 1×11 DOEs at the full laser power (b).

nation of two factors. First, the lower fluence of DS pulses makes the process more sensitive to threshold-related reductions in ablation efficiency. Second, shorter propagation distances and lifetimes of the ablation plasma may promote redeposition of ablated material onto the target surface. The present experiments do not allow these contributions to be separated quantitatively; thus, enhanced redeposition should be regarded as a plausible contributing mechanism rather than a directly verified explanation.

A comparison of the productivities of Gaussian and DS pulses in the MB-PLAL regimes shows similar tendencies as for single beams (Figure 7b). With the splitting factor $n = 4$ at the full power, when the sub-beam fluence is kept at a moderate value of 2.1 J/cm^2, the DS pulses are again more efficient than Gaussian ones at the same power and DOE. The gains are 1.8, 1.6, and 1.2 for FeNi, HEA, and Au, respectively, that is, close to the increase factor of 1.5–1.6 for single beams. With the 1×4 DOE, the efficiencies of individual DS and Gaussian sub-beams relative to the corresponding single-beam PLALs at the same fluence are on a similar level of 70–80% (the number in brackets in Table 2). This indicates that the DOE does not modify the DS beam profile and that the simultaneously produced bubbles do not interact significantly. The obtained productivity increase factors with four DS beams at the full power compared to a single DS beam are 3.4, 3.0, and 2.5 for FeNi, HEA, and Au, respectively (Table 2), that is, considerably higher than the corresponding increases for Gaussian beams. With the 1×11 DOE, when the fluence of individual DS sub-beams is near the ablation threshold, their productivity is well below that of 11 Gaussian beams (Figure 7b), again in agreement with the above considerations of the low efficiency of low-fluence DS pulses. Note that the individual fluence of a DS sub-beam in the 11-beam PLAL at P_0 was lower than the fluence of the single-beam PLAL at $P_0/11$ (0.75 instead of 0.9 J/cm^2, Table 1). Such a difference at this near-threshold fluence level appears to be significant, and this is why the observed relative efficiency of the split DS beams (≈40%, Table 2) is considerably lower than that of a single DS beam at $P_0/11$ (70–80%). Nevertheless, the obtained productivities of FeNi and HEA NPs with 11 DS sub-beams are higher than the single-beam values by factors of 3.9 and 4.1, respectively (Table 2), that is, the gains are similar to what was obtained with Gaussian pulses. Only for gold NPs, the productivity of DS pulses with the 1×11 DOE drops significantly due to the near-threshold fluence in this case.

Summarizing this section, we can state that using DS laser pulses in PLAL setups does not substantially reduce NP synthesis productivity, both in single-beam and multibeam configurations. Moreover, at moderate laser fluences (several times the ablation threshold value), DS pulses are more efficient than Gaussian pulses due to a larger and more uniformly irradiated ablation spot. However, at low near-threshold fluences, the productivity of DS pulses significantly drops, which may be associated with enhanced redeposition of the ablated material. Therefore, when choosing the splitting factor in MB-PLAL with DS pulses, this yield reduction effect should be taken into account. The observed fairly high efficiency of DS beams is an important factor in the context of the main motivation of their use, control over the NP size distribution. The size aspects will be considered in the next section.

Size distributions

The results on NP size distributions for different PLAL regimes are summarized in Figures 2–4, 8, and 9, and Table 3. All the obtained size histograms are approximated by a lognormal function (by two functions in the case of gold), as illustrated by line envelopes for selected distributions in Figures 2–4. The indicated median size values $\langle D \rangle$ and the most often appearing data (MOD) values are derived from the lognormal fits. For gold, the provided $\langle D \rangle$ values correspond to the dominant small-particle population of the bimodal fits. The median absolute deviation MAD and the robust coefficient of variation RCV = MAD/$\langle D \rangle$ are obtained directly from the experimental data of NP sizes. Representative SEM images of NPs obtained in all the studied PLAL conditions and the corresponding size distributions are given in Supporting Information File 2 (Figures S1–S12). Below, the effects of the beam shaping conditions at different laser fluences on the size distributions of the studied PLAL-produced NPs are discussed.

Gaussian beams

The size distributions of HEA and FeNi NPs can be reasonably fitted with a single lognormal function (Figures 2 and 3 and Supporting Information Files 1 and 2), and the derived median NP sizes are found to be rather fluence-independent with $\langle D \rangle$ values of around 41 nm for HEA and 46 nm for FeNi in the studied fluence range of 0.9–12.6 J/cm^2, that is, laser powers from $P_0/11/2.7$ to P_0 (Figure 8). Similar mean sizes and weak fluence dependencies were observed recently for PLAL-produced HEA NPs [18,48]. The relative variations of the sizes (RCV values) are also practically fixed at ≈0.25 for HEA NPs and ≈0.21 for FeNi NPs with a tendency to increase at low fluences for the latter (Figure 9). A similar trend of increasing the polydispersity index of the FeNi NP distributions with reducing the fluence was obtained in MB-PLAL regimes [36].

Gold NPs, however, demonstrate a different behavior. Their median sizes are significantly lower than those of HEA and FeNi NPs, and systematically increase with the fluence from 13 nm at 0.9 J/cm^2 to 20 nm at 12.6 J/cm^2 (Figure 8). Another

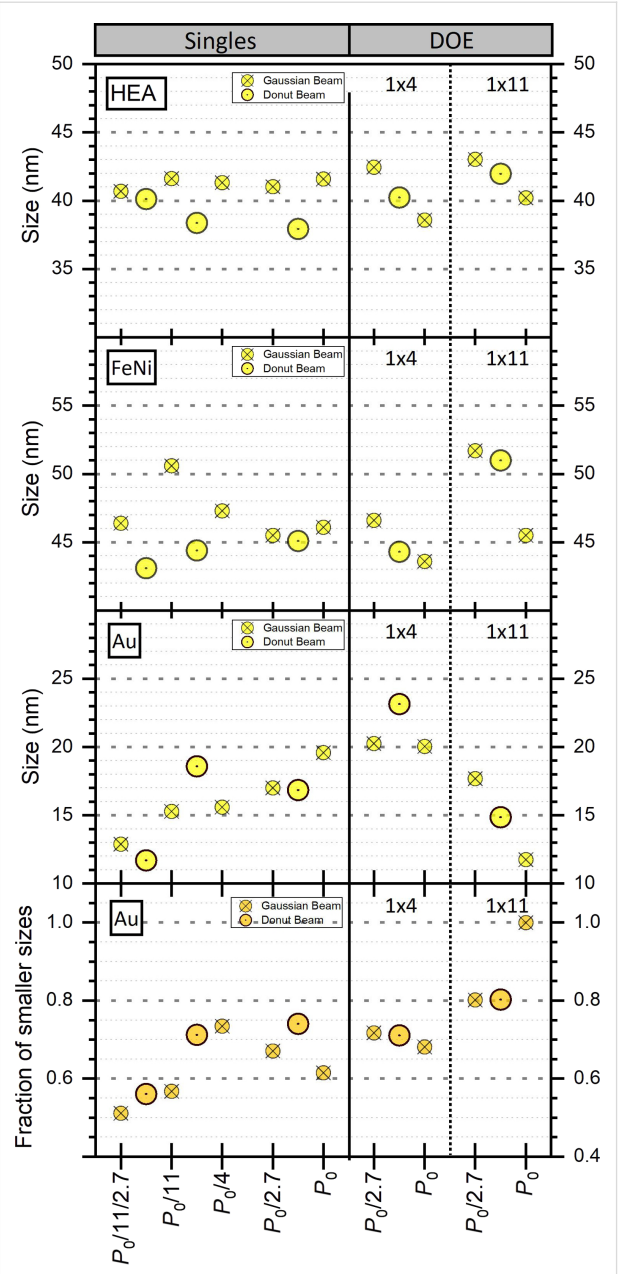

Figure 8: Lognormal fitted median size of HEA, FeNi, and Au NPs produced under various PLAL conditions as a function of the total laser power. For gold, the size is given for the small NP population and the fraction of smaller particles is shown on the bottom panel. For convenience, the results for donut-shaped pulses obtained at a power *P* are placed between *P* and *P*/2.7 (the latter corresponds to the same fluence of a Gaussian pulse at *P*).

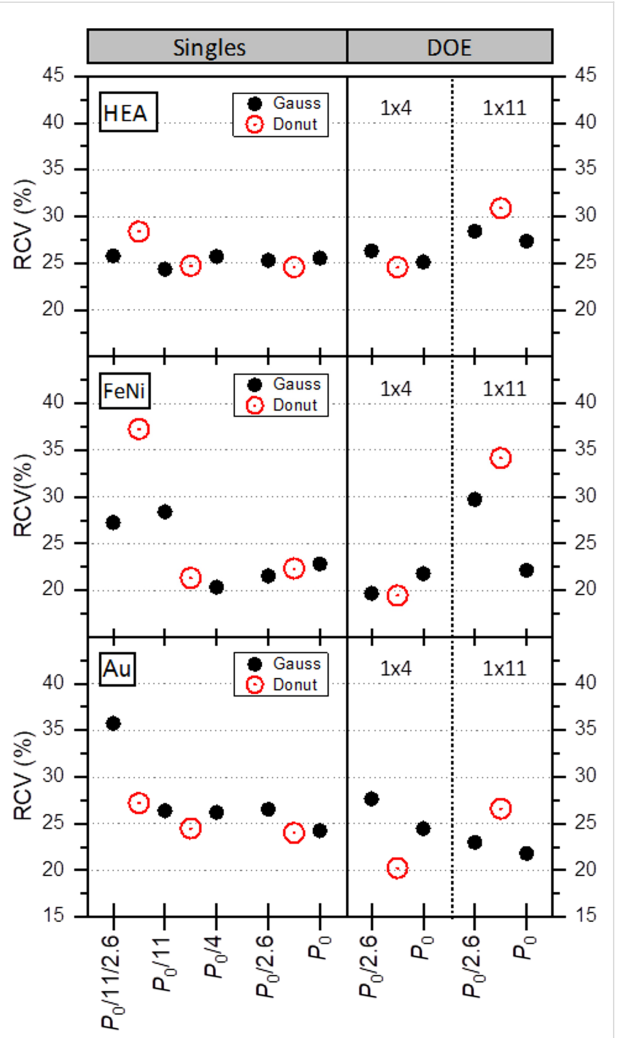

Figure 9: Robust coefficient of variation (RCV) derived from the measured particle sizes of HEA, FeNi, and Au NPs produced under various PLAL conditions as a function of the total laser power. As in Figure 8, the results with donut-shaped pulses are placed between *P* and *P*/2.7.

difference is that the gold size distributions cannot be adequately described by a single lognormal envelope and clearly exhibit two NP populations, smaller and larger ones (Figure 4, Supporting Information File 2, Figures S10 and S12). Such bimodal size distributions are often observed for noble-metal PLAL-produced NPs [23,25,60,61] and are explained by distinct formation mechanisms for the small and large populations [26,60]. In our case, the small NP population dominates, and its fraction increases with fluence (Figure 8). The RCV values of gold NP distributions are therewith almost fixed at the same value of 0.25 as for HEA NPs throughout the studied fluence range (Figure 9). An exception is at the lowest fluence of 0.9 J/cm^2 when the distribution is relatively broad (RCV = 0.35), possibly due to a low pulse-to-pulse reproducibility of the ablation process at the near-threshold fluence.

Splitting the Gaussian beams does not practically affect the size distributions of HEA and FeNi NPs for both 1×4 and 1×11 DOEs (Figure 8 and Figure 9). This indicates that the DOEs, indeed, do not alter the irradiated spot profile and that the interaction of adjacent bubbles simultaneously produced with the 1×4 DOE, if it occurs, has little effect on the size distri-

Table 3: Median size values ⟨*D*⟩ for the NP distributions obtained under different PLAL conditions with the median absolute deviation (MAD) in parentheses (in nm). For Au, the values correspond to the dominant small-particle population.

	Power notation	FeNi		HEA		Au	
		Gauss	Donut	Gauss	Donut	Gauss	Donut
Single beam	P_0	46 (10)	45 (10)	42 (10)	38 (9)	20 (5)	17 (4)
	P_0/2.7	46 (10)	—	41 (10)	—	17 (4)	—
	P_0/4	47 (10)	44 (9)	41 (11)	38 (9)	16 (4)	18 (5)
	P_0/11 or P_0/4/2.7	51 (14)	43 (13)	42 (10)	40 (11)	15 (4)	12 (3)
	P_0/11/2.7	46 (13)	—	41 (11)	—	13 (4.5)	—
DOE 1×4	P_0	44 (9.5)	44 (8.5)	39 (10)	40 (10)	20 (5)	23 (5)
	P_0/2.7	47 (9)	—	42.5 (11)	—	20 (5.5)	—
DOE 1×11	P_0	46 (10)	51 (17)	40 (11)	42 (13)	12 (2.5)	15 (4)
	P_0/2.7	52 (15)	—	43 (12)	—	18 (4)	—

bution. A slight increase in the median size of FeNi NPs is only observed at the lowest fluence (1×11 DOE, P_0/2.7) compared to its single-beam counterpart at P_0/11/2.7 (52 nm instead of 46 nm, Figure 8), which can be explained by the poor reproducibility at low fluences. For gold NPs, the situation is again somewhat different. The median size of NPs produced with the 1×4 DOE for both P_0 and P_0/2.7 is considerably larger (20 nm) than that obtained in the single-beam regimes (15 nm) at the same laser fluences (at P_0/4 and P_0/4/2.7, respectively). This is likely due to a relatively small separation distance between the spots with the 1×4 DOE, which results in the bubble interaction and affects, in this case, not only the NP synthesis productivity (Section "Productivity") but also their size distribution.

A question arises: Why are only gold NPs affected by the bubble interaction, while the median sizes of HEA and FeNi NPs remain virtually unchanged under the same MB-PLAL with the 1×4 DOE? One can envision a thermal feedback effect of the neighboring irradiation spots occurring in gold. Indeed, the thermal conductivity of gold (and particularly its electronic component, which dominates at early ablation stages [62]) is much higher than that of alloys [63,64]; thus, interspot heat transfer can result in heat confinement and potentially affect the gold ablation process. According to [62,65], the electronic diffusivity α_{Au} at a typical for picosecond ablation electron temperature of 10^4 K is ≈500 mm^2/s. The corresponding length of the heat diffusion zone $(\alpha_{Au}t_a)^{1/2}$ at a time t_a of the ablation onset ($t_a \approx 100$ ps for picosecond-laser ablation [66,67]) is about 0.2 μm, that is, much smaller than both the spot size and spot separation. Therefore, interspot heat transfer can be ruled out under the present conditions, leaving hydrodynamic interaction between the cavitation bubbles as a plausible explanation for the observed effect.

The maximal bubble heights under the considered conditions of picosecond PLAL of gold in water were reported to be 250 μm at 2.7 J/cm^2 [58], 330 μm at 3.3 J/cm^2 [57], and 600 μm at 6 J/cm^2 [57], while, for HEA, the reported bubble height is smaller, ≈100 μm at 5 J/cm^2 [18] (although the values were obtained at different pulse energies and cannot be compared directly). In any case, the maximal bubble size is smaller than the spot separation in our experiments with the 1×4 DOE (700 μm), and the relevant dimensionless parameter H^* (the ratio between double bubble spatial separation and their maximum height, introduced in [58]) is expected to be in the range of 1.5–3.0. At first sight, the bubble interaction should also be ruled out as an explanation of the DOE-induced modification of gold NP sizes since the NP diameters were found to be affected by the interaction of two bubbles only at $H^* < 1$ and remained unaffected in double-pulse PLAL at $H^* = 1$ [58]. However, the situation with multiple bubbles appears to be more complicated, and the bubble interaction occurs even at larger H^* values. Thus, Bao et al. [68] investigated the dynamics of three identical, synchronized, symmetrically aligned laser-induced bubbles and demonstrated significant bubble interactions at fairly large separations. It resulted, for instance, in a delay in the evolution of the central bubble with its longer lifetime compared to that of two verge ones even at $H^* = 3$. We believe that such hydrodynamic interaction among bubbles in the MB-PLAL occurs in our experiments with the 1×4 DOE and is a plausible explanation for the observed increase in gold NP sizes. In particular, the extended lifetime of the two central bubbles (serving as NP reactors [69]) allows for NPs to grow to larger sizes, similar to what happens with gold NPs when laser fluence is increased in the single-beam PLAL. This interpretation is also consistent with the relative insensitivity of HEA and FeNi NPs to the beam splitting since the sizes of these NPs are

less affected by laser fluence, that is, by the size and lifetime of the cavitation bubble, under the considered conditions (Figure 8).

The RCV values of the distributions are found to be almost unaffected by the beam splitting for all the materials (Figure 9). An exception is again for FeNi NPs at the lowest fluence (1×11 DOE, P_0/2.7) when the distribution is broader, probably due to an instability of the ablation process at the near-threshold fluence resulting in a larger variation in sizes of the produced NPs.

Although the observed trends are discussed mainly in terms of the applied fluence relative to the material-specific ablation threshold, the material response is also governed by other thermophysical and optical properties. Thermal conductivity, melting and vaporization enthalpies, optical absorption, and energy coupling to the electron subsystem may influence ablation efficiency, melt ejection, plasma-plume and cavitation-bubble dynamics, and nanoparticle formation. For example, the substantially higher thermal conductivity of Au compared with the investigated alloys may affect energy redistribution and melt dynamics within the irradiated region. Therefore, the different responses of Au, FeNi, and HEA to beam shaping should be attributed to the combined influence of several material properties rather than to the ablation threshold alone. Quantitatively separating their individual contributions is beyond the scope of the present study.

An additional process that apparently influences the size distribution of NPs produced under the considered PLAL conditions, especially in the splitting regimes with the 1×11 DOE, is laser-induced fragmentation in liquids (LFL) [2,70-72]. In LFL, laser-irradiated colloidal NPs absorb laser energy to transiently pass an excited state and finally break into small fragments. The LFL method is used efficiently to produce small, size-controlled NPs from larger NPs [20,46,47,70], often as a separate step in addition to PLAL, and from microparticles [72,73]. LFL can also occur during PLAL synthesis if the produced NPs have a sufficiently long residence time in the irradiation area, but in this case it is considered rather a parasitic process [20] since it is difficult to control both NP growth and fragmentation simultaneously.

The considered splitting in the PLAL regime with 11 sub-beams appears to be favorable for the LFL manifestation. With the setup geometry, the flow direction is parallel to the vertical 11-beam line (Figure S13, Supporting Information File 2). Assuming that the PLAL-produced NPs follow the water flow, their velocity in the chamber can be estimated as 1 m/min. Then the average residence time of the NPs in a 1 cm spiral sub-beam irradiation area is about 0.3 s (estimated for NPs produced in central regions), which corresponds to nearly eight full spiral cycles; thus, the NPs, particularly those originating from the bottom regions, undergo repeated laser exposure. In most cases, the used laser fluences are well above the fragmentation threshold (typically below 1 J/cm^2 for picosecond pulses [2,20,72]), and the higher the fluence, the smaller the fragments produced [2]. This is consistent with the increase in the fraction of small gold NPs with increasing fluence (Figure 8, bottom panel). The highest fractions of small Au NPs are observed, in agreement with the above considerations, for the 1×11 splitting regime, exhibiting a unimodal distribution with no statistically resolvable large-particle component at maximal laser power (Figure 8).

We note that LFL is also more likely to occur under single-beam irradiation than in the previous experiments [48]. Here, the chamber volume is five times larger (25 mL instead of 5 mL in [48]) and, with a similar flow rate, this results in a lower removal rate of the produced NPs from the irradiation region, thus giving them a better chance to absorb laser energy. Combined with a longer irradiation time and a high NP synthesis productivity, this represents favorable conditions for LFL. We believe that this is the reason for the difference in the size distributions of gold NPs produced under similar single-beam irradiation conditions, a bimodal distribution in this work and unimodal one in [48].

Donut-shaped beams

As for Gaussian beams, the distributions of donut-beam-generated HEA and FeNi NPs are well described by a single lognormal function, while those for Au NPs exhibit again a bimodal behavior. A single DS beam results generally in smaller HEA and FeNi NPs compared to the corresponding Gaussian pulse (Figure 8), in agreement with the previous observations [48]. This is particularly pronounced at the tails of the distributions where a large-mass cut-off occurs at considerably smaller sizes for DS pulses than for Gaussian pulses, for example, at ≈80 and 90 nm, respectively, for HEA NPs at fairly high fluences (see Figure 2 and Figure S14, Supporting Information File 2). For gold NPs, however, the expected reduction in sizes with the DS pulses is likely masked by the above-discussed LFL processes. As a result, the observed median sizes and fractions of the small population are rather identical for Au NPs produced by single Gaussian and DS pulses (Figure 8).

The RCV values of the NP size distributions obtained with the DS beams are nearly the same as for Gaussian pulses at around 0.25 (Figure 9). Exceptions are observed again at the lowest fluence of 0.9 J/cm^2 (power P_0/11), when the RCVs are somewhat higher, especially for FeNi NPs (RCV = 0.37), that is, the

relative distribution broadening is even stronger than that for the low-fluence Gaussian beam. This is partly due to small median NP sizes under these conditions (note that the smallest sizes of FeNi and Au NPs are obtained here, 43 and 11 nm, respectively, Figure 8). However, other processes, for example, the discussed above NP redeposition at low-fluence DS pulses, can possibly contribute to the observed RCV increase, which requires separate studies.

Splitting the DS beam does not show a distinct reduction in the median NP sizes compared to split Gaussian pulses, as was expected based on experiments with single DS pulses here (Figure 8) and in [48]. The sizes of NPs produced under multi-donut-beam conditions are either similar to those obtained in the corresponding Gaussian MB-PLAL or even larger, with similar RCV values (Figure 8). We attribute this behavior to secondary processes occurring or being promoted under multi-beam irradiation. Different processes appear to be relevant in the two investigated MB-PLAL configurations. For the 1×4 DOE, the observed behavior is most consistent with cavitation-bubble interaction because the relatively short interspot distance promotes hydrodynamic coupling between neighboring bubbles, as discussed above in the contexts of productivity (Sections “Multibeam approach” and “Donut-shaped beams“) and the sizes of NPs produced with Gaussian beams (Section “Gaussian beams”). The interaction of adjacent cavitation bubbles was shown to modify the NP formation process, leading to increased NP size [58]. However, the present experiments do not allow us to quantify the contribution of this mechanism relative to other secondary processes. For DS beams, the bubble interaction is expected to be stronger than that for Gaussian beams at the same pulse energy and spot separation due to a larger spot size [37]. Indeed, the largest size of gold NPs (whose generation appears to be most affected by the bubble interaction) was observed namely in MB-PLAL with four DS sub-beams (Figure 8). To avoid the NP size modification by the hydrodynamic interaction of the cavitation bubbles and thus to obtain an NP size reduction similar to that with a single DS beam, the sub-beam spot separation should be sufficiently large, presumably larger than the maximal lateral size of the bubble by a factor of at least 3–4 [68]. On the other hand, as pointed out in [58], varying the interspot distance is a distinct novel approach for manipulating the NP size distribution in MB-PLAL.

For the conditions with the 1×11 DOE, the spot separation is large (4 mm), so the bubble interaction, even if it exists, is likely a minor factor. Instead, other processes come into play. The most important one, in particular for gold NPs, as for Gaussian pulses, appears to be LFL due to our PLAL setup with the vertical spot line (Figure S13, Supporting Information File 2). This geometry results in repeated re-irradiation of the generated NPs and in a high fraction of the small Au NP population, which is, however, lower than that with 11 Gaussian beams at the same total power (Figure 8), due to a higher laser fluence in the latter case. The LFL process is expected to be significantly suppressed in the MB-PLAL by using a setup with a horizontal line of the spots and a vertical liquid flow. Such an experiment is currently under preparation. Another possible contributor is NP redeposition, which is expected to be particularly efficient for low-fluence DS pulses, as discussed above in the context of productivity. The relative importance of these processes cannot be, however, determined from the present data and should therefore be regarded as a plausible interpretation. The redeposition process is likely to be size-dependent, but, in contrast to LFL, it leads to an increase of the mean size of the remaining colloidal NPs because larger NPs are shown to be predominantly concentrated at the upper part of the cavitation bubble [74] and thus are less affected by the redeposition. This is, therefore, a plausible explanation of why HEA and FeNi NPs produced with 11 DS sub-beams (and which are apparently less affected by LFL) exhibit the highest median size (Figure 8). An increase of laser fluence in the individual sub-beams would obviously reduce the redeposition effect in this MB-PLAL regime, but this was impossible in our experiments due to limitations of the laser power.

We emphasize that the mechanisms discussed above, including cavitation-bubble interaction, laser-induced fragmentation in liquids, and NP redeposition, should be considered as physically motivated interpretations of the observed trends rather than direct experimental observations. While these mechanisms are consistent with our experimental results and previous reports in the literature, their individual contributions cannot be quantitatively separated using the characterization methods employed in the present study. Direct verification would require dedicated diagnostics, such as time-resolved visualization of the bubble dynamics and in situ studies of NP fragmentation and transport, which are beyond the scope of the present work.

Conclusion

A new approach to advancing laser synthesis of colloidal NPs is proposed by combining the advantages of two recently developed PLAL methods, both of which involve spatial shaping of laser pulses. One method is based on multibeam laser ablation created by splitting a laser beam into several sub-beams, which enables a significant increase in synthesis productivity in a cost-effective way. Another method suggests using donut-shaped laser pulses instead of conventional Gaussian pulses to better control the NP size and morphology. A combination of the methods in one PLAL process is expected to address two

main challenges in the use of laser-produced NPs in real-world applications, namely, relatively low synthesis efficiency and insufficient control of the NP size distribution.

In this pilot study, NPs of three materials, gold, an iron–nickel alloy, and a high-entropy alloy, were synthesized by picosecond laser ablation in water using donut-shaped pulses in combination with two MB-PLAL configurations, with 4 and 11 sub-beams. The obtained NPs were compared in terms of productivity and size with those produced by Gaussian pulses and in single-beam PLAL. The experiments were performed over a wide range of laser powers, and we were able to compare single-beam and multibeam PLAL processes at the same pulse energy and fluence per beam.

We have demonstrated that splitting of DS beams into several sub-beams using static DOEs can be as efficient in terms of NP synthesis productivity as that of Gaussian beams. Moreover, at moderate laser fluences (several times the ablation threshold value), DS pulses are found to be even more efficient, possibly because of a larger and more uniformly irradiated ablation spot. At near-threshold fluences, the productivity of DS pulses significantly drops, likely due to redeposition of the ablated material. The obtained productivities of DS-beam-produced HEA and FeNi NPs with the 1×11 DOE are about fourfold higher than those with a single DS beam, that is, the gain in productivity is similar to that observed with Gaussian beams. For gold NPs, the productivity of DS pulses in this MB-PLAL regime is low since fluence is at a near-threshold value even at the maximal laser power. The highest productivity for Au NPs was obtained with the 1×4 DOE and was ≈2.5 times higher than that with a single DS beam. We emphasize that the reported productivity values can be considerably increased in the same MB-PLAL setup by optimization of the laser repetition rates and fluences.

Regarding the NP size distributions, we observe a reduction of the median size of NPs produced by DS pulses in single-beam PLAL in agreement with previous experiments. However, the transfer of this reduction effect to the MB-PLAL configurations is not straightforward and several pitfalls occur due to secondary processes modifying the size distributions. Three processes are identified as potentially important: (a) interaction of individual cavitation bubbles when the interspot distance in MB-PLAL is relatively short; (b) laser fragmentation (in particular, in a non-optimal MB-PLAL configuration, when NPs produced by a sub-beam are repeatedly irradiated by other sub-beams); and (c) NP redeposition (particularly important for low-fluence DS pulses). Mitigation measures to eliminate (or minimize) impacts of the secondary effects are discussed and experiments involving such measures are currently under preparation.

Overall, the results demonstrate that DS beams can be successfully implemented in MB-PLAL without eliminating the productivity advantages of beam splitting. However, achieving simultaneous improvements in productivity and NP size control requires careful optimization of both the optical configuration and the liquid-flow geometry. These findings provide practical guidance for the further development of scalable MB-PLAL systems combining high productivity with improved control over NP size distributions.

Supporting Information

Supporting Information File 1

Data processing details.
[https://www.beilstein-journals.org/bjnano/content/supplementary/2190-4286-17-110-S1.pdf]

Supporting Information File 2

Additional experimental data and figures.
[https://www.beilstein-journals.org/bjnano/content/supplementary/2190-4286-17-110-S2.pdf]

Acknowledgements

The authors thank Nadezhda M. Bulgakova, Stephan Barcikowski, and Anna R. Ziefuss for useful discussions.

Funding

Rémi Bérard conducts his research under the Marie Skłodowska-Curie Actions – COFUND project, which is co-funded by the European Union (Physics for Future – Grant Agreement No. 101081515). Oleksandr Gatsa and Alexander V. Bulgakov acknowledge support from the European Regional Development Fund and the State Budget of the Czech Republic (project SenDiSo: CZ.02.01.01/00/22_008/0004596). Bilal Gökce acknowledges funding by the Deutsche Forschungsgemeinschaft (DFG, German Research Foundation), grant numbers GO 2566/14-1 and GO 2566/7-2. Rémi Bérard also acknowledges support from COST Action CA23125 TETRA "The mETamaterial foRmalism approach to recognize cAncer" (European Cooperation in Science and Technology).

Author Contributions

Rémi Bérard: data curation; formal analysis; investigation; methodology; visualization; writing – original draft; writing – review & editing. Abdel Rahman Altakroury: data curation; formal analysis; investigation; methodology; writing – review & editing. Oleksandr Gatsa: data curation; formal analysis; investigation; methodology; validation; writing – review & editing. Zongwen Fu: project administration; supervision;

writing – review & editing. Bilal Gökce: conceptualization; funding acquisition; methodology; project administration; resources; supervision; validation; writing – review & editing. Alexander V. Bulgakov: conceptualization; funding acquisition; investigation; methodology; project administration; resources; supervision; writing – original draft; writing – review & editing.

ORCID® iDs

Rémi Bérard - https://orcid.org/0000-0002-2332-1371
Oleksandr Gatsa - https://orcid.org/0000-0002-9832-3590
Zongwen Fu - https://orcid.org/0000-0003-2140-2263
Bilal Gökce - https://orcid.org/0000-0001-6368-9659
Alexander V. Bulgakov - https://orcid.org/0000-0002-9651-1328

Data Availability Statement

Data generated and analyzed during this study is available from the corresponding authors upon reasonable request.

Preprint

A non-peer-reviewed version of this article has been previously published as a preprint: https://doi.org/10.3762/bxiv.2026.32.v1

References

1. Yang, G. W. *Prog. Mater. Sci.* **2007,** *52,* 648–698. doi:10.1016/j.pmatsci.2006.10.016
2. Zhang, D.; Gökce, B.; Barcikowski, S. *Chem. Rev.* **2017,** *117,* 3990–4103. doi:10.1021/acs.chemrev.6b00468
3. Amans, D.; Cai, W.; Barcikowski, S. *Appl. Surf. Sci.* **2019,** *488,* 445–454. doi:10.1016/j.apsusc.2019.05.117
4. Amendola, V.; Amans, D.; Ishikawa, Y.; Koshizaki, N.; Scirè, S.; Compagnini, G.; Reichenberger, S.; Barcikowski, S. *Chem. – Eur. J.* **2020,** *26,* 9206–9242. doi:10.1002/chem.202000686
5. Geoffrion, L. D.; Hesabizadeh, T.; Medina-Cruz, D.; Kusper, M.; Taylor, P.; Vernet-Crua, A.; Chen, J.; Ajo, A.; Webster, T. J.; Guisbiers, G. *ACS Omega* **2020,** *5,* 2660–2669. doi:10.1021/acsomega.9b03172
6. Amendola, V.; Guadagnini, A.; Agnoli, S.; Badocco, D.; Pastore, P.; Fracasso, G.; Gerosa, M.; Vurro, F.; Busato, A.; Marzola, P. *J. Colloid Interface Sci.* **2021,** *596,* 332–341. doi:10.1016/j.jcis.2021.03.096
7. Scaramuzza, S.; de Faria, C. M. G.; Coviello, V.; Forrer, D.; Artiglia, L.; Badocco, D.; Pastore, P.; Ghigna, P.; Postuma, I.; Cansolino, L.; Ferrari, C.; Bortolussi, S.; Vago, R.; Spinelli, A. E.; Bekić, M.; Čolić, M.; Amendola, V. *Adv. Funct. Mater.* **2023,** *33,* 2303366. doi:10.1002/adfm.202303366
8. Forsythe, R. C.; Cox, C. P.; Wilsey, M. K.; Müller, A. M. *Chem. Rev.* **2021,** *121,* 7568–7637. doi:10.1021/acs.chemrev.0c01069
9. Matten, M.; Koch, N. G.; Caidi, A.; Radev, I.; Lange, T.; Barcikowski, S.; Reichenberger, S. *J. Phys. Chem. C* **2025,** *129,* 7740–7750. doi:10.1021/acs.jpcc.5c00223
10. Ji, S.; Li, P.; Zhao, X.; Wei, S.; Cheng, X.; Wu, L.; Ye, Y.; Ma, K.; Cai, Y.; Liang, C. *Sens. Actuators, B* **2023,** *383,* 133595. doi:10.1016/j.snb.2023.133595
11. Cortes, F. R. U.; Falomir, E.; Lancis, J.; Mínguez-Vega, G. *Appl. Surf. Sci.* **2024,** *665,* 160326. doi:10.1016/j.apsusc.2024.160326
12. Hupfeld, T.; Wegner, A.; Blanke, M.; Doñate-Buendía, C.; Sharov, V.; Nieskens, S.; Piechotta, M.; Giese, M.; Barcikowski, S.; Gökce, B. *Adv. Opt. Mater.* **2020,** *8,* 2000473. doi:10.1002/adom.202000473
13. Logunov, L.; Ulesov, A.; Khramenkova, V.; Liu, X.; Kuchmizhak, A. A.; Vinogradov, A.; Makarov, S. *Nanomaterials* **2023,** *13,* 965. doi:10.3390/nano13060965
14. Chausali, N.; Saxena, J.; Prasad, R. *J. Agric. Food Res.* **2023,** *12,* 100541. doi:10.1016/j.jafr.2023.100541
15. Kosajan, V.; Wen, Z.; Wang, X. *J. Ind. Ecol.* **2025,** *29,* 344–357. doi:10.1111/jiec.13601
16. Bulgakov, A. V.; Bulgakova, N. M. *Sci. China: Phys., Mech. Astron.* **2022,** *65,* 274207. doi:10.1007/s11433-021-1858-9
17. Streubel, R.; Barcikowski, S.; Gökce, B. *Opt. Lett.* **2016,** *41,* 1486–1489. doi:10.1364/ol.41.001486
18. Gatsa, O.; Tahir, S.; Flimelová, M.; Riahi, F.; Doñate-Buendia, C.; Gökce, B.; Bulgakov, A. V. *Nanomaterials* **2024,** *14,* 365. doi:10.3390/nano14040365
19. Kalus, M.-R.; Reimer, V.; Barcikowski, S.; Gökce, B. *Appl. Surf. Sci.* **2019,** *465,* 1096–1102. doi:10.1016/j.apsusc.2018.09.224
20. Ziefuss, A. R.; Reich, S.; Reichenberger, S.; Levantino, M.; Plech, A. *Phys. Chem. Chem. Phys.* **2020,** *22,* 4993–5001. doi:10.1039/c9cp05202j
21. Spellauge, M.; Redka, D.; Podhrazsky, A.; Eckmann, K.; Eulenkamp, C.; Koepp, O.; Doñate-Buendia, C.; Gökce, B.; Barcikowski, S.; Huber, H. P. *Laser Photonics Rev.* **2026,** *20,* e01348. doi:10.1002/lpor.202501348
22. Doñate-Buendía, C.; Fernández-Alonso, M.; Lancis, J.; Mínguez-Vega, G. *Photonics Res.* **2019,** *7,* 1249–1257. doi:10.1364/prj.7.001249
23. Sylvestre, J.-P.; Kabashin, A. V.; Sacher, E.; Meunier, M. *Appl. Phys. A: Mater. Sci. Process.* **2005,** *80,* 753–758. doi:10.1007/s00339-004-3081-4
24. Zhang, D. S.; Li, Z. G.; Liang, C. H. *Sci. China: Phys., Mech. Astron.* **2022,** *65,* 274203. doi:10.1007/s11433-021-1860-x
25. Shih, C.-Y.; Streubel, R.; Heberle, J.; Letzel, A.; Shugaev, M. V.; Wu, C.; Schmidt, M.; Gökce, B.; Barcikowski, S.; Zhigilei, L. V. *Nanoscale* **2018,** *10,* 6900–6910. doi:10.1039/c7nr08614h
26. Shih, C.-Y.; Shugaev, M. V.; Wu, C.; Zhigilei, L. V. *Phys. Chem. Chem. Phys.* **2020,** *22,* 7077–7099. doi:10.1039/d0cp00608d
27. Sajti, C. L.; Sattari, R.; Chichkov, B. N.; Barcikowski, S. *J. Phys. Chem. C* **2010,** *114,* 2421–2427. doi:10.1021/jp906960g
28. Cristoforetti, G.; Pitzalis, E.; Spiniello, R.; Ishak, R.; Muniz-Miranda, M. *J. Phys. Chem. C* **2011,** *115,* 5073–5083. doi:10.1021/jp109281q
29. Intartaglia, R.; Bagga, K.; Brandi, F. *Opt. Express* **2014,** *22,* 3117–3127. doi:10.1364/oe.22.003117
30. Khairani, I. Y.; Mínguez-Vega, G.; Doñate-Buendía, C.; Gökce, B. *Phys. Chem. Chem. Phys.* **2023,** *25,* 19380–19408. doi:10.1039/d3cp01214j
31. Messina, G. C.; Wagener, P.; Streubel, R.; De Giacomo, A.; Santagata, A.; Compagnini, G.; Barcikowski, S. *Phys. Chem. Chem. Phys.* **2013,** *15,* 3093–3098. doi:10.1039/c2cp42626a
32. Monsa, Y.; Gal, G.; Lerner, N.; Bar, I. *Nanotechnology* **2020,** *31,* 235601. doi:10.1088/1361-6528/ab78ac
33. Mansour, Y.; Battie, Y.; Naciri, A. E.; Chaoui, N. *Nanotechnology* **2023,** *34,* 075602. doi:10.1088/1361-6528/aca3b0
34. Barcikowski, S.; Menéndez-Manjón, A.; Chichkov, B.; Brikas, M.; Račiukaitis, G. *Appl. Phys. Lett.* **2007,** *91,* 083113. doi:10.1063/1.2773937

35. Semaltianos, N. G. *Crit. Rev. Solid State Mater. Sci.* **2010,** *35,* 105–124. doi:10.1080/10408431003788233
36. Khairani, I. Y.; Spellauge, M.; Riahi, F.; Huber, H. P.; Gökce, B.; Doñate-Buendía, C. *Adv. Photonics Res.* **2024,** *5,* 2300290. doi:10.1002/adpr.202300290
37. Molina-Prados, S.; Bulgakova, N. M.; Bulgakov, A. V.; Lancis, J.; Vega, G. M.; Doñate-Buendia, C. *Beilstein J. Nanotechnol.* **2026,** *17,* 309–342. doi:10.3762/bjnano.17.22
38. Sobhan, M. A.; Ams, M.; Withford, M. J.; Goldys, E. M. *J. Nanopart. Res.* **2010,** *12,* 2831–2842. doi:10.1007/s11051-010-9868-7
39. Mahdieh, M. H.; Fattahi, B. *Appl. Surf. Sci.* **2015,** *329,* 47–57. doi:10.1016/j.apsusc.2014.12.069
40. Hamad, A.; Li, L.; Liu, Z. *Appl. Phys. A: Mater. Sci. Process.* **2015,** *120,* 1247–1260. doi:10.1007/s00339-015-9326-6
41. Mafuné, F.; Kohno, J.-y.; Takeda, Y.; Kondow, T. *J. Phys. Chem. B* **2002,** *106,* 7575–7577. doi:10.1021/jp020577y
42. Essaidi, A.; Chakif, M.; Schöps, B.; Aumman, A.; Xiao, S.; Esen, C.; Ostendorf, A. *J. Laser Micro/Nanoeng.* **2013,** *8,* 131–136. doi:10.2961/jlmn.2013.02.0003
43. Gao, C.; Vuong, J.; Zhang, Q.; Liu, Y.; Yin, Y. *Nanoscale* **2012,** *4,* 2875–2878. doi:10.1039/c2nr30300k
44. Sylvestre, J.-P.; Kabashin, A. V.; Sacher, E.; Meunier, M.; Luong, J. H. T. *J. Am. Chem. Soc.* **2004,** *126,* 7176–7177. doi:10.1021/ja048678s
45. Rehbock, C.; Merk, V.; Gamrad, L.; Streubel, R.; Barcikowski, S. *Phys. Chem. Chem. Phys.* **2013,** *15,* 3057–3067. doi:10.1039/c2cp42641b
46. Besner, S.; Kabashin, A. V.; Winnik, F. M.; Meunier, M. *Appl. Phys. A: Mater. Sci. Process.* **2008,** *93,* 955–959. doi:10.1007/s00339-008-4773-y
47. Luo, R.-C.; Li, C.; Du, X.-W.; Yang, J. *Angew. Chem., Int. Ed.* **2015,** *54,* 4787–4791. doi:10.1002/anie.201411322
48. Altakroury, A. R.; Gatsa, O.; Riahi, F.; Fu, Z.; Flimelová, M.; Samokhvalov, A.; Barcikowski, S.; Doñate-Buendía, C.; Bulgakov, A. V.; Gökce, B. *Beilstein J. Nanotechnol.* **2025,** *16,* 407–417. doi:10.3762/bjnano.16.31
49. Tang, Y.; Perrie, W.; Rico Sierra, D.; Li, Q.; Liu, D.; Edwardson, S. P.; Dearden, G. *Micromachines* **2021,** *12,* 376. doi:10.3390/mi12040376
50. Tahir, S.; Shkodich, N.; Eggert, B.; Lill, J.; Gatsa, O.; Flimelová, M.; Adabifiroozjaei, E.; Bulgakova, N. M.; Molina-Luna, L.; Wende, H.; Farle, M.; Bulgakov, A. V.; Doñate-Buendía, C.; Gökce, B. *ChemNanoMat* **2024,** *10,* e202400064. doi:10.1002/cnma.202400064
51. Arachchige, C. N. P. G.; Prendergast, L. A.; Staudte, R. G. *J. Appl. Stat.* **2022,** *49,* 268–290. doi:10.1080/02664763.2020.1808599
52. Neuenschwander, B.; Jaeggi, B.; Schmid, M.; Hennig, G. *Phys. Procedia* **2014,** *56,* 1047–1058. doi:10.1016/j.phpro.2014.08.017
53. Jee, Y.; Becker, M. F.; Walser, R. M. *J. Opt. Soc. Am. B* **1988,** *5,* 648–659. doi:10.1364/josab.5.000648
54. Raciukaitis, G.; Brikas, M.; Gecys, P.; Gedvilas, M. *Proc. SPIE* **2008,** *7005,* 70052L. doi:10.1117/12.782937
55. Armbruster, O.; Naghilou, A.; Kitzler, M.; Kautek, W. *Appl. Surf. Sci.* **2017,** *396,* 1736–1740. doi:10.1016/j.apsusc.2016.11.229
56. Gamaly, E. G.; Madsen, N. R.; Duering, M.; Rode, A. V.; Kolev, V. Z.; Luther-Davies, B. *Phys. Rev. B* **2005,** *71,* 174405. doi:10.1103/physrevb.71.174405
57. Tomko, J.; Naddeo, J. J.; Jimenez, R.; Tan, Y.; Steiner, M.; Fitz-Gerald, J. M.; Bubb, D. M.; O'Malley, S. M. *Phys. Chem. Chem. Phys.* **2015,** *17,* 16327–16333. doi:10.1039/c5cp01965f
58. Riahi, F.; Bußmann, A.; Doñate-Buendia, C.; Adami, S.; Adams, N. A.; Barcikowski, S.; Gökce, B. *Photonics Res.* **2023,** *11,* 2054–2071. doi:10.1364/prj.498204
59. Doan, H. D.; Iwatani, N.; Sasaki, H.; Matsumura, S.; Fushinobu, K. Nanosecond time-resolved visualization of short pulse laser ablation processes for various laser beam profiles. Proc. 14th IEEE Int. Conf. on Thermal and Thermomechanical Phenomena in Electronic Systems (ITherm), Orlando, FL, USA; 2014; pp 1279–1284. doi:10.1109/itherm.2014.6892428
60. Inasawa, S.; Sugiyama, M.; Yamaguchi, Y. *J. Phys. Chem. B* **2005,** *109,* 9404–9410. doi:10.1021/jp0441240
61. Marzun, G.; Nakamura, J.; Zhang, X.; Barcikowski, S.; Wagener, P. *Appl. Surf. Sci.* **2015,** *348,* 75–84. doi:10.1016/j.apsusc.2015.01.108
62. Lin, Z.; Zhigilei, L. V.; Celli, V. *Phys. Rev. B* **2008,** *77,* 075133. doi:10.1103/physrevb.77.075133
63. Ho, C. Y.; Ackerman, M. W.; Wu, K. Y.; Oh, S. G.; Havill, T. N. *J. Phys. Chem. Ref. Data* **1978,** *7,* 959–1178. doi:10.1063/1.555583
64. He, M.; Wu, C.; Shugaev, M. V.; Samolyuk, G. D.; Zhigilei, L. V. *J. Phys. Chem. C* **2019,** *123,* 2202–2215. doi:10.1021/acs.jpcc.8b09922
65. Lizunov, S. A.; Bulgakov, A. V.; Campbell, E. E. B.; Bulgakova, N. M. *Appl. Phys. A: Mater. Sci. Process.* **2022,** *128,* 602. doi:10.1007/s00339-022-05733-4
66. Willis, D. A.; Xu, X. *Appl. Surf. Sci.* **2002,** *197–198,* 118–123. doi:10.1016/s0169-4332(02)00314-8
67. Carrasco-García, I.; Vadillo, J. M.; Laserna, J. J. *J. Anal. At. Spectrom.* **2019,** *34,* 2119–2125. doi:10.1039/c9ja00196d
68. Bao, H.; Zhang, H.; Gao, L.; Tang, M.; Zhang, C.; Lu, J. *Ultrason. Sonochem.* **2021,** *71,* 105375. doi:10.1016/j.ultsonch.2020.105375
69. Rehbock, C.; Jakobi, J.; Gamrad, L.; van der Meer, S.; Tiedemann, D.; Taylor, U.; Kues, W.; Rath, D.; Barcikowski, S. *Beilstein J. Nanotechnol.* **2014,** *5,* 1523–1541. doi:10.3762/bjnano.5.165
70. González-Rubio, G.; Guerrero-Martínez, A.; Liz-Marzán, L. M. *Acc. Chem. Res.* **2016,** *49,* 678–686. doi:10.1021/acs.accounts.6b00041
71. Huang, H.; Zhigilei, L. V. *J. Phys. Chem. C* **2021,** *125,* 13413–13432. doi:10.1021/acs.jpcc.1c03146
72. Spellauge, M.; Auer, R.; Tack, M.; Limani, F.; Redka, D.; Reichenberger, S.; Ziefuss, A. R.; Barcikowski, S.; Huber, H. P. *Opt. Laser Technol.* **2026,** *203,* 115762. doi:10.1016/j.optlastec.2026.115762
73. Kim, D.; Jang, D. *Appl. Surf. Sci.* **2007,** *253,* 8045–8049. doi:10.1016/j.apsusc.2007.02.153
74. Ibrahimkutty, S.; Wagener, P.; Menzel, A.; Plech, A.; Barcikowski, S. *Appl. Phys. Lett.* **2012,** *101,* 103104. doi:10.1063/1.4750250

License and Terms

This is an open access article licensed under the terms of the Beilstein-Institut Open Access License Agreement (https://www.beilstein-journals.org/bjnano/terms), which is identical to the Creative Commons Attribution 4.0 International License (https://creativecommons.org/licenses/by/4.0). The reuse of material under this license requires that the author(s), source and license are credited. Third-party material in this article could be subject to other licenses (typically indicated in the credit line), and in this case, users are required to obtain permission from the license holder to reuse the material.

The definitive version of this article is the electronic one which can be found at:
https://doi.org/10.3762/bjnano.17.110